Development of the Detectors for the Muon-to-Electron Conversion Search Experiment Using Pulsed Proton Beam from J-PARC RCS and Measurement of Momentum Spectrum of Muon Decay in Orbit from Muonic Atoms

A dissertation submitted to
the Graduate School of Science, Osaka City University
in partial fulfillment of the requirements
for the degree of Doctor of Philosophy in science

January, 2019

by
Natsuki Teshima

Natsuki Teshima

Development of the Detectors for the Muon-to-Electron Conversion Search Experiment Using Pulsed Proton Beam from J-PARC RCS and Measurement of Momentum Spectrum of Muon Decay in Orbit from Muonic Atoms

Thesis directed by Prof. Yoshihiro Seiya

Abstract

The Standard Model of particle physics successfully describes all phenomena observed in experiments so far. However, the hint of new physics beyond the Standard Model is not provided yet. At present, much focus is being placed on searching for rare reaction processes of particle interactions as a search for new physics. In this thesis, the preparation status of DeeMe experiment, an experimental plan to search for muon-to-electron conversion that is not yet discovered, is presented.

In the experiment, a signal of muon-to-electron conversion is an electron with a monochromatic energy of 105 MeV, and we search for it using a magnetic spectrometer. The spectrometer consists of four tracking detectors, multi-wire proportional chambers (MWPCs), and a magnet called PACMAN. The MWPCs have reading cathode strips, and anode and potential wires stretched alternately, to which high voltage applied momentarily at the timing of searching for a signal. We discuss development of these innovative MWPCs including optimization of filling gases, improvement of the reading circuits, and the test of suppressing oscillation on the output waveform induced by the high voltage switching. The detection efficiency for an electron improved by two times of that for the old setting as the whole magnetic spectrometer.

In June, 2017, we measured momentum spectra of muon decay in orbit, which is a main background in DeeMe experiment, at J-PARC Material and Life Science Experimental Facility (MLF) D2 Area. In this experiment, the MWPCs and a magnet of KEK Muon Science Laboratory was used. Calibration of the magnetic spectrometer, momentum analysis, and the comparison with the theoretical model of the momentum spectra are discussed in this thesis.

Acknowledgement

I am very grateful to my supervisors Prof. Yoshihiro Seiya and Prof. Kazuhiro Yamamoto for their guidance, wisdom and motivation.

I thank Prof. Masaharu Aoki, Dr. Yohei Nakatsugawa, Dr. Hiroaki Natori, Dr. Nguyen Minh Truong, Daiki Nagao, and the other members of the DeeMe Collaboration for their help, intelligence and hard work.

I am very grateful to Prof. Hiroshi Itoyama for reading this thesis carefully and giving me sound advice.

I thank Prof. Nobuyuki Kanda, Prof. Eiichi Nakano, and Prof. Shoichi Ogio of Osaka City University for their teaching and kindness. I thank Prof. Nobuhito Maru for his theoretical support.

Thanks to friends at the High Energy Physics Laboratory of Osaka City University and for outside of study for the good times.

Thanks to my parents and brother for never doubting my ability to carry it through.

I am very grateful to Ono Scholarship Foundation (Ono Pharmaceutical Co., Ltd.), Research Fund for Ph.D. Students of Osaka City University and JGC-S Scholarship Foundation (JGC Corporation) for their support and care over the years.

The DeeMe Collaboration, 2018

K. Shigaki, Y. Shingo
Hiroshima University, Hiroshima, Japan

M. Ikegami, Y. Irie, N. Kawamura, H. Kobayashi, S. Makimura, H. Matsumoto, T. Mibe, S. Mihara, Y. Miyake, H. Nishiguchi, C. Ohimori, N. Saito, K. Shimomura, P. Strasser, T. Yamazaki, M. Yoshii
High Energy Accelerator Research Organization (KEK), Tsukuba, Japan

H. Natori
Institute for Basic Science, Daejeon, Korea

Y. Nakatsugawa
Institute of High Energy Physics, Beijing, China

M. Kinsho, S. Meigo, P. K. Saha, K. Yamamoto
Japan Atomic Energy Agency (JAEA), Tokai, Japan

K. Yoshimura
Okayama University, Okayama, Japan

M. Adachi, Y. Seiya, T. Takahashi, N. Teshima, K. Yamamoto, H. Yoshinaka
Osaka City University, Osaka, Japan

M. Aoki, D. Nagao
Osaka University, Osaka, Japan

S. Ritt
Paul Scherrer Institut, 5232 Villigen, Switzerland

T. Numao
TRIUMF, Vancouver, Canada

D. Bryman
University of British Columbia, Vancouver, Canada

N. M. Truong
University of Da Nang - University of Science and Technology, Da Nang, Vietnam

N. D. Thong
Vietnam National University, Ho Chi Minh, Vietnam

Contents

List of Figures

List of Tables

Chapter 1

Introduction

1.1 Standard Model

Elementary particle physics aims to explain the nature of elementary particles, the smallest components of matter, and the interaction between them, and to discover the fundamental laws of nature. The Standard Model (SM) has been established and extremely successful in predicting the behavior of elementary particles. In the Standard Model, elementary particles include quarks, leptons, which are matter particles (fermions), and gauge bosons, which are carrier particles for the forces between matter particles.

Table 1.1: Fermions.

	Three Generations of Matter				
	I	II	III	Charge $Q/\lvert e\rvert$	Spin
Quarks	u (up)	c (charm)	t (top)	$+2/3$	1/2
	d (down)	s (strange)	b (bottom)	$-1/3$	1/2
Leptons	ν_e (electron neutrino)	ν_μ (muon neutrino)	ν_τ (tau neutrino)	0	1/2
	e^- (electron)	μ^- (muon)	τ^- (tau)	-1	1/2

Table 1.2: Gauge bosons.

	Interaction	Charge $Q/\|e\|$	Spin
γ (photon)	electromagnetic	0	1
g (gluon)	strong	0	1
$W^{\pm}$ (W boson)	weak	± 1	1
Z^0 (Z boson)	weak	0	1

1.2 Physics beyond the Standard Model

There are some unsolved problems in the SM. The electroweak scale ($\sim 10^2$ GeV) is much smaller than the Planck scale ($\sim 10^{19}$ GeV), at which the strength of gravity is expected to become comparable with the electroweak interaction or strong interaction. This is known as the hierarchy problem. Due to this problem, the theory requires very unnatural fine-tuning. Moreover, there are some phenomena that the SM cannot explain, for example, neutrinos have masses. Thus, the SM is considered to be a low-energy approximation to a more complete theory at higher energies. At high energy scales, new phenomena beyond the SM are expected to exist.

The LHC experiments at CERN searches for new physics beyond the SM at the energy frontier by using large accelerators. On the other hand, experiments at the intensity frontier explore some of the rarest processes using intense particle beam and sensitive detectors. That means a different approach to finding new physics.

1.3 Charged Lepton Flavor Violation

Leptons are assigned with a lepton number of +1, antileptons −1. In the SM, lepton number is conserved in particle interactions. Moreover, for the charged particles, lepton number has three types, and the number of each type is also conserved.

For example, consider the muon decay (Michel decay),

$$\mu^- \quad \rightarrow \quad e^- + \nu_\mu + \overline{\nu_e}. \tag{1.1}$$

The muon (μ^-) on the left side carrys a lepton number +1, the electron (e^-) +1, the muon neutrino (ν_μ) +1 and the anti-electron neutrino ($\overline{\nu_e}$) −1 on the right side. The sum of lepton number on the right side is +1 and the lepton numbers are the same. The muon carrys an electron number 0. On the right side, the electron carrys $+1$, the muon neutrino 0 and the anti-electron neutrino -1 and the sum of electron number is 0. The electron number is preserved. The muon carrys a muon number $+1$, the electron 0, the muon neutrino $+1$, the anti-electron neutrino 0. The muon number is also conserved to be $+1$.

Consider the muon capture (MC),

$$\mu^- + (A, Z) \quad \rightarrow \quad \nu_\mu + (A, Z-1) \tag{1.2}$$

where A is the atomic mass and Z is the atomic number of the matter in which the muon is stopped. The sum of lepton number is $+1$, that of muon number $+1$ and that of electron number Z. Through these interactions the lepton number and charged lepton numbers are conserved.

Makoto Kobayashi and Toshihide Maskawa proposed an explanation of CP violation and quark-flavor-changing processes was confirmed by the Belle experiment at KEK and the BaBar experiment at SLAC (Stanford Linear Accelerator Center) [1]. Furthermore, Super-Kamiokande experiment or T2K experiment at J-PARC discovered neutrino oscillation, which means neutrinos can change from one flavor to another like quarks do [2–4].

On the other hand, Charged Lepton Flavor Violation (cLFV) processes have not been observed yet (Fig. 1.1). In the Standard Model to which neutrino oscillations are added, the branching ratio for cLFV processes is too small to be observe experimentally. As an example, decay diagram for $\mu \rightarrow e\gamma$ via neutrino oscillation, that is one of cLFV processes, is shown in Fig. 1.2. In this process, muon decays into W-boson and mu-neutrino, and its mu-neutrino oscillates and becomes electron-neutrino. The electron-neutrino then interacts with the W-boson. The branching ratio for $\mu \rightarrow e\gamma$ is given by

$$Br(\mu \rightarrow e\gamma) = \frac{3\alpha}{32\pi} \left| \sum_{i=2,3} U^*_{\mu i} U_{ei} \frac{\Delta m^2_{i1}}{M^2_W} \right|^2 < 10^{-54} \tag{1.3}$$

where $U_{\mu i}$, U_{ei} are Maki-Nakagawa-Sakata (MNS) matrix (neutrino mixing matrix) components, Δm_{ij} mass difference between neutrinos, M_W the mass of W-boson [5, 6]. Mass difference between neitrinos ($\Delta m^2_{21} = 7.5 \times 10^{-5}$ eV^2, $|\Delta m^2_{32}| = 2.44 \times 10^{-3}$ eV^2) is much less than the mass of W-boson ($M_W = 80.376$ GeV). Thus, the upper limit on the branching ratio is greatly reduced to 10^{-54}.

However, some theoretical models beyond the Standard Model predict higher branching ratio, 10^{-13} to 10^{-16}, for us to be able to find the cLFV processes experimentally. If the processes are observed, that is a clear evidence of new physics beyond the SM existing.

1.3.1 History of Searching for Charged Lepton Flavor Violating Processes

In the 1930's, Hideki Yukawa predicted the existence of mesons, which explained the interaction between nucleons. In 1936, muons were discovered in cosmic rays. Muons have a mass about 200 times that of the electron. Due to its mass, the muon was initially thought to be Yukawa's meson However, the muon was found to have a longer life time and not to interact with nucleons, so that it was not Yukawa's meson. In the point of view regarding a question whether the muon was an excited state of the electron, Hincks and Pontecorvo conducted an experiment to search for $\mu \to e\gamma$ in 1947 [7,8]. That was the first experiment of searching for cLFV processes. Then, the sensitivity is improving by two orders of magnitude every 10 years (see in Fig. 1.3), however, the processes have never been observed [9].

Technological advance of accelerators brings a lot of muons into use relatively easily. Furthermore, because the decay processes of muons are not subject to strong interactions, the result of experiments using muons is less affected by backgrounds than that using hadrons like K^0_L, K^+. The experiments using muons thus are attracting attention in searching for cLFV processes.

1.3.2 Muon to Electron Conversion

Proton beams from the accelerator are injected into the target to produce pions. Pions then decay into muons, and the muons captured in orbit around nucleons of the target. Atoms having muons in the orbit like electrons around nuclei are called muonic atoms. Bound muons fall into the stable state (1s) of the atoms as characteristic X-rays are emitted. With the framework of the SM, muons in orbit then decay into neutrinos and electrons, Eq. (1.1), or fall into the nuclei, Eq. (1.2).

Muon to electron conversion,

$$\mu^- + (A, Z) \quad \to \quad e^- + (A, Z) \tag{1.4}$$

has a muon number +1, electron number Z on the left side, muon number 0 and electron number $Z + 1$ on the right side, which is one of cLFV processes against the conservation laws of electron number and muon number.

For muon to electron conversion, the conversion electron is monoenergetic with an energy $E_{\mu e}$ equal to the muon mass m_μ minus the binding energy of the muon in 1s orbit of muonic atom B_μ, and nuclear recoil energy E^0_{rec},

$$\begin{aligned} E_{\mu e} &= m_\mu - B_\mu - E^0_{\text{rec}} & (1.5) \\ E^0_{\text{rec}} &\simeq \frac{(m_\mu - B_\mu)^2}{2M_A}. & (1.6) \end{aligned}$$

The nuclear recoil energy E^0_{rec} is so small as to be ignorable. The binding energy of the muon in 1s orbit of muonic atom depends on the muonic atomic mass.

Due to dependence on interaction between muon and nuclei, the branching ratio of muon to electron conversion is defined as ratio of decay width for muon to electron conversion to that for muon capture by nuclei,

$$Br(\mu^- + (A,Z) \to e^- + (A,Z)) \equiv \frac{\Gamma[\mu^- + (A,Z) \to e^- + (A,Z)]}{\Gamma[\mu^- + (A,Z) \to \nu_\mu + (A,Z-1)]}. \quad (1.7)$$

1.3.3 Search for Muon to Electron Conversion and $\mu \to e\gamma$

Possible processes for cLFV can be classified as photonic-like ones as shown in Fig. 1.5 and non-photonic-like ones as shown in 1.4. These can be expressed by an effective Lagrangian $\mathcal{L}$ [10],

$$\mathcal{L} = \frac{1}{1+\kappa}\frac{m_\mu}{\Lambda^2}\overline{\mu_{\text{R}}}\sigma^{\mu\nu}e_{\text{L}}F_{\mu\nu} + \frac{\kappa}{1+\kappa}\frac{1}{\Lambda^2}(\overline{\mu_{\text{L}}}\gamma^\mu e_{\text{L}})(\overline{q_{\text{L}}}\gamma_\mu q_{\text{L}}). \quad (1.8)$$

For photonic processes, because the intermediate state needs to be photon, the branching ratio for muon to electron conversion is about one hundredth of that for $\mu \to e\gamma$. If the non-photonic contribution dominates, only muon to electron conversion may exist even though $\mu \to e\gamma$ is not observed. We must study cLFV processes with different approaches.

1.4 Theoretical Models

1.4.1 Supersymmetry

Supersymmetry (SUSY) is a major candidate for the model beyond the SM to solve the hierarchy problem. In the theory, particle types occur in pairs, so that there is a boson (fermion) type for each fermion (boson) type. However, SUSY particles have never been found so far and the symmetry is breaking. The symmetry breaking terms of the symmetry breaking cause charged lepton flavor violation.

The slepton mass matrix is represented by

$$m_{\tilde{l}}^2 = \begin{pmatrix} m_{\tilde{e}\tilde{e}}^2 & \Delta m_{\tilde{e}\tilde{\mu}}^2 & \Delta m_{\tilde{e}\tilde{\tau}}^2 \\ \Delta m_{\tilde{\mu}\tilde{e}}^2 & m_{\tilde{\mu}\tilde{\mu}}^2 & \Delta m_{\tilde{\mu}\tilde{\tau}}^2 \\ \Delta m_{\tilde{\tau}\tilde{e}}^2 & \Delta m_{\tilde{\tau}\tilde{\mu}}^2 & m_{\tilde{\tau}\tilde{\tau}}^2 \end{pmatrix} \tag{1.9}$$

and the non-diagonal component induces the cLFV processes. Figure 1.5 is an example of diagram for μ-e conversion with SUSY particles. In this diagram, a muon converts into an electron through a neutrarino $\tilde{\chi}^0$ exchange. A smuon $\tilde{\mu}$ changes to a selectron $\tilde{e}$ and the photon emitted is absorbed by a quark.

There are two supersymmetric scenarios, SUperSYmmetric Grand Unified Theory (SUSY-GUT) and Supersymmetric extensions of the Seesaw mechanism (SUSY-Seesaw), which give some values to the non-diagonal components of the slepton mass matrix.

1.4.2 Supersymmetric Grand Unified Theory (SUSY-GUT)

It is predicted that strong interaction and the weak interaction may be unified at an energy scale of $\sim 10^{16}$ GeV. This is called the Grand Unified Theory.

In the SUSY-GUT which is the Grand Unifies Theory with SUSY extension, the non-diagonal component of the slepton mass matrix is expressed by

$$\Delta m_{\tilde{\mu}\tilde{e}}^2 \propto \frac{3m_0^2 + A_0^2}{8\pi^2} h_t^2 V_{td}^* V_{ts} \ln \frac{M_{GUT}}{M_{R_3}}, \tag{1.10}$$

where m_0 is the universal scaler mass, A_0 the scaler trilinear coupling, h_t the Yukawa coupling of top quarks, V_{td}, V_{ts} the Cabibbo-Kobayashi-Maskawa matrix components, M_{GUT} the mass scale of Grand Unified Theory, M_{R_3} the mass of right-handed neutrino [11, 12].

Figure 1.6 shows the branching ratio of μ-e conversion as a function of mass of right-handed selectron in $SU(5)$ SUSY-GUT. The $\tan\beta$ is the ratio of two vacuum expectation values of the Higgs fields, coupling to up-type or down-type quarks, and μ is a parameter to determine the masses of Higgs and Higgsino. In this theory, the branching ratio is predicted to be 10^{-19} to 10^{-13}.

The branching ratio of $\mu \rightarrow e\gamma$ as a function of mass of right-handed selectron in $SU(10)$ SUSY-GUT is shonw in Fig. 1.7. The branching ratio becomes larger, 10^{-13} to 10^{-11} in this theory [13].

1.4.3 Supersymmetric Extensions of the Seesaw Mechanism (SUSY-Seesaw)

In the seesaw mechanism, right-handed neutrinos, which do not exist in the Standard Model, are introduced. The reason why only left-handed neutrinos are observed is because the right-handed neutrinos are too heavy to observe. Figure 1.8 shows a diagram for μ-e conversion with heavy neutrinos.

The right- and left-handed neutrinos have asymmetric couplings to the Higgs fields, and that causes the non-diagonal components of the slepton mass matrix [14]. The non-diagonal component of the slepton mass matrix is

$$\Delta m^2_{\tilde{\mu}\tilde{e}} \propto \frac{3m_0^2 + A_0^2}{8\pi^2} h_\tau^2 U^*_{\tau e} U_{\tau\mu} \ln \frac{M_{GUT}}{M_{R_3}}, \tag{1.11}$$

where h_τ is τ Yukawa coupling constant, $U_{\tau e}$ and $U_{\tau\mu}$ are the Maki-Nakagawa-Sakata (MNS) matrix neutrino mixing matrix components.

Figure 1.9 shows the branching ratio for $\mu \to e\gamma$ predicted in the SUSY-Seesaw. The branching ratio greatly depends on the Marjorana mass of right-handed neutrinos.

The μ-e conversion is sensitive to some theories of new physics with loop-type operators like the second Higgs doublet, or contact term operators such as leptoquarks, heavy Z' or anomalous Z coupling (Fig. 1.10).

1.5 DeeMe Experiment

The DeeMe (Direct emission of electron from Muon to electron conversion) is an experiment to search for μ-e conversion and it is planned to be conducted at Materials and Life Science Experimental Facility (MLF) of J-PARC in Japan [15].

Figure 1.11 illustrates the conceptual design of the DeeMe experiment. When pulsed proton beams from the 3 GeV synchrotron RCS hit the target, negative pions are produced. In general experiments to search for μ-e conversion, pions are collected using an electromagnet to decay into muons, and the muons are stopped at a stopping target. On the other hand, in the DeeMe experiment, the pion production target is also used for the muon-decay and the muon-transport section, and the muon-stopping target. We can then perform a compact experiment.

A negative muon stopped in the target is bound around the nucleus of a target atom. We will search for a μ-e conversion signal, a delayed electron with a monochromatic energy by measuring the momentum using a spectrometer.

First, we will aim at a single event sensitivity (SES) of 1×10^{-13} utilizing proton beams with a power of 1 MW and a carbon target for 1 year (2×10^{8} seconds). It is under investigation to change the target to a target made of silicon carbide for better SES of about 2×10^{-14}.

The pulsed proton beams from RCS have a structure with two bunches. When pulse proton beams hit the target, a large quantity of charged particles, prompt burst, is produced (Fig. 1.12). Even if only particles with an energy near 105 MeV are transported by the beamline, it is estimated that 2×10^{8} charged particles per pulse will come to the spectrometer. The detectors need to quickly restore its operation after prompt burst and detect a delayed electron of μ-e conversion.

The signal

In the DeeMe experiment, the signal of μ-e conversion is an electron with an energy of 105.06 MeV for muonic carbon atoms or 104.91 MeV for muonic silicon atoms. The life times of muonic atoms are 2.0 μs and 0.76 μs, respectively.

Backgrounds

There are background of electrons which originate from decays of muons bounded on the orbits of muonic atoms (muon Decay in Orbit, DIO). They could acquire energies as large as 105 MeV due to the nuclear recoil. Figure 1.13 shows the expected momentum spectra of DIO electrons for muonic carbon, aluminum, silicon, and titanium atoms [16].

Another type of background electrons would be produced by the proton beams from the accelerator RCS if they happen to be extracted to the target with a delayed timing, which we call the delayed-proton background.

Figure 1.14 shows the momentum spectra of signal electrons (green), background electrons produced through DIO (red), and beam-related background electrons produced by delayed protons of the accelerator (magenta), where we assume the RCS operating with 1 MW for 2×10^{7} seconds (1 year), using a target made of silicon carbide, the branching fraction of μ-e conversion 3×10^{-14}, and the ratio of the number of delayed protons to the number of protons per pulse $< 10^{-19}$. To separate the signals from the high-momentum tail of the DIO background, we need a spectrometer with a momentum resolution $\Delta p < 1$ MeV.

There may be electrons produced through muon decay in flight, or through electron-positron pair production by photons from the radiative pion capture (RPC) resulting from pions stopped in the target. These are in the prompt timing, outside the analysis window.

Cosmic-ray background is suppressed by a factor of $\simeq 1/10000$ because the analysis window is a few microseconds while the cycle of the accelerator RCS is 40 milliseconds.

1.6 Precedent Experiments

Table 1.3 lists the current upper limits on the charged lepton flavor violation for muons.

Table 1.3: The current upper limits on charged lepton flavor violation for muons.

Decay mode	Upper limit of branching fraction	Experiment
$\mu^+ \to e^+\gamma$	5.7×10^{-13}	MEG at PSI
$\mu^+ \to e^+e^+e^-$	1.0×10^{-12}	SINDRUM at PSI
$\mu^- + \mathrm{Au} \to e^- + \mathrm{Au}$	7×10^{-13}	SINDRUM-II at PSI
$\mu^- + \mathrm{Ti} \to e^- + \mathrm{Ti}$	4.3×10^{-12}	SINDRUM-II at PSI
$\mu^- + \mathrm{Ti} \to e^- + \mathrm{Ti}$	4.6×10^{-12}	TRIUMF

1.6.1 SINDRUM-II

The SINDRUM-II Experiment at Paul Scherrer Institute (PSI) in Switzerland is the newest experiment searching for μ-e conversion [17]. Figure 1.15 shows the result of the SINDRUM-II Experiment. The target is gold. The monochromatic energy E_e of signal electrons from μ-e conversion is 95.6 MeV for this experiment.

In the momentum plot of negative muon beams, two events with higher momenta than that of DIO are found. It is thought that this is more likely to be backgrounds from pions because DC muon beams are used.

The current upper limit of μ-e conversion is $Br(\mu^- + \mathrm{Au} \rightarrow e^- + \mathrm{Au}) \leq 7 \times 10^{-13}$ (90% C. L.).

1.6.2 MEG

The MEG Experiment started in 2018 to search for $\mu^+ \rightarrow e^+\gamma$ at PSI [18]. In the experiment, the signal is a pair of positron and photon from two-body decay after positive muons are stopped at a target. The current upper limit $Br(\mu^+ \rightarrow e^+ + \gamma) < 4.2 \times 10^{-13}$ (90% C. L.) is obtained in 2017. The preparation of MEG-II Experiment is now in progress to improve search sensitivity by one order of magnitude.

1.7 Experimental Plan in the Future

1.7.1 COMET

The COMET (COherent Muon to Electron Transition) is an experiment to search for μ-e conversion at J-PARC Hadron Hall. The Collaboration consists of more than 200 people representing 40 institutes (as of October, 2018). In the experiment, a target made of aluminum will be used and the monochromatic energy of signal electrons will be 105.0 MeV.

The COMET Phase-I aims to a sensitivity $Br(\mu^- + \mathrm{Al} \rightarrow e^- + \mathrm{Al}) \leq 7.2 \times 10^{-15}$ to improve the sensitivity by two orders of magnitude. The preparation for the detectors will finish in 2019, and the experiment will start after the construction of beamline. The COMET Phase-II will aim to achieve $Br(\mu^- + \mathrm{Al} \rightarrow e^- + \mathrm{Al}) \leq 2.6 \times 10^{-17}$ to further improve sensitivity by two orders of magnitude from Phase-I [19].

1.7.2 Mu2e

The Mu2e Experiment is planned to search for μ-e conversion at Fermi National Accelerator Laboratory (FNAL) in the United States [20]. Using a target made of aluminum, the experiment aims at a sensitivity at the same level as the COMET Phase-II to improve the sensitivity by four orders of magnitude from the current upper limit, and is going to take data from 2022. In addition, the Mu2e-II Experiment is planned to further improve sensitivity by one order of magnitude from the Mu2e Experiment.

1.7.3 MEG-II

The MEG-II Experiment aims to search for $\mu^+ \to e^+ + \gamma$ with a better sensitivity by one order of magnitude than the MEG Experiment by using the basic design of the MEG Experiment with an improved muon beam intensity, the resolution and the efficiency of the detectors. Data taking will start in 2019.

1.7.4 Mu3e

The Mu3e Experiment is planned to search for $\mu^+ \to e^+e^+e^-$ at PSI. That aims for a sensitivity of 2×10^{-15} in Phase-I and 1×10^{-16} in Phase-II. Data taking will start in 2019-2020.

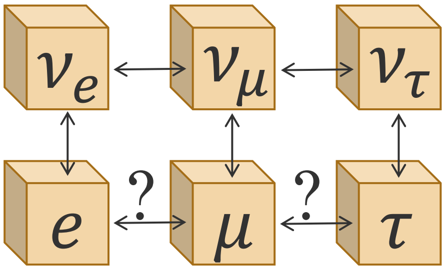

Figure 1.1: Leptons and charged lepton flavor violation.

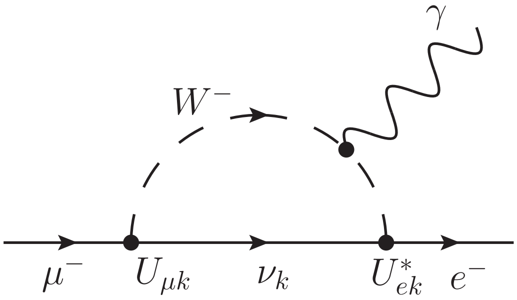

Figure 1.2: Feynman diagram for the $\mu^- \to e^-\gamma$ via neutrino oscillation.

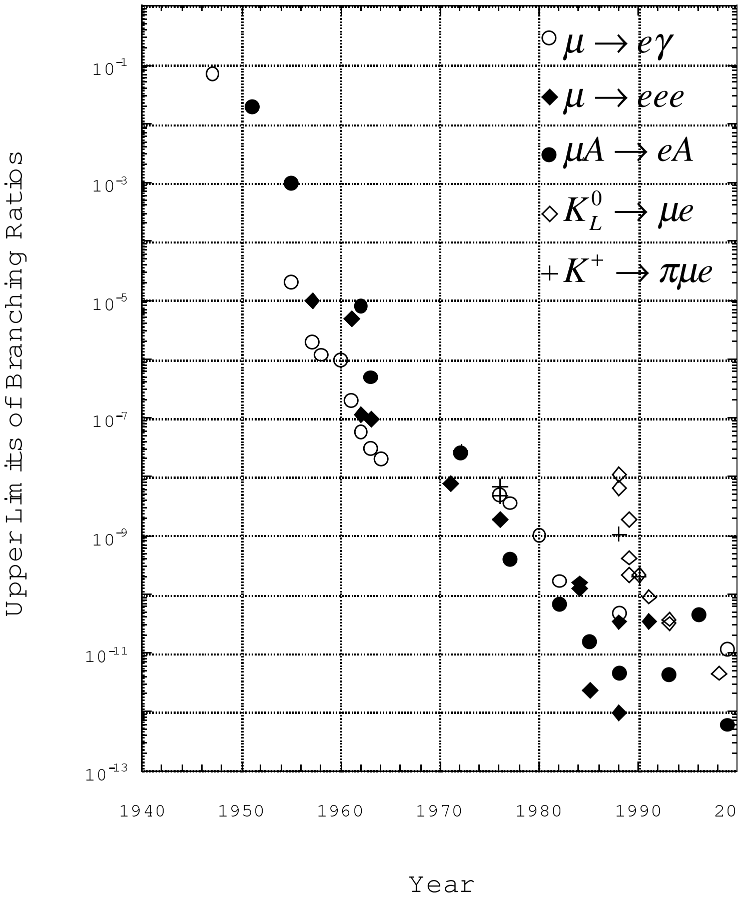

Figure 1.3: Upper limits on the branching ratios of various charged-lepton-flavor-violating processes as a function of year [9].

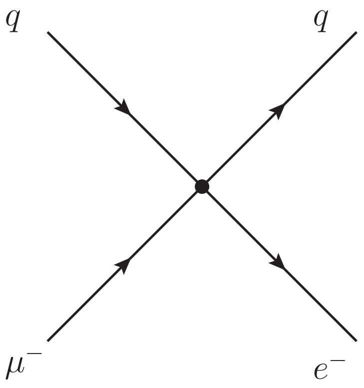

Figure 1.4: Diagram for non-photonic μ-e conversion.

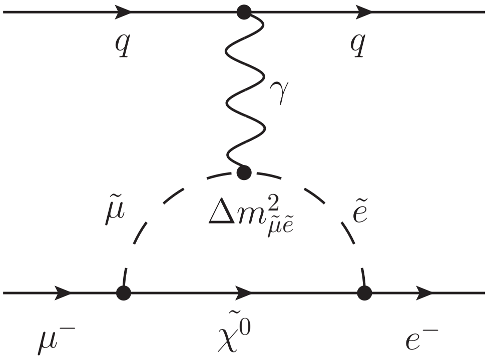

Figure 1.5: An example of diagram for μ-e conversion with supersymmetric particles.

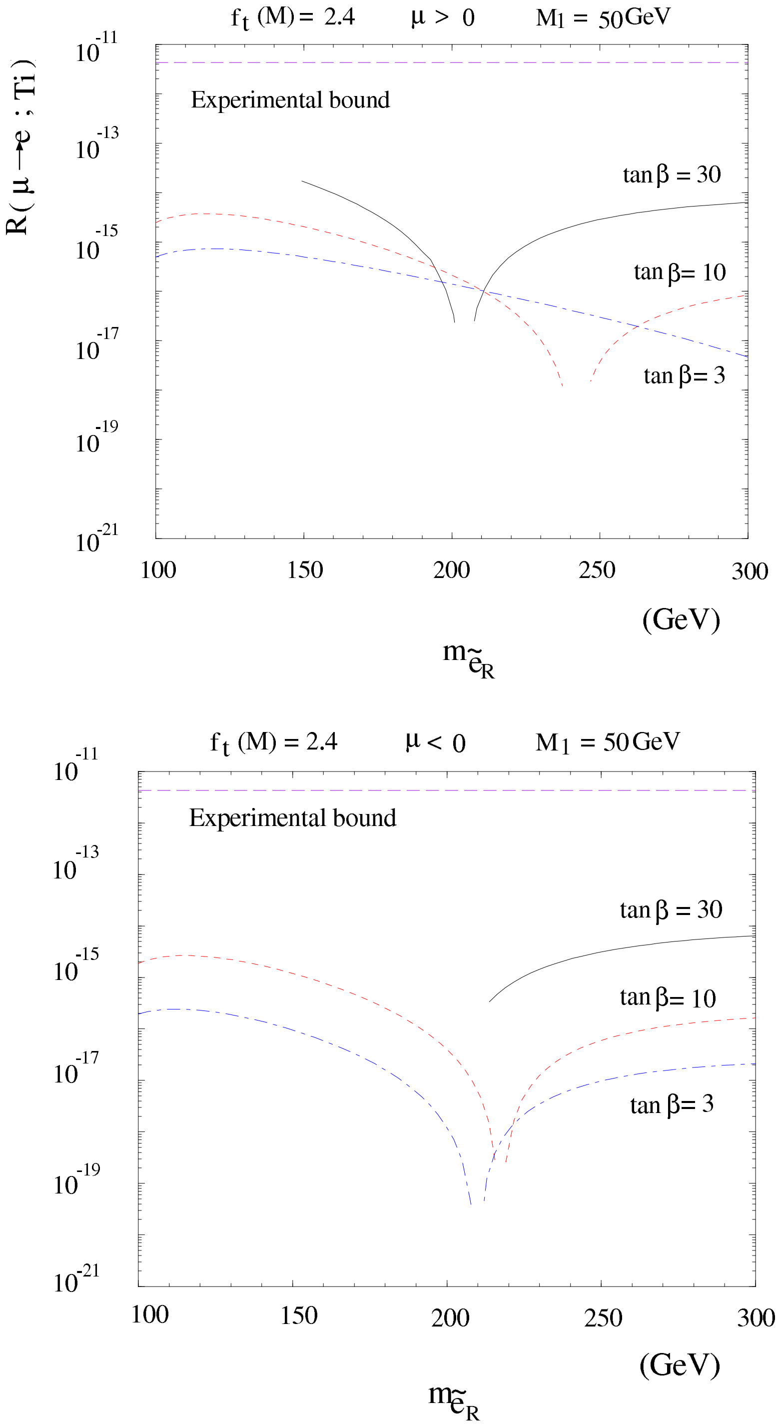

Figure 1.6: The branching ratio of μ-e conversion as a function of $m_{\tilde{e}_R}$ in $SU(5)$ SUSY-GUT [12].

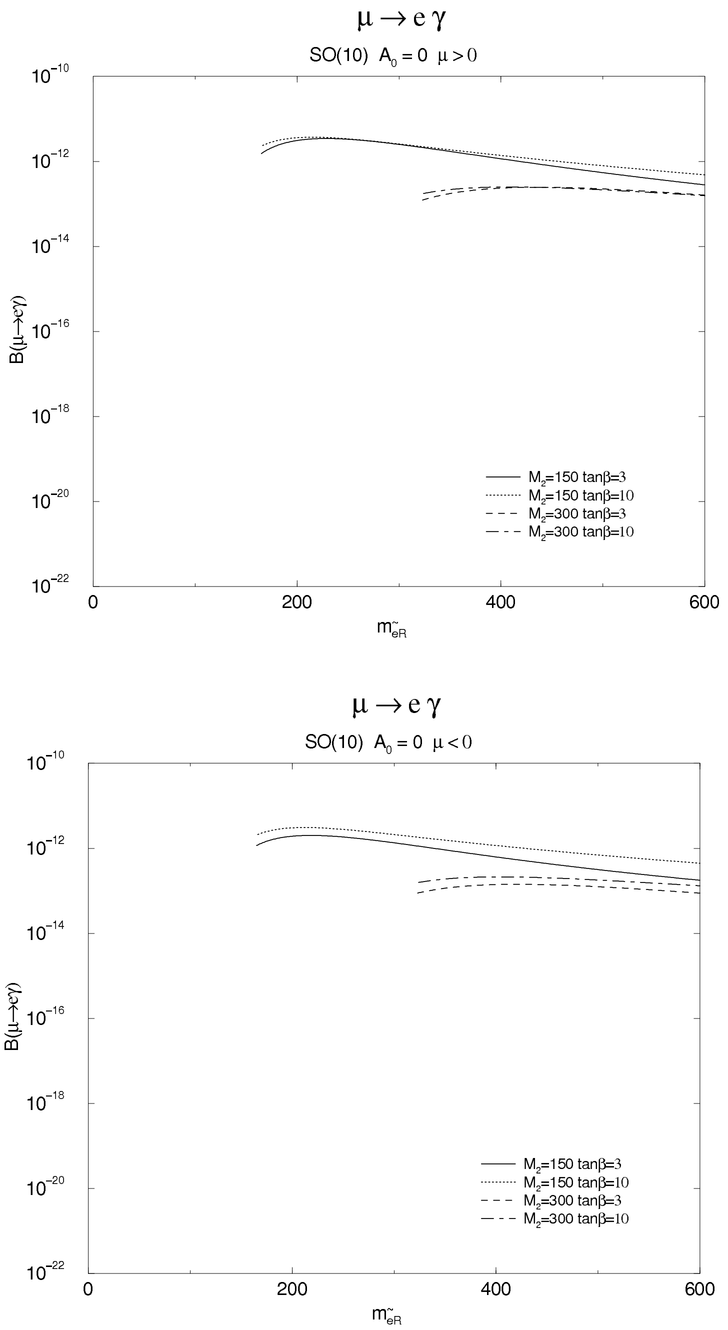

Figure 1.7: The branching ratio of $\mu \to e\gamma$ as a function of $m_{\tilde{e_R}}$ in $SU(10)$ SUSY-GUT [13].

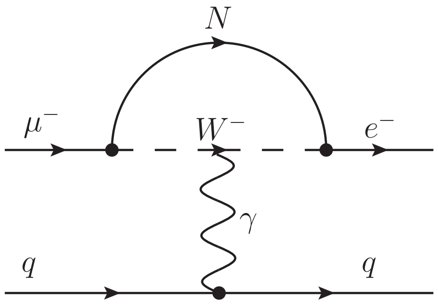

Figure 1.8: A diagram for μ-e conversion with heavy neutrinos.

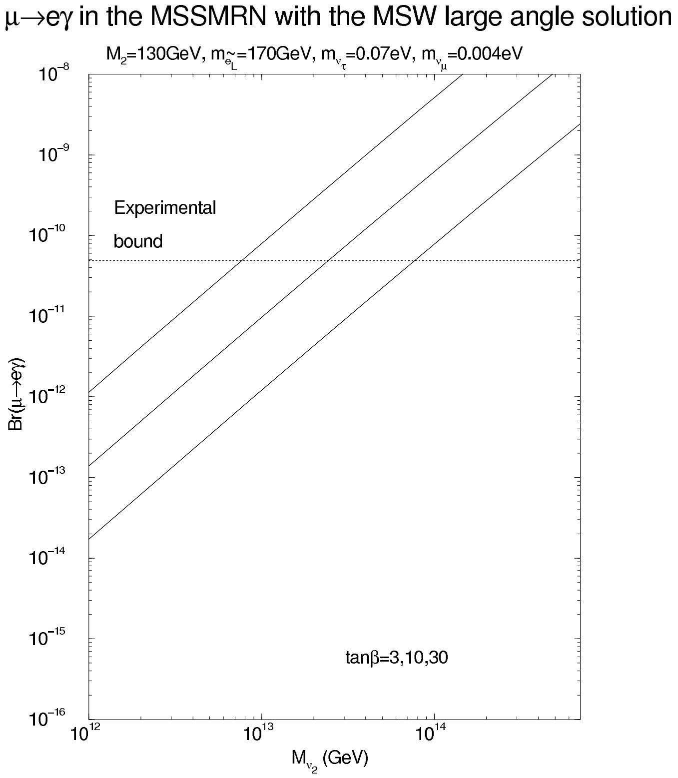

Figure 1.9: The branching ratio for $\mu \rightarrow e\gamma$ as a function of Majorana mass of the second right-handed neutrinos in Minimal Supersymmetric Standard Model (MSSM) [14].

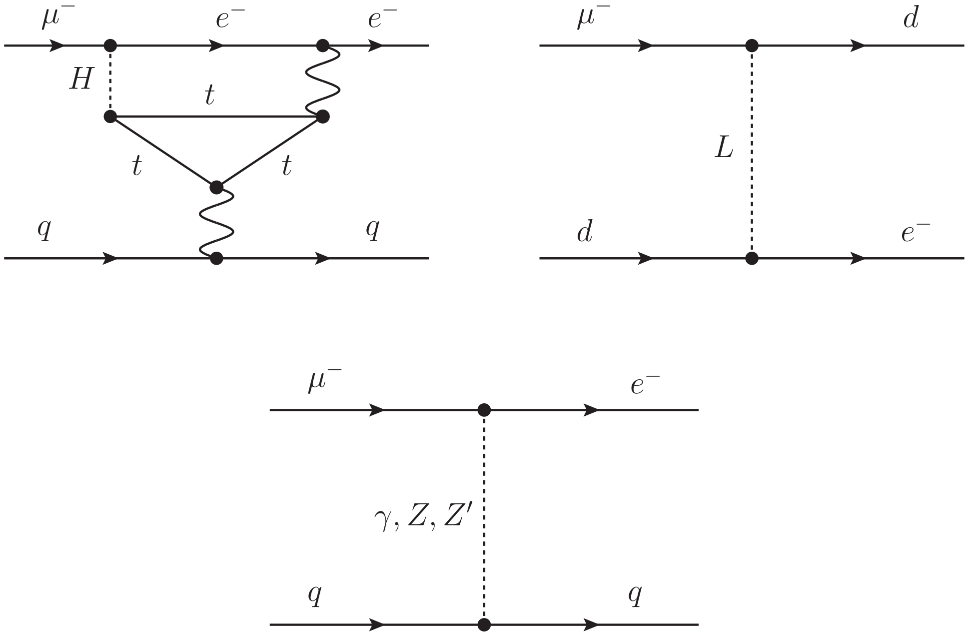

Figure 1.10: Diagrams for μ-e conversion. Loop-type operator like the second Higgs doublet and contact term operators like leptoquarks, heavy Z' or anomalous Z coupling.

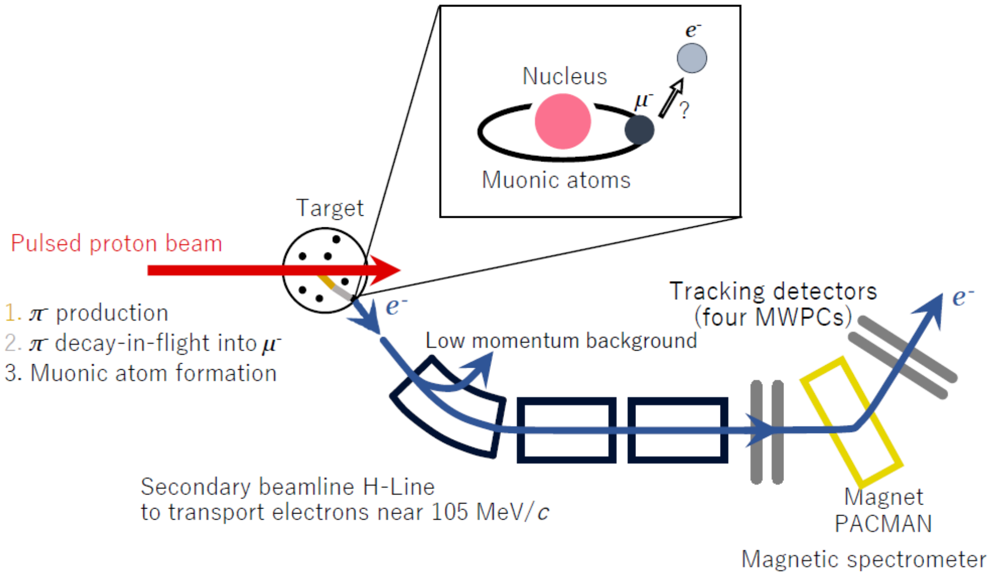

Figure 1.11: The method of the DeeMe experiment.

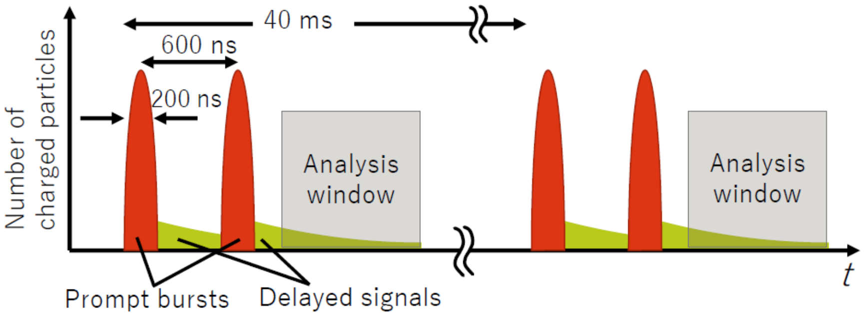

Figure 1.12: Expected charged particles (prompt bursts and delayed signals) which hit the first multi-wire proportional chamber.

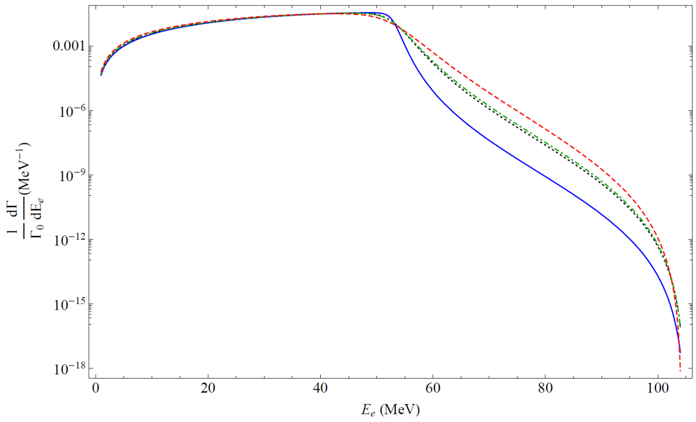

Figure 1.13: The expected momentum spectra of the electrons generated by muon Decay in Orbit (DIO) for carbon (blue line), aluminum (black line), silicon (broken green line), or titanium (broken red line) muonic atoms [16].

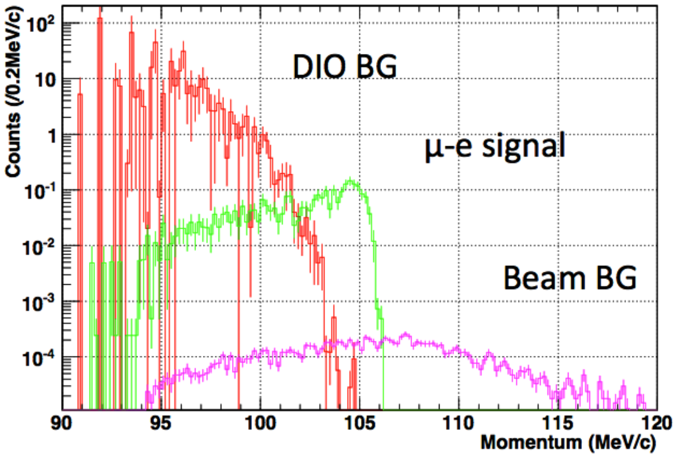

Figure 1.14: Monte Carlo calculation of expected momentum spectra of electrons obtained by the spectrometer.

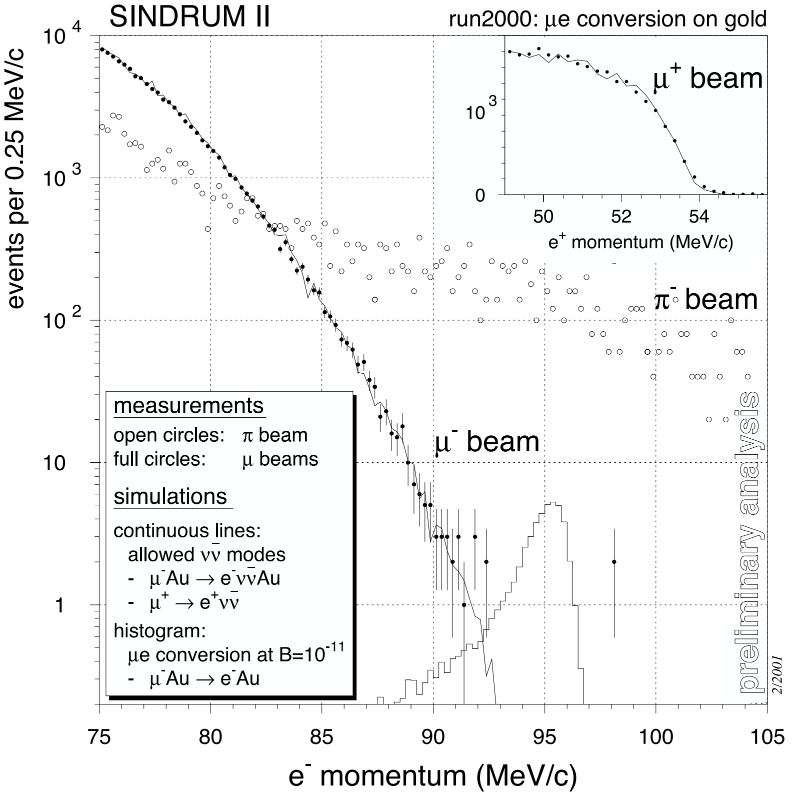

Figure 1.15: Result of the SINDRUM-II Experiment [17].

Chapter 2

Experimental Apparatus

We are preparing for the DeeMe experiment at Materials and Life Science Experimental Facility (MLF), Japan Proton Accelerator Research Complex (J-PARC) in Tokai village, Ibaraki, Japan. The following sections describe some facilities of J-PARC and the expetimental apparatus which will be used for the DeeMe experiment [21].

2.1 Japan Proton Accelerator Research Complex (J-PARC)

J-PARC is a high intensity proton accelerator facility which is operated by a joint management between High Energy Accelerator Research Organization (KEK) and Japan Atomic Energy Agency (JAEA). The high intensity proton beams hit targets to produce various secondary particle (like neutrons, muons, kaons and neutrinos). Utilizing the beams of the secondary particles, researches are conducted on a broad range of fields such as particle physics, nuclear physics, materials science, life science, and nuclear engineering. A birds-eye view of J-PARC is shown in Fig. 2.1.

2.1.1 Linear Accelerator (LINAC)

First, negative hydrogen ions H^- are produced in the source of LINAC in the left of Fig. 2.1. The cycle of the acceleration is up to 50 Hz. Those negative hydrogen ions are accelerated to 400 MeV, and then they are divided with 25 Hz in two beamlines, the beamline to the 3 GeV synchrotron Rapid Cycle Synchrotron (RCS) and the beamline to the superconducting linear accelerator for further accelerate.

2.1.2 Rapid Cycle Synchrotron (RCS)

The RCS is a 3 GeV proton-synchrotron with a length of 348 m in circumference. Negative hydrogen ions from the LINAC are converted into proton H^+ beams, by using a charge converting film made of carbon and removing two electrons from H^-, and injected to the RCS. Those proton beams are accelerated to 3 GeV, and then they are sent to Materials and Life Science Experimental Facility (MLF) and the 50 GeV synchrotron Main Ring through the beam transport systems at the downstream.

The proton beam intensity sent to the MLF has been steadily increased. The oparation with 300 kW started in 2012, and the power increased to 400 kW in March, 2015, then to 500 kW in April, 2015. In the future, the intensity is planned to be increased up to 1 MW (333 μA or 2.1×10^5 protons per second).

The beams are extracted from the RCS to the MLF with a method called fast extraction. In principle, no proton remains in the ring of the RCS after extraction to supply high purity pulsed proton beams to the MLF.

Some protons could exist in the ring after extraction, and if any, we call them delayed protons. Delayed protons might be transported to the target and produce electrons; thus, they can be backgrounds of the experiment. We put a counter at injection into the RCS and estimate the number of delayed protons.

Table 2.1 gives main proton beam parameters of the RCS.

Table 2.1: Main beam parameters of the RCS.

Extraction beam energy	3 GeV
Number of bunches	2
Repetition	25 Hz
Beam intensity	500 kW (September, 2015) 150 kW (March, 2017) 150 kW (June, 2017)

2.1.3 Materials and Life Science Experimental Facility (MLF)

MLF is situated in the center of the 50 GeV synchrotron Main Ring (MR) (Fig. 2.1). In the MLF building, the two-bunch pulsed-proton beams from the RCS hit the target to produce muon beams and neutron beams. Those beams are utilized for studies in the fields of materials science, life science, and so on.

2.1.4 Muon Production Target

To produce muon beams in the MLF, a rotating target made of carbon (C) is used (as of November, 2017). We are investigating a possibility to change the target to a target made of silicon carbide (SiC) [22].

The following are the advantage of changing the target made of C to another one made of SiC:

- The wave function of Si atomic nuclei overlaps with that of negative muons more than that of C atomic nuclei. After negative muons stop in matter, muons are captured by Si nuclei with a probability of 62% for Si nuclei, while they are captured by C nuclei with 8% for C nuclei. For negative muons stopping in a mixture of matter, assuming that the muon capture depends on the atomic number (known as Fermi-Teller Z-law), 70% of negative muons react with Si nuclei and 30% of those react with C nuclei. Thus, the reaction rate of negative muons with a target made of SiC and with a target made of C is $0.62 \times 0.7 + 0.08 \times 0.3 = 46\%$, 8%, respectively, and the sensitivity of the experiment using a target made of SiC will be 6 times better than that using a target made of C.

- We will get 1.7 times more low-energy muons using a target made of SiC than using that made of C.

- Compared to C, SiC has higher degree of hardness, heat, and radiation resistivity.

The rotating target made of SiC is being developed by Organization of Advanced Sustainability Initiative for Energy System or Materials (OASIS) at Muroran Institute of Technology.

The life times of muonic C atoms and muonic Si atoms are 2.0 second and 0.76 second, respectively. For better sensitivities, we need detectors with dead time as short as possible.

2.1.5 MUon Science Establishment (MUSE)

MUSE in the J-PARC MLF is one of the world's highest intensity muon facilities for contribution to a wide range of fields from basic to applied science.

Figure 2.2 shows the MUSE in the MLF. Four muon beam lines, Decay/surface muon beamline (D Line), Ultra-slow muon beamline (U Line), Surface muon beamline (S Line), and High-momentum muon beamline (H Line) of the MUSE, will be connected from the muon production target to the experimental areas. We will conduct the DeeMe experiment at the H Line of them [23].

2.1.6 High-Momentum Muon Beamline (H Line)

As of December, 2017, H Line is under construction in the J-PARC MLF. The H Line drawn by G4beamline [24] is shown in Fig. 2.3. The beamline from the target to the magnetic spectrometer consists of a large-diameter capture solenoid HS1, two dipole magnets HB1, HB2, two transport solenoids HS2, HS3, and three quadrupole magnets HQ1, HQ2, HQ3.

The H Line will transport charged particles with momenta of 90 to 120 MeV/c, around 105 MeV/c which is the momentum of an electron from the muon to electron conversion. Thereby, removing electrons with low momenta produced by negative-muon decay and beam muon/pion capture by nuclei.

Figure 2.4 gives the acceptance of the magnets of the H Line and spectrometer as a function of momentum. The acceptance of the spectrometer in the signal-momentum region is approximately 120 msr/(MeV/c).

Expectations for the H Line are high in research of fundamental physics of muons. It is proposed to conduct experiments for measuring muonium hyperfine structure and anomalous magnetic moment g-2/EDM of muons, which might also give a hint for the existence of new physics beyond the Standard Model [25].

2.1.7 D2 Area at Decay/Surface Muon Beamline (D Line)

There is a D2-area apparatus for muon basic science in the J-PARC MLF. The muon beam intensity with a 300 kW proton beam from RCS is 3.0×10^6 μ^+/s. We can use surface muons, positive or negative muons up to 50 MeV/c with a double or single pulse structure.

Utilizing D2, we tested multi-wire proportional chambers used for DeeMe in 2015, and measured the momenta of DIO electrons in 2017. The DIO electrons will be one of main backgrounds in the experiment in 2017. The setup of measurement of DIO electrons is shown in Fig. 2.5.

2.2 Magnetic Spectrometer

For precisely measuring the momenta of electrons, a magnetic spectrometer is placed at the downstream of the H Line (Fig. 2.3). The spectrometer consists of a dipole magnet called PACMAN (shown in Fig. 2.6) and four tracking detectors. Two of the four tracking detectors are put before the magnet and the other two are put after the magnet. We briefly summarize how to measure the momenta using a magnetic spectrometer. Figure 2.6 shows the magnet used for the DeeMe experiment and its coordinate system. The direction of charged particles is from the surface to the back of the photo in Fig. 2.6. For the sake of ease, a uniform magnetic field with only the y component is applied and a charged particle circularly moves on the xz plane. When a relativistic charged particle circularly moves in a uniform magnetic field, the motion is described by

$$\frac{m_0 v^2}{r} \frac{1}{\sqrt{1-(v/c)^2}} = qvB \tag{2.1}$$

with m_0: rest mass of the charged particle, v: velocity, r: radius of circular motion, c: the speed of light, q: charge, B: magnetic flux density, so that the radius of circular motion becomes

$$r = \frac{1}{cqB} \frac{cm_0 v}{\sqrt{1-(v/c)^2}}. \tag{2.2}$$

Substituting 3×10^8 m/s into c, 1.6×10^{-19} C into q, 0.4 T (the strength of the magnetic field in the experimental design) into B and 105 MeV/c into momentum $m_0 v/\{1-(v/c)^2\}^{-1/2}$, we find

$$\begin{aligned} r &= \frac{1}{3 \times 10^8\ \mathrm{m/s} \times 1.6 \times 10^{-19}\ \mathrm{C} \times 0.4\ \mathrm{T}}\, c \cdot 105\ \mathrm{MeV}/c \qquad (2.3) \\ &= \frac{1}{3 \times 10^8\ \mathrm{m/s} \times 1.6 \times 10^{-19}\ \mathrm{A \cdot s} \times 0.4\ \mathrm{N \cdot A^{-1} \cdot m^{-1}}}\, 105\ \mathrm{MeV} \\ &= \frac{1}{3 \times 10^8 \times 1.6 \times 10^{-19} \times 0.4\ \mathrm{N}}\, 105 \times 10^6 \times 1.6 \times 10^{-19}\ \mathrm{N \cdot m} \\ &\simeq 0.88\ \mathrm{m}. \end{aligned}$$

Thus, electrons with a momentum of 105 MeV/c will circularly move with a curvature radius of approximately 0.88 m in a uniform magnetic field of 0.4 T.

2.2.1 Electromagnet Called PACMAN

To apply a magnetic field to the spectrometer, we will use a dipole electromagnet called PACMAN. This magnet was used for the PIENU experiment at TRIUMF in Canada, an experiment to measure the branching ratio of positive-pion decay into positive muons and positrons [26].

This magnet was shipped from TRIUMF to the J-PARC MLF in August, 2014. The size is 2350 mm in the x-axis direction, 2500 mm in the y-axis direction, and 700 mm in the z-axis direction. The magnet weights 29.5 t. The winding of two coils is 2 × 132 times.

Consider the magnetic field in the center of the magnet. Ampere's circuital law is denoted by

$$\oint_{\partial S} \boldsymbol{H} \cdot d\boldsymbol{l} = nI. \tag{2.4}$$

with ∂S: boundary of the integral region S, $\boldsymbol{H}$: strength of the magnetic field, $\boldsymbol{l}$: vector line element, n: number of the coil turns, I: total current passing through the integral region S. As shown in Fig. 2.7, consider a integral region S closed by a loop with a radius of r. The angle between two pole surfaces is about $\pi/6$ rad of 2π rad, thus

$$\left(\frac{\pi}{6\mu_{air}} + \frac{11\pi}{6\mu_{iron}}\right) rB = nI \tag{2.5}$$

where B is the magnetic flux density, and μ_{air} and μ_{iron} the magnetic permeability of air and iron, respectively. From the formula, the magnetic flux density can be found

$$B = \left(\frac{1}{6\mu_{air}} + \frac{11}{6\mu_{iron}}\right)^{-1} \frac{nI}{\pi r}. \tag{2.6}$$

Substituting $1.26 \times 10^{-6}\ \mathrm{N \cdot A^{-2}}$ into μ_{air}, $6.30 \times 10^{-3}\ \mathrm{N \cdot A^{-2}}$ into μ_{iron}, 264 into n, 300 A into I and 0.5 m (approximate radius of the circle) into r, we find

$$\begin{aligned}
B = &\left(\frac{1}{6 \times 1.26 \times 10^{-6}\ \mathrm{N \cdot A^{-2}}} + \frac{11}{6 \times 6.30 \times 10^{-3}\ \mathrm{N \cdot A^{-2}}}\right)^{-1} \\
&\times \frac{264 \times 300\ \mathrm{A}}{3.14 \times 0.5\ \mathrm{m}} \\
\simeq &\ 0.4\ \mathrm{N \cdot A^{-1} \cdot m} \\
= &\ 0.4\ \mathrm{T} \\
(= &\ 4000\ \mathrm{Gauss}\ ).
\end{aligned}$$

In July, 2015, the magnet, PACMAN was tested and we measured the magnetic field at the J-PARC MLF. It worked well for flowing current up to 500 A (voltage 65 V) forward and backward. Figure 2.8 shows a measured magnetic field in the x-axis, y-axis and z-axis components as a function of distance from the center of the magnet on the z axis with a flowing current of 300 A in the magnet.

An upper view of the trajectory of a charged particle is shown in Fig. 2.9. The turning angle θ is then

$$\theta = 2 \arcsin \frac{l}{2r} \tag{2.7}$$

where r is the curvature radius, l the chord length of the trajectory with a magnetic field. For simplicity, assuming that B_y does not depend on the x-axis position, and using Eq. (2.2) and the measured magnetic field (Fig. 2.8) at 100 mm intervals, the angle θ at which the travel direction of a charged particle with a momentum of 105 MeV/c bends with passing through ±1500 mm in the z-axial direction is then

$$\begin{aligned}\theta = 2 \times 2 \Bigg(& \arcsin \frac{100\text{ mm}}{2 \times 0.88\text{ m}} + \arcsin \frac{100\text{ mm}}{2 \times 0.88\text{ m}} + \arcsin \frac{100\text{ mm}}{2 \times 0.88\text{ m}} \\ & + \arcsin \frac{100\text{ mm}}{2 \times 1.4\text{ m}} + \arcsin \frac{100\text{ mm}}{2 \times 2.2\text{ m}} + \arcsin \frac{100\text{ mm}}{2 \times 3.5\text{ m}} \\ & + \arcsin \frac{100\text{ mm}}{2 \times 5.8\text{ m}} + \arcsin \frac{100\text{ mm}}{2 \times 8.8\text{ m}} + \arcsin \frac{100\text{ mm}}{2 \times 17.5\text{ m}} \Bigg) \\ = {} & 60^\circ. \end{aligned} \tag{2.8}$$

2.2.2 Tracking Detector

When charged particles pass through matter, the directions of their motion are changed due to scattering. To minimize the effect to the momentum resolution of the magnetic spectrometer, the tracking detectors should have small mass per unit length. Therefore, we use gas detectors, Multi-Wire Proportional Chambers (MWPCs) in the DeeMe experiment.

Requirements

Initially, it was planned to remove beam-prompt charged particles produced by pulsed proton beams with an electronic kicker magnet installed in the H Line to protect the detectors. However, due to the budget constraints, the proposal to install the electronic kicker magnet was abolished, and instead, multi-wire proportional chambers with tolerance to high rate was developed.

For using a target made of SiC, the number of beam-prompt charged particles which pass through the first multi-wire proportional chamber will be 1.9×10^8 particles, 1.4×10^4 particles/mm^2 at most or 70 GHz/mm^2 with a prompt-burst-pulse width of 200 ns (simulated by G4beamline). Upon being hit by such high rate charged particles, a multi-wire proportional chamber with the usual design will be unable to detect a charged particle for several tens of microseconds because a large amount of ions distort the electric field in the multi-wire proportional chamber (called space charge effect) and the gas amplification factor decreases. In the DeeMe experiment, we will search for a signal of muon to electron conversion, a delayed electron with a monochromatic energy of 105 MeV from 300 ns after the prompt burst pulses. Thus, the detectors need to restore the operation in a few hundreds of nanoseconds after receiving prompt burst pulses.

The following are the requirements of the detectors used for the DeeMe experiment:

- The detectors need to be tolerant to beam-prompt charged particles $\sim$ 70 GHz/mm^2.
- The detectors need to be able to detect an electron a few hundreds of nanoseconds after being hit by beam-prompt burst pulses.

Appearance of the multi-wire proportional chamber

Figure 2.10 shows a photo of one of the multi-wire proportional chambers used for the DeeMe experiment. We will use the cathode-strip-readout multi-wire proportional chamber with 80 channels in the x-axis direction and 16 channels in the y-axis direction. In the photo, it is seen that the cathode plane in the y-axis direction is taken and the wires are stretched. On the nearer side of the multi-wire proportional chamber, there are five connectors for the x-axis readout. There is a connector for the y-axis readout on the right side of the multi-wire proportional chamber. The multi-wire proportional chamber will be put with the nearer side facing the ceiling in the experimental area.

Structure of the multi-wire proportional chamber

When the beam-prompt charged particles pass through the detector, the gas gain is controlled by switching the applied voltage of the potential wires stretched alternately with the anode wires (called HV switching technique) in order to prevent the space charge effect. HV switching will be described in the later section.

Figure 2.11 shows a cross-sectional view of one of the multi-wire proportional chambers used in the DeeMe experiment. For the 713-type multi-wire proportional chamber, the wire spacing between an anode wire and potential wire is 0.7 mm, and the gap between the wire plane and cathode plane is 3 mm. Table 2.2 gives some list of parameters of the multi-wire proportional chamber structure used for the DeeMe experiment.

Since the distance between an anode wire and potential wire is smaller than the distance between the wire and cathode plane, the gradient of the electrical potential among anode and potential wires becomes dominant in determining the gas amplification factor. The capacitance between two wires per unit length is represented by

$$\begin{aligned} C &= \frac{\pi\epsilon}{\ln\left(\frac{s+\sqrt{s^2-4a^2}}{2a}\right)} \\ &\simeq \frac{\pi\epsilon}{\ln\left(s/a\right)}, \end{aligned} \tag{2.9}$$

where C is the capacitance between two wires, ϵ is the dielectric constant of filling gas, s is the wire spacing, and a is the radius of wire. Ignoring the thickness of anode and potential wires, and substituting $8.85 \times 10^{-12}\ \mathrm{F \cdot m^{-1}}$ for the dielectric constant ϵ, 0.7 mm for the wire spacing s, and 7.5 μm for the radius of anode wire, we thus have the capacitance between an anode wire and potential wire $C_{\mathrm{ano-po}}$,

$$C \simeq \frac{3.14 \times 8.85 \times 10^{-12}\ \mathrm{F \cdot m^{-1}}}{\ln\left(0.7\ \mathrm{mm}/7.5\ \mu\mathrm{m}\right)} \tag{2.10}$$

$$= 6\ \mathrm{pF/m}$$

$$C_{\mathrm{ano-po}} = 6\ \mathrm{pF/m} \times 0.3\ \mathrm{m} \tag{2.11}$$

$$\simeq 2\ \mathrm{pF}.$$

For the capacitance per an anode wire, this can be thought that two capacitors between anode and potential wire are connected in parallel, so that this is 4 pF. The total number of anode wires of 713-type multi-wire proportional chamber is, for example, 144, thus the capacitance of 144 anode wires and 145 potential wires will be 4 pF × 144 $\simeq$ 600 pF (0.6 nF).

Using a digital multimeter and touching the connector for applying high voltage to 144 anode wires and connector for 145 potential wires, the capacitance is about 0.5 nF.

When the voltage on potential wires is the same as that on anode wires during HV switching, the capacitance $C_{\mathrm{wire-cath}}$ between anode wires and cathode planes is approximately represented by

$$C_{\mathrm{wire-cath}} \simeq \frac{2\pi\varepsilon}{\frac{\pi L}{s} - \ln\frac{\pi d}{s}} \tag{2.12}$$

where L is the anode to cathode gap distance and d is the diameter of anode wire. Substituting $8.85 \times 10^{-12}\ \mathrm{F \cdot m^{-1}}$ for the dielectric constant ϵ, 3 mm for the distance between cathode and anode L, 0.7 mm for the wire spacing s, and 15 μm for the diameter of anode wire d, then

$$\begin{aligned} C_{\mathrm{wire-cath}} &\simeq \frac{2 \times \pi \times 8.85 \times 10^{-12}\ \mathrm{F \cdot m^{-1}}}{\frac{\pi \times 3\ \mathrm{mm}}{0.7\ \mathrm{mm}} - \ln\frac{\pi \times 15\ \mu\mathrm{m}}{0.7\ \mathrm{mm}}} \qquad (2.13) \\ &\simeq 3\ \mathrm{pF/m}, \end{aligned}$$

for the diameter of potential wire 50 μm,

$$\begin{aligned} C_{\mathrm{wire-cath}} &\simeq \frac{2 \times \pi \times 8.85 \times 10^{-12}\ \mathrm{F \cdot m^{-1}}}{\frac{\pi \times 3\ \mathrm{mm}}{0.7\ \mathrm{mm}} - \ln\frac{\pi \times 50\ \mu\mathrm{m}}{0.7\ \mathrm{mm}}} \qquad (2.14) \\ &\simeq 4\ \mathrm{pF/m}. \end{aligned}$$

When multiplied by one side length of the cathode plane of 0.25 m, that yields the capacitance of 1 pF.

Filling Gas

Passing radiation in a multi-wire proportional chamber filled with gas, the gas is ionized, and then electrons and ions are produced. The ionization electrons and ions are collected to make electronic signals for radiation detection.

The MWPCs in the DeeMe experiment will be used with filling argon-based mixed gases at 1 atmosphere. It is easy to operate the ionization and it is cheap, so that argon is often used for gas detectors. If one tries to obtain a gas gain 10^3 to 10^4 by using only argon, discharge is generated continually and the detector cannot be used. Here if some ethane or isobutane is added which is polyatomic gas, that prevents discharge due to energy consumption for elastic collision as a quencher. For using isobutane as a quencher, a small quantity of compound including fluorine is mixed to the gas to prevent after pulses. The optimization of filling gas in the DeeMe experiment is mentioned in a later section.

It is necessary to exchange gas enough because discharge tends to take place when gas exchange in the chamber is insufficient. Figure 2.12 shows the gas system for sending mixed gas to the multi-wire proportional chambers. It has flowmeters of argon, ethane, and carbon dioxide to mix those gases, and send it to the chamber.

Suppose to flow the mixed gas of argon and ethane 20 cc/min., respectively. The volume of 713-type multi-wire proportional chamber is height × width × depth = 467 mm × 612 mm × 56 mm $\simeq$ 16000 cc, so it takes

$$\begin{aligned} 16000\ \mathrm{cc} \div (20\ \mathrm{cc/min.} + 20\ \mathrm{cc/min.}) &= 400\ \mathrm{min.} \\ &= 6\ \mathrm{hours}\ 40\ \mathrm{min.} \end{aligned} \tag{2.15}$$

to fill the chamber once. Similarly, in the case of 724-type MWPC, it has a volume of height × width × depth = 518 mm × 674 mm × 58 mm $\simeq$ 20000 cc and it takes 8 hours 20 minutes to fill the chamber once. Generally, before operating multi-wire proportional chambers with a high voltage, gas is exchanged three and more times. To check how far along gas exchange is, we put an oximeter after the gas output of the chamber on the course of the exhaust. We apply the high voltage in the condition that at least oxygen density becomes smaller than 1000 ppm.

Because ethane and isobutane used as quencher is flammable gas, attention is paid to the dispose of the gas. The explosion limit of ethane and isobutane in the air are 3.0% to 12.5% and 1.8% to 8.4%, respectively. The output gas is exhausted after weakened with nitrogen gas so that the density becomes smaller than the upper limit of the explosion limit. For example, ethane of 20 cc/min. is flowed with nitrogen more than 650 cc/min. together.

High voltage switching technique

In order to control the gas gain of the multi-wire proportional chamber, the applied voltage of the potential wires is changed from 0 V to the voltage as high as that of the anode wires. We call it HV switching technique.

When the voltage as high as that on the anode wires is applied to the potential wires, the electric-field gradient between two kinds of wire becomes small and the gas gain becomes low. The gas gain is calculated to be the order of 10^4 when a potential difference between anode and potential wires is approximately 1500 V and the gas gain less than 10 when no potential difference. The relation of the average gas gain and applied voltage is mentioned in the later section.

The expected charged particles hitting the multi-wire proportional chamber and how the voltage is applied by HV switching are shown in Fig 2.13. For both of two methods, when the multi-wire proportional chamber is hit by the prompt burst pulses, there is no voltage difference between two kinds of wire, that is, no gas avalanche multiplication. After that, while we are searching for a signal delayed electron, the voltage difference is put to enable the gas multiplication.

By the method above in Fig. 2.13, when the prompt burst pulses pass through the detectors, no voltage difference is applied between anode and potential wires; for the rest of time, the voltage difference is large. By this method, due to the long time of a high voltage difference between the two kinds of wire, electric discharge between them is easy to occur.

By the method to apply high voltage below, we make the potential difference between the two kinds of wires large only during the measurement time we set (it is about 10 μs) and the detectors work for that time. This switching scheme was tested when we had beam time in the D2 area of J-PARC MLF in November, 2015, and it was confirmed that the frequency of discharge of the multi-wire proportional chamber becomes less in this method.

Module for HV switching

Figure 2.14 shows the module for HV switching. The input voltage into the module from the rear panel is DC voltage, and the output voltage is switched between DC high voltage and 0 V by inputting TTL signal into pulse IN. When the pulse IN is TTL high (low), the output voltage of the module becomes 0 V (the voltage input from the connector of the rear panel). The reason why the pulse IN gives a reverse response of the output voltage is to prevent that the output voltage becomes 0 V and the voltage between the two kinds of wires stays large when the pulse IN falls to 0 V for some reason.

Prompt burst of charged particles

The number of charged particles of the prompt burst pulse passing through the multi-wire proportional chamber is approximately 2×10^8 per pulse. When the prompt burst hits the multi-wire proportional chambers, the gas gain is reduced less than 10 by HV switching. The electric charge $q_{\rm prompt}$ induced in the detector by the prompt burst, for a gas gain of 10, is estimated to be

$$
\begin{aligned}
& q_{\text{prompt}} \\
& \qquad = \text{(The number of charged particles of prompt burst)} \\
& \qquad\quad \times \text{(number of initial ion pairs)} \times \text{(gas gain)} \times \text{(elementary charge)} \qquad (2.16) \\
& \qquad \simeq 2 \times 10^{8} \times 61 \times 10 \times 1.6 \times 10^{-19}\ \text{C} \\
& \qquad \simeq 20\ \text{nC}.
\end{aligned}
$$

For the cathode strip for the x-axis direction readout, because one-third of the charge is induced in one side of the cathode plane due to the shape of the electric field and it has 80 strips in the plane, the induced charge per channel will be 20 nC/3/80 $\simeq$ 80 pC/channel . Similarly, because there are 16 channels for the y-axis readout, that will be 20 nC/3/16 $\simeq$ 0.4 nC/channel for the y-axis readout strips.

The pulse signal of gas detectors is formed by ions moving to the cathode and the charge induced. The voltage as a function of time $V(t)$ induced in the electrode of the cylinder-shaped proportional counter is represented by

$$
\begin{aligned}
V(t) &= -\frac{q}{4\pi\epsilon l} \ln\left(1 + \frac{t}{t_0}\right), & (2.17) \\
\text{where } t_0 &= \frac{a^2\pi\epsilon}{\mu C V_0}, & (2.18)
\end{aligned}
$$

q is the electric charge, ϵ the dielectric constant of the gas, l the length of wire, μ the mobility, C the capacitance of the detector, V_0 the applied voltage to the detector, and a the radius of the anode wire. The electric charge $Q(t)$ we obtain as a signal is then

$$
\begin{aligned}
Q(t) &= ClV(t) \\
&= -\frac{qC}{4\pi\epsilon} \ln\left(1 + \frac{t}{t_0}\right) & (2.19)
\end{aligned}
$$

and the current $I(t)$

$$
\begin{aligned}
I(t) &= \frac{dQ(t)}{dt} \\
&= -\frac{qC}{4\pi\epsilon}\left(\frac{1}{t_0 + t}\right). & (2.20)
\end{aligned}
$$

If there are many charged particles incident to the detector, a long tail comes within sight in the form of pulse. Consider the signal of the proportional counter induced to a cathode strip. Inverting the sign of (2.20) and substituting $8.85 \times 10^{-12}\ \mathrm{F \cdot m^{-1}}$ for the dielectric constant ϵ, $1.5 \times 10^{-4}\ \mathrm{m^2/(V \cdot s)}$ for the mobility μ, 12 pF/m for the capacitance of the detector C, 1450 V for the applied voltage to the detector V_0, 0.75 μm for the radius of the anode wire a, we then find

$$\begin{aligned} t_0 &= \frac{(7.5\ \mu\mathrm{m})^2 \times \pi \times 8.86 \times 10^{-12}\ \mathrm{F/m}}{1.5 \times 10^{-4}\ \mathrm{m^2/(V \cdot s)} \times 12\ \mathrm{pF/m} \times 1450\ \mathrm{V}} \qquad (2.21) \\ &\simeq 600\ \mathrm{psec.} \end{aligned}$$

For the electric charge of 81 pC, the current $I(t)$ as a function of time is shown in Fig. 2.15. Since the actual prompt burst pulses have a width of about 200 ns, the signal form we observe would not be so steep as this figure.

Signal of 1 minimum ionizing particle (MIP)

Figure 2.16 shows the simulated number of initial ion pairs produced by an electron with an energy of 105 MeV incident to the thickness of the multi-wire proportional chamber of 6 mm filled with 1 atm argon (35%) ethane (65%). The horizontal axis represents the number of initial ion pairs, while the vertical axis is the frequency. The mean number of ion pairs created is 61 pairs, and the distribution has some spread from ten to a few hundreds due to statistical nature. The average energy to create an ion-electron pair is about 25 eV. If an incident particle creates 61 ion-electron pairs, the energy loss of the particle will be 1.5 keV. Figures 2.17 and 2.18 show the energy loss of an incident electron to the thickness of 6 mm filled with 1 atm gas and that versus the number of ion-electron pairs of the gas, respectively.

When 61 ion-electron pairs are multiplied with a gas gain of 10^4, the total charge q_{signal} which the multi-wire proportional chamber obtains as a signal will be

$$\begin{aligned} q_{\mathrm{signal}} &= (\text{Number of initial ion pairs}) \times (\text{gas gain}) \\ &\quad \times (\text{elementary charge}) \qquad (2.22) \\ &= 61 \times 10^4 \times 1.6 \times 10^{-19}\ \mathrm{C} \\ &\sim 0.1\ \mathrm{pC.} \end{aligned}$$

Deposited energy of an electron of 1 MIP to the multi-wire proportional chamber

Figure 2.19 illustrates an electron with a momentum of 105 MeV/c passing one multi-wire proportional chamber with its cross-sectional view. The total mass per unit area the electron passes is

$$\begin{aligned} & (18\ \mu\text{m aluminum}) + (75\ \mu\text{m kapton}) \\ & +(\text{gas of Ar } (50\%)\ \text{C}_2\text{H}_6\ (50\%),\ 27^\circ\text{C},\ 1\ \text{atm}) \qquad (2.23) \\ = & \ 18\ \mu\text{m} \times 2.7\ \text{g/cm}^3 + 75\ \mu\text{m} \times 1.4\ \text{g/cm}^3 \\ & +30\ \text{mm} \times 1.6 \times 10^{-3}\ \text{g/cm}^3 \\ \fallingdotseq & \ 2.1 \times 10^{-2}\ \text{g/cm}^2. \end{aligned}$$

Electrons with an energy more than approximately 1 MeV become Minimum Ionizing Particles (MIPs). The energy loss dE/dx is about 2 MeV/(g/cm^2), and the amount of energy deposited is

$$\begin{aligned} & 2.1 \times 10^{-2}\ \text{g/cm}^2 \times 2\ \text{MeV/(g/cm}^2) \qquad (2.24) \\ \sim & \ 40\ \text{keV}, \end{aligned}$$

when an electron passes one multi-wire proportional chamber.

2.3 Readout Electronics

A schematic diagram of the readout electronics system for the multi-wire proportional chambers is shown in Fig. 2.20.

2.3.1 Amplifier

After the signal is amplified, the output waveforms are sent to flash analog-to-digital converter (ADC). It is desirable for amplifiers to have excellent signal/noise ratio and stable baseline.

Requirements for amplifiers

Quantity of electric charge for a prompt burst pulse per one readout channel of the y-axis direction (0.4 nC) is approximately 4000 times bigger than that for the signal we search for (0.1 pC). The signal of the prompt burst pulse has a long tail, and it is necessary to separate the tail and a signal of muon to electron conversion.

When the voltage on the potential wires is switched between 0 V and 1500 V, the quantity of electric charge q_{hvs} that is to flow into one x-axis-readout strip with a width of 3 mm becomes

$$\begin{aligned} q_{\mathrm{hvs}} &\sim C_{\mathrm{wire-cath}} \times (\text{width of cathode strip}) \times (\text{switching voltage}) \qquad (2.25) \\ &\sim 4\ \mathrm{pF/m} \times 3\ \mathrm{mm} \times 1500\ \mathrm{V} \\ &\sim 18\ \mathrm{pC}. \end{aligned}$$

A charge of 18 pC is then input during the switching of the high voltage for several hundred nanoseconds. The amplifiers must have the tolerance for an electric current induced by high voltage switching and the prompt charged particles.

The following are the requirements of the amplifiers used for the DeeMe experiment:

- They must have the tolerance for a large electric current due to prompt charged particles.
- They must have the tolerance for that due to high voltage switching on the potential wires.
- They need to be able to separate a signal from long tails of prompt burst pulses.
- After being hit by prompt burst pulses, they need to be able to restore quickly and to amplify a signal of an electron.

Radeka-type two-stage amplifier

Radeka-type two-stage pre-amplifier was developed by M. Ikeno, M. Morii and T. Taniguchi, and the gain of which was raised from that of Radeka-type one-stage amplifier [27]. In the DeeMe experiment, Radeka-type two-stage amplifiers are used alone without post-amplifiers. Because that makes the readout system simpler and we can reduce production cost, Radeka-type two-stage amplifiers are now adopted after trial production and performance evaluation. The development of Radeka-type two-stage amplifiers is mentioned in [28] and Chapter 4.

Radeka-type amplifiers are charge amplifiers. Unlike voltage amplifiers whose outputs depend on the capacitance of the detector, charge amplifiers are also suitable for the use such as detectors that capacitance changes including the semiconductor detectors.

Because the signal from the multi-wire proportional chamber is weak, the amplifiers are attached with it as close as possible. Figure 2.21 shows a photo of the multi-wire proportional chamber with Radeka-type two-stage amplifiers. The 16 channels of amplifiers are integrated in one shield case.

Power supply board

Power supply boards are manufactured by the VME standard in order to supply Radeka-type two-stage amplifiers used for the DeeMe experiment. They are connected to the amplifiers by flat cables with a length of approximately 15 m. When a NIM standard logic signal is input from the LEMO connector of the front panel, test pulses can be sent to the 16 amplifiers connected.

Test pulse board

By rectangular wave of the NIM standard being input from the LEMO connector of the front panel, test pulses can be sent to multiple sets of 16-channel amplifiers at the same time. This is used for matching the timings of measuring equipments. In addition, by requiring coincidence of the accelerator triggers and logic signals which are slightly different from the accelerator triggers in the frequency, random pulses are generated and input in order to check if there is no event-mismatching among the flash analog-to-digital converters. Figure 2.22 shows a photograph of a crate with a test pulse board and some power supply boards.

2.3.2 Flash Analog-to-Digital Converter (FADC)

The output waveform from the amplifiers is sent to the flash analog-to digital converters (FADCs). The flash analog-to-digital converter developed for the TREK experiment is adopted (Fig. 2.23). It has an analog-to-digital count of 1024 counts (10 bits), a sampling frequency of 100 MHz (10 ns between two sample points), and a data-output speed of 100 Mbps to the network. Flash analog-to-digital converters are connected to the power supply boards of the amplifiers by 34-pin flat cables with a length of 1 m.

Figure 2.24 shows the crates of the readout electronics and gas system.

Table 2.2: The structure of multi-wire proportional chamber for DeeMe (713-type/724-type).

Material of anode wire	Gold-plated tungsten-rhenium Au-W(Re)
Material of potential wire	Gold-plated tungsten Au-W
Diameter of anode wire	15 μm
Total number of anode wires	144/136
Tension of anode wire	41 g
Diameter of potential wire	50 μm
Total number of potential wires	145/137
Tension of potential wire	80 g
Wire spacing between anode and potential wire	0.7 mm/0.75 mm
Length of wire	300 mm
Material of cathode	Aluminium (Al) mylar film
Width of cathode strip for x-axis readout	3.0 mm
Total number of cathode strips for x-axis readout	80
Width of cathode strip for y-axis readout	15 mm
Total number of cathode strips for y-axis readout	16
Gap between cathode and wire plane	3.0 mm

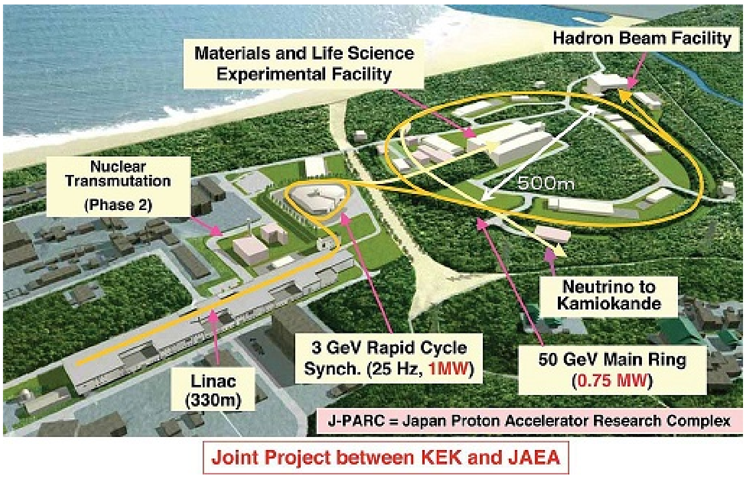

Figure 2.1: Bird's-eye view of J-PARC [21].

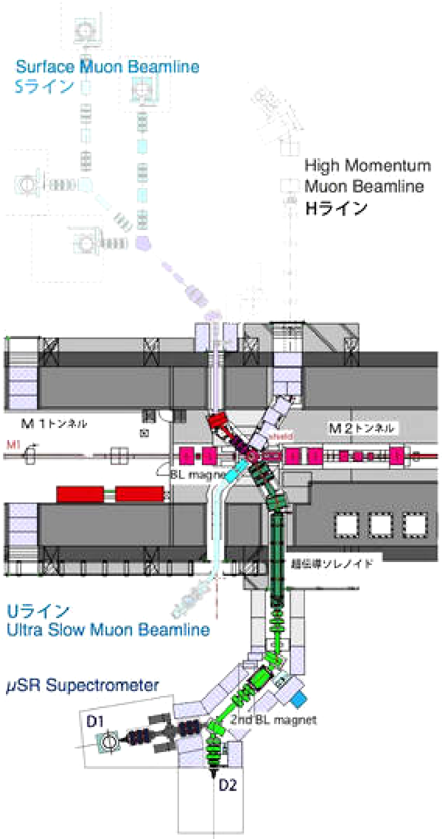

Figure 2.2: J-PARC MLF MUon Science Establishment (MUSE) [21].

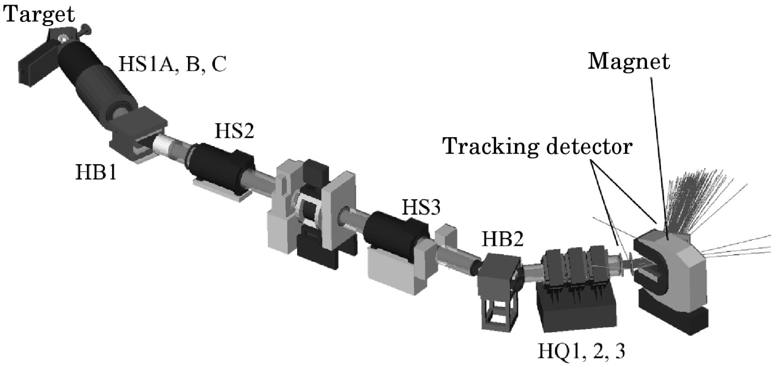

Figure 2.3: The H Line and magnetic spectrometer drawn by G4beamline.

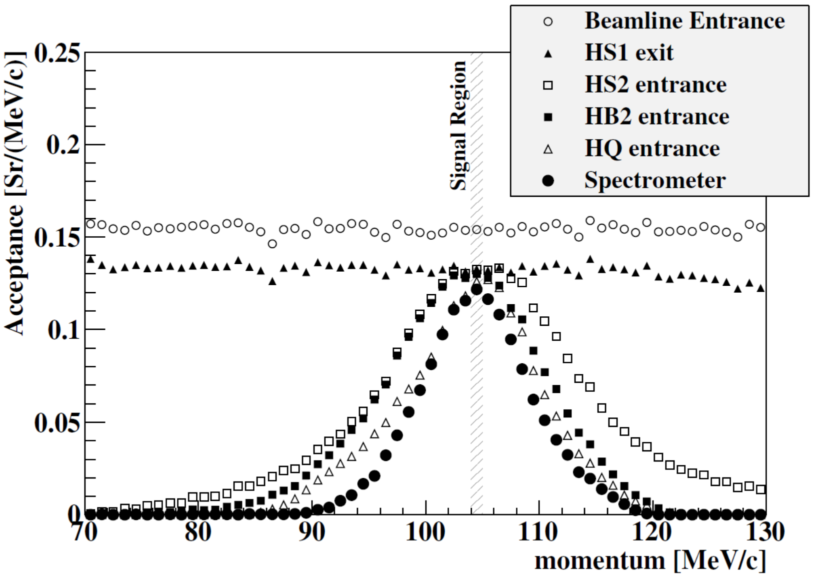

Figure 2.4: Acceptance of the magnets of the H Line and spectrometer as a function of momentum.

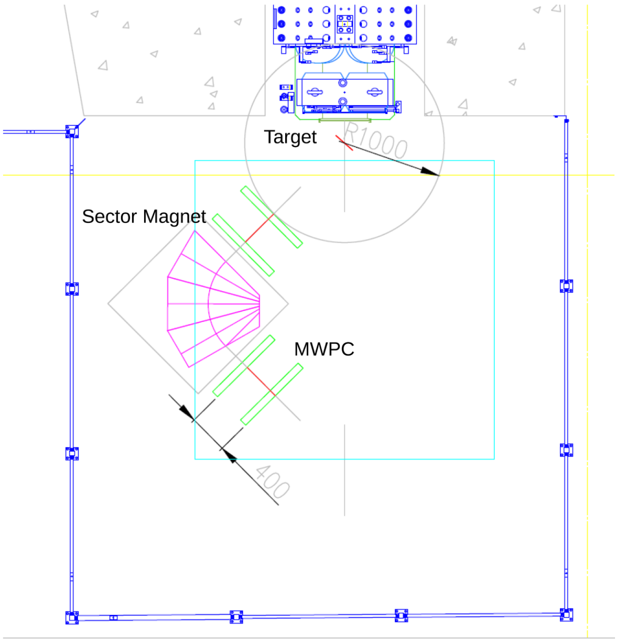

Figure 2.5: Floor plan of the experiment to measure the momentum spectra from the muon Decay in Orbit in the D2 Area.

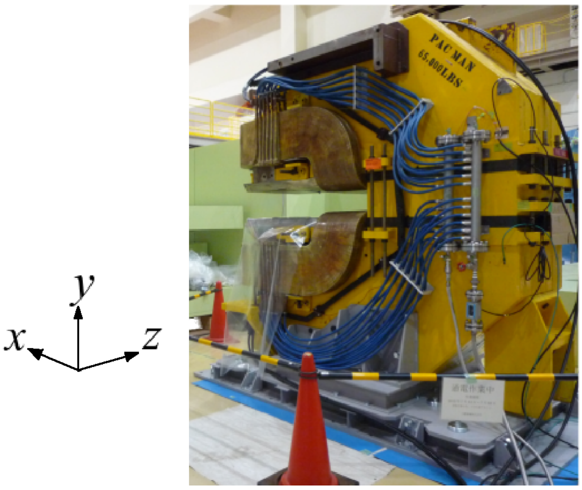

Figure 2.6: Photo of the dipole magnet called PACMAN which will be used for the DeeMe experiment.

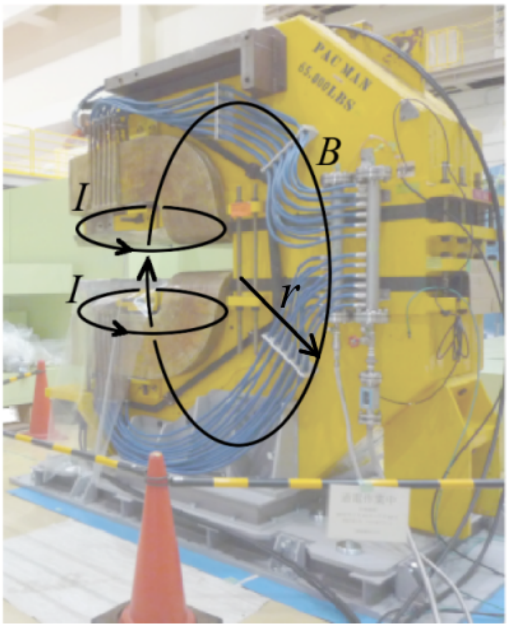

Figure 2.7: Calculation of the magnetic field of the dipole magnet.

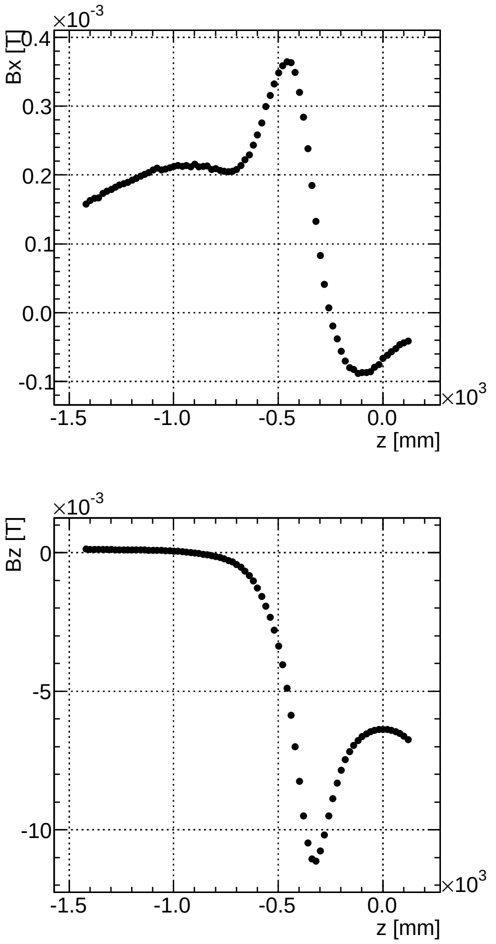

Figure 2.8: Measured magnetic field of the x-axis, y-axis and z-axis components as a function of distance from the center of the magnet on the z axis with flowing a current of 300 A in the magnet.

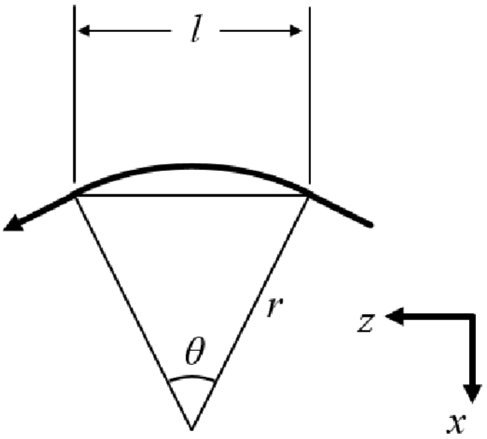

Figure 2.9: Trajectory of a charged particle from an upper view.

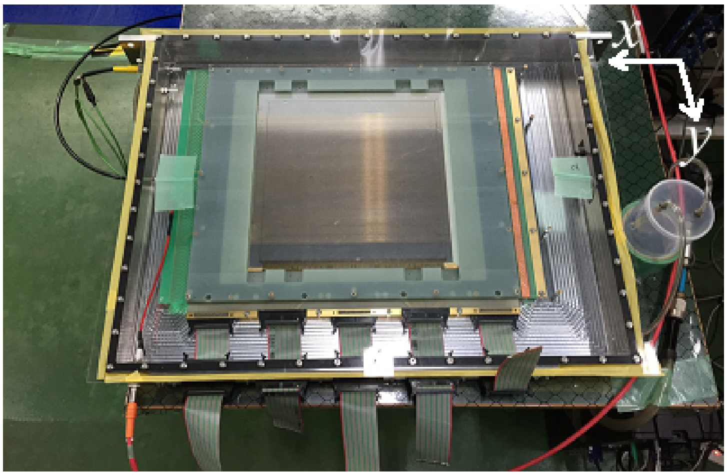

Figure 2.10: Photograph of a multi-wire proportional chamber for the DeeMe experiment.

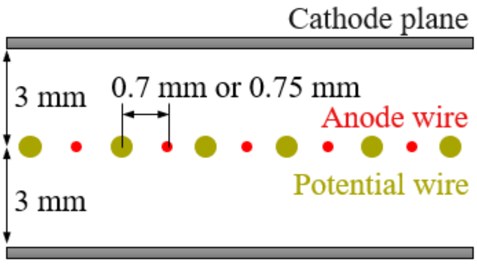

Figure 2.11: Sectional view of one of the multi-wire proportional chambers used in the DeeMe experiment.

Figure 2.12: Photograph of the system flowing mixed gas to the multi-wire proportional chambers.

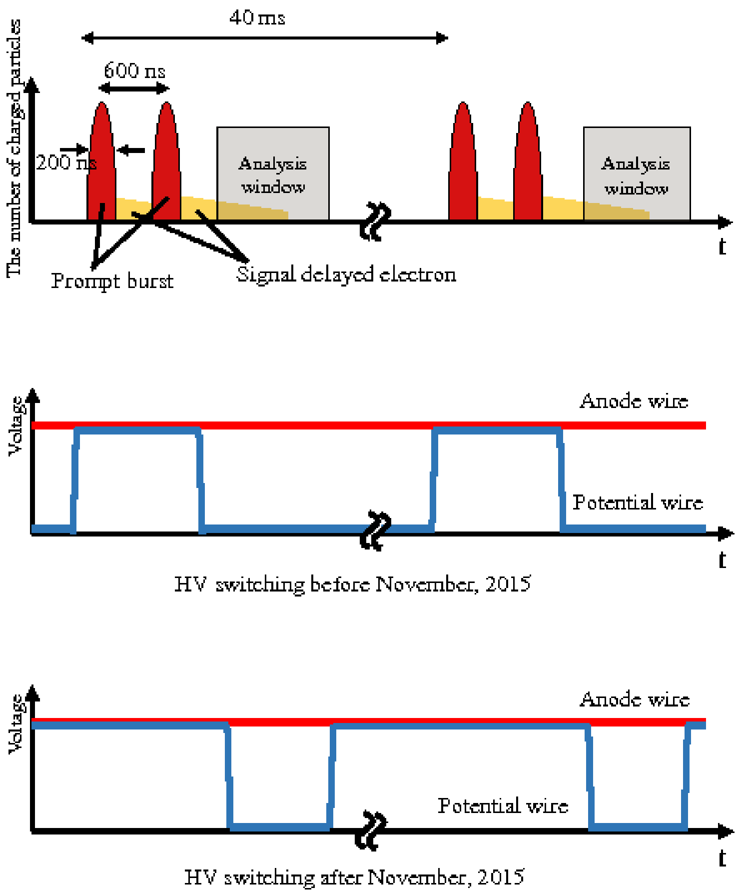

Figure 2.13: The expected charged particles hitting the multi-wire proportional chamber and how the voltage is applied.

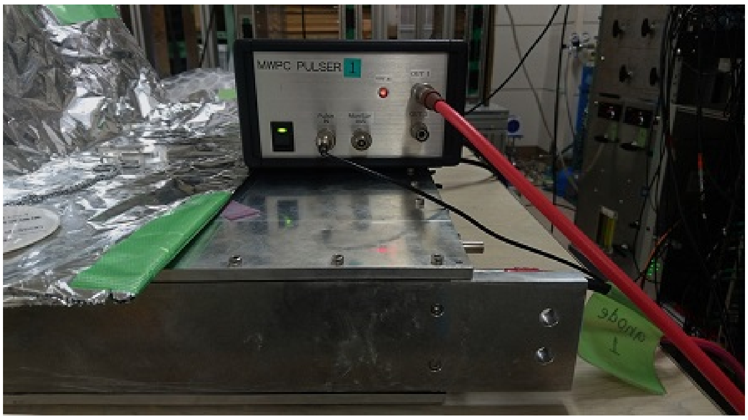

Figure 2.14: Photograph of the module used for HV switching.

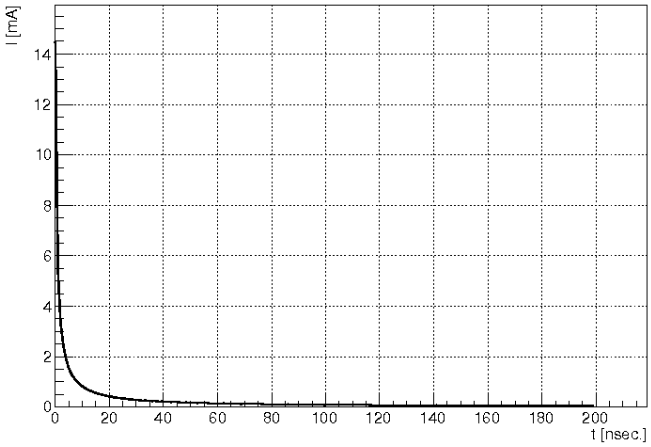

Figure 2.15: The current $I(t)$ of expected prompt burst as a function of time for the electric charge of 81 pC.

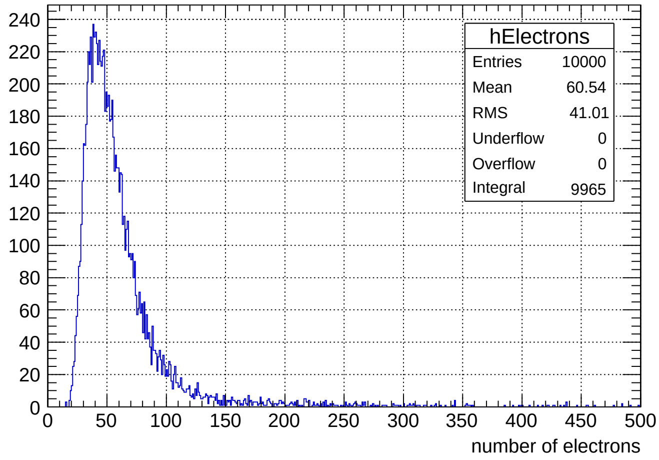

Figure 2.16: The number of initial ion pairs produced by an electron with an energy of 105 MeV incident to the thickness of the multi-wire proportional chamber of 6 mm filled with 1 atm argon (35%) ethane (65%) simulated by Garfield++.

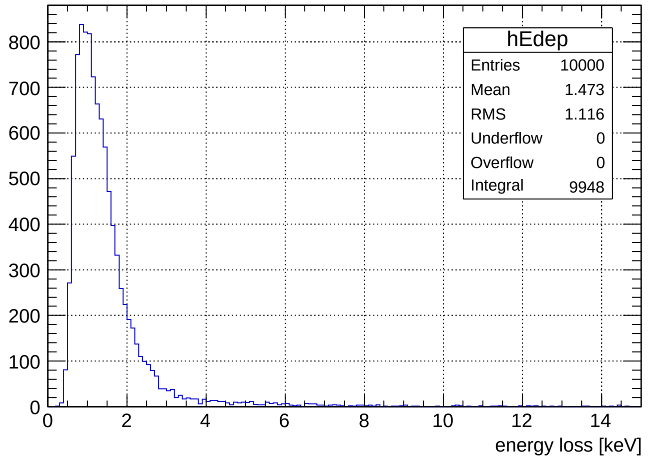

Figure 2.17: The energy loss of an incident electron with an energy of 105 MeV to the thickness of the multi-wire proportional chamber of 6 mm filled with 1 atm argon (35%) ethane (65%) simulated by Garfield++.

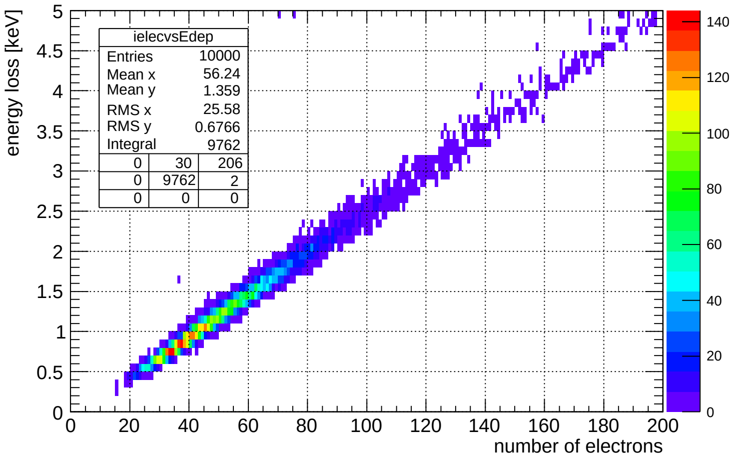

Figure 2.18: The energy loss of an incident electron versus the number of ionized electrons of the gas.

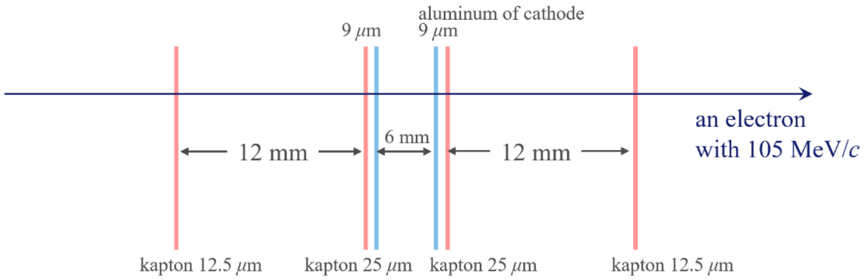

Figure 2.19: An electron with a momentum of 105 MeV/c passing one multi-wire proportional chamber and its cross-sectional view.

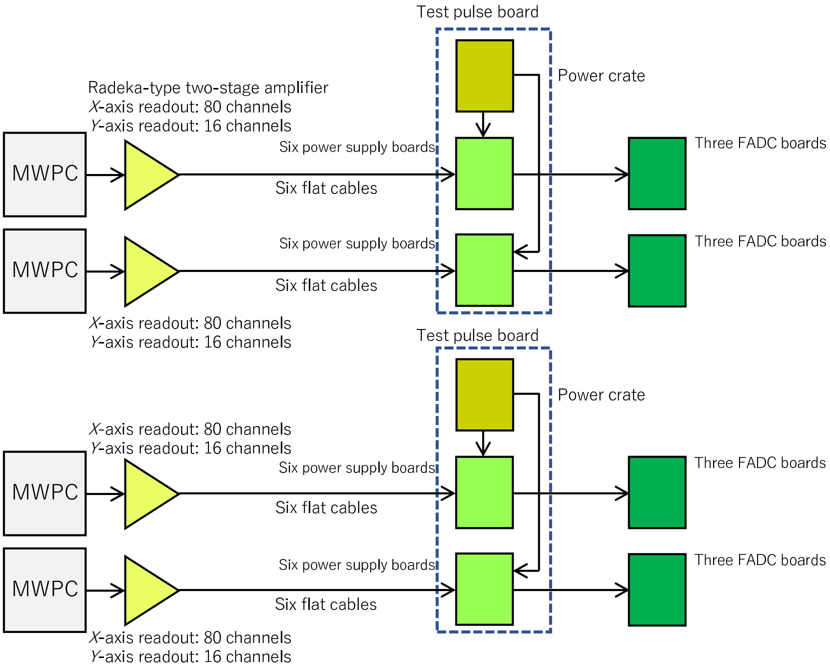

Figure 2.20: Diagram of the gas detectors, multi-wire proportional chambers, and their readout electronics.

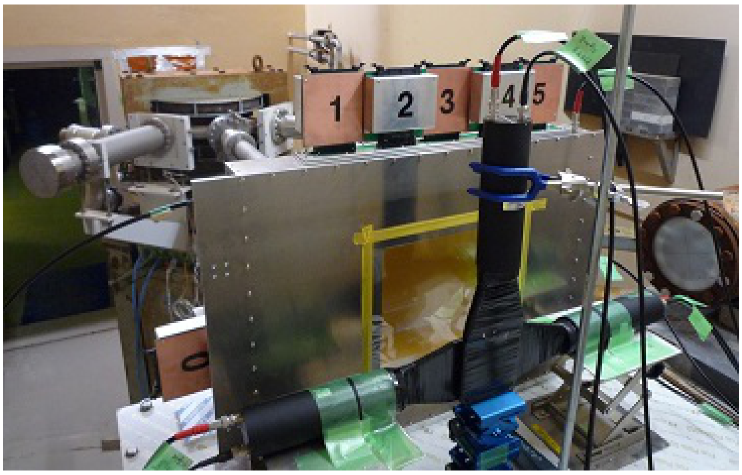

Figure 2.21: Photo of the multi-wire proportional chamber with 80 channels of x-axis and 16 channels of y-axis amplifiers.

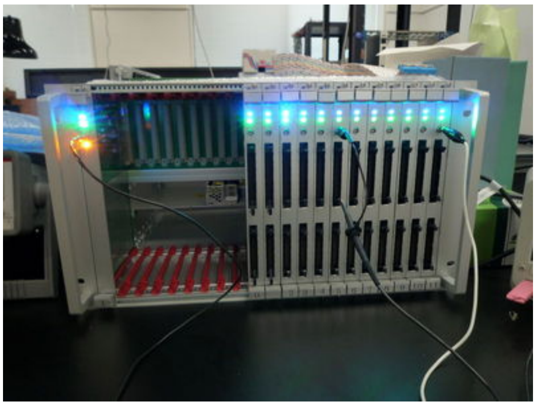

Figure 2.22: Photograph of a crate with a test pulse board and some power supply boards.

Figure 2.23: Photo of the flash analog-to-digital converter.

Figure 2.24: Photo of the readout electronics and gas system. Left: mass flow controllers of gas and oximater for the output from multi-wire proportional chamber(s). Center: logic circuits and high voltage supply modules. Right: power supply boards of the amplifiers and flash analog-to-digital converters.

Chapter 3

Development of the Detectors

In this chapter, the development of multi-wire proportional chambers (MWPCs), their amplifiers, and modules for high voltage switching is described.

3.1 Multi-Wire Proportional Chamber

The number of MWPCs used for the experiment is four in total. Two have a wire spacing of 0.7 mm (713-type), and the other two have a wire spacing of 0.75 mm (724-type). One of the 713-type MWPC was manufactured in 2015, and another one was done in 2016. Two of the 724-type were made in 2017. After having produced them, we performed tests to fill chambers with gas and to apply voltage in the laboratory at Tokai Building No.2, J-PARC. After successful test operation in the laboratory, the MWPCs were used for the measurement of momenta of electrons from muon decay in orbit in the J-PARC Materials and Life Science Experimental Facility D2 Area. They worked well. The filling gas was a mixture gas of argon 10 mL/min. ethane 20 mL/min. (1 atmospheric pressure), and the applied voltage was 1630 V to the 724-type MWPCs, or 1600 V to the 713-type MWPCs at the time of the experiment. The applied voltage was lower by 20 or 30 V than the value used for the operation check in the laboratory because the 713-type MWPCs with a wire spacing of 0.7 mm did trip frequently.

Afterwards it was planned to change ethane, used as quencher gas, to isobutane. The purpose is to prevent electric discharge by using the bigger molecule, and to make it easy to cause Penning effect, $\mathrm{Ar}^* + \mathrm{M} \rightarrow \mathrm{M}^+ + \mathrm{e}^- + \mathrm{Ar}$ (where M is a quencher molecule) because the ionization energy 10.7 eV of isobutane is lower than that of ethane 11.5 eV to make pulse height of the signal higher [29]. For changing the quencher gases, we investigated the electric discharge phenomenon between the wires in the gas.

3.1.1 Discharge Voltage

While the MWPC of the DeeMe experiment has a gas gain at the order of 10^4, high voltage is applied to anode wires, and 0 V is applied to potential wires. For stable operation of the MWPC, it is important that electric discharge does not occur between the two kinds of wire, and other places in the chamber.

Here Paschen's law on discharge between two electrodes will be summarized. An electron of the gas in the chamber, produced by ionization by charged particles, is accelerated by the electric field between the electrodes. When it has enough energy to ionize another gas molecule, continual ionization occurs. The number dn of new electrons produced is

$$dn = n\alpha dx \tag{3.1}$$

where $\alpha = 1/\lambda$ is the probability to cause ionization per unit length (λ is the mean free path of collisions that electrons causes the second ionization). By integrating, the total number of electrons created in a path d of distance between two electrodes will be

$$n = n_0 \exp(\alpha d). \tag{3.2}$$

Suppose that the original number of electrons n_0 is 1. The $\exp(\alpha d) - 1$ positive ions created are then accelerated in the electric field, and they collide with the cathode to produce $\gamma(\exp(\alpha d) - 1)$ electrons. This is repeated so that the total number of electrons will be

$$1 + \{\gamma(\exp(\alpha d) - 1\}^1 + \{\gamma(\exp(\alpha d) - 1\}^2 + \cdots . \tag{3.3}$$

This is a infinite geometric series with common ratio $\gamma(\exp(\alpha d) - 1)$. If the common ratio is greater than 1, there will be exponential growth towards positive infinity, that is, discharge occurs. Solving $\gamma(\exp(\alpha d) - 1) = 1$, this yields the boundary voltage to discharge,

$$\gamma(\exp(\alpha d) - 1) \;=\; 1, \tag{3.4}$$

$$\alpha d \;=\; \ln\left(1 + \frac{1}{\gamma}\right) \tag{3.5}$$

Here we adopt a model of α [30],

$$\frac{\alpha}{p} = A \exp\left(\frac{-Bp}{E}\right), \tag{3.6}$$

where p is the pressure, A and B are constants depending on the gas, and E is the electric field. Substituting into (3.5),

$$\begin{aligned} Apd \exp\left(\frac{-Bp}{E}\right) &= \ln\left(1 + \frac{1}{\gamma}\right) && (3.7) \\ \frac{Bp}{E} &= \ln \frac{Apd}{\ln\left(1 + \frac{1}{\gamma}\right)} && (3.8) \\ V &= \frac{Bpd}{\ln \frac{Apd}{\ln\left(1+\frac{1}{\gamma}\right)}}. && (3.9) \end{aligned}$$

The discharge voltage therefore depends on pd.

Figure 3.1 shows discharge voltage V as a function of distance d in case of argon, $p = 1013$ hPa, where $A = 8.63$, $B = 132$, $\gamma = 0.1$ [31]. Distance between an anode wire and a potential wire of the MWPC used for the experiment is 0.7 mm or 0.75 mm. The discharge voltage is proportional to distance of 10^{-4} m to 10^{-3} m.

Here the actual electric discharge test we performed is summarized. A wire with a diameter of 15 μm and wire with a diameter of 50 μm were tighten up in a small chamber, which were the same as the anode and potential wires of the MWPC. We kept the voltage 0 V on the wire of 50 μm and raised voltage on the wire of 15 μm slowly. We then investigated what voltage discharge occurs at. For this examination, the tools, which were used for determining the wire spacing of the MWPC, were utilized again: a wire of 15 μm made of tungsten rhenium gold-plated, a wire of 50 μm made of tungsten gold-plated, a G-10 board, a small chamber (a commercial plastic container for food sealed up using seal material LOCTITE 5699), gases (argon, ethane, isobutane), iseg HV power supply, and gas-flowing system [32]. Figure 3.2 shows the small chamber and tighten-up wires for this experiment.

Tables 3.1 to 3.6 give lists of results of discharge voltage. Blank columns mean there is no data because the wires have broken. The operation voltage will be detemined by taking acount of these discharge voltages and the gas gain summarized in the later sections.

Table 3.1: Discharge voltage [V] and wire spacing for argon (50%) ethane (50%) at 1 atmosphere.

wire spacing [mm] discharge	0.465	0.568	0.662	0.686
1st	1500.2	1831	1950.5	1850
2nd	1350	1430	1850.2	1750
3rd	1400.7	1756	1900.9	1890.3
4th	1410	1600	1850.7	1750
5th	1487	1551.6		1820.4

Table 3.2: Discharge voltage [V] and wire spacing for argon (60%) ethane (40%) at 1 atmosphere.

wire spacing [mm] discharge	0.465	0.568	0.662	0.686
1st	1350.3	1450.1		1750.1
2nd	1380.5	1400		1551
3rd	1350.3	1450.5		1551.3
4th	1350.4	1480.4		1601.2
5th	1450.6	1550.4		1550.2

Table 3.3: Discharge voltage [V] and wire spacing for argon (70%) ethane (30%) at 1 atmosphere.

wire spacing [mm] discharge	0.465	0.568	0.662	0.686
1st	1400.6	1380		1500.5
2nd	1351	1451.3		1451.2
3rd	1330.5	1350		1521.7
4th	1250.2	1400.7		1630
5th	1200.7	1400.5		1550.9
6th	1280			1550.2
7th	1251			1550.2

Table 3.4: Discharge voltage [V] and wire spacing for argon (80%) isobutane (20%) at 1 atmosphere.

wire spacing [mm] discharge	0.614
1st	1769
2nd	1573
3rd	1735
4th	1723
5th	1728
6th	1713
7th	1685
8th	1707
9th	1687

Table 3.5: Discharge voltage [V] and wire spacing for argon (90%) isobutane (10%) at 1 atmosphere.

wire spacing [mm] discharge	0.614
1st	1424
2nd	1384
3rd	1464
4th	1431
5th	1207
6th	1442

Table 3.6: Discharge voltage [V] and wire spacing for argon (100%) at 1 atmosphere.

discharge \ wire spacing [mm]	0.614
1st	865
2nd	868
3rd	575
4th	872
5th	884

3.1.2 Simulation of Gas Gain versus Applied Voltage

Relation between pulse height of signals of the MWPC and applied voltages is simulated using a simulator of tracking detectors Garfield++ [33]. In the simulation, two cathode planes are put at a distance of 3 mm away from the anode plane. The wires have a length of 30 cm. For the wire spacing, two kinds of 0.7 mm and 0.75 mm are simulated. In the chamber, mixture of argon ethane or that of argon isobutane is filled at 1 atmosphere in 20 degrees Celsius (293.15 K). Cathode and potential wires then are 0 V, while high voltage is applied to the anode wires for gas multiplication. In this condition, one electron is put in the random place within 150 μm from the center of an anode wire,

$$x = r\cos(2\pi \cdot \mathrm{Rndm}()) \tag{3.10}$$

$$y = r\sin(2\pi \cdot \mathrm{Rndm}()) \tag{3.11}$$

$z = 0$, where x is the direction in which the wires are lined, y the direction perpendicular to the wire plane, z the direction of the wire axis, $r = 150$ μm, Rndm() the random number uniformly distributed from 0 to 1. After having caused the avalanche amplification, the mean number of positive ions are investigated to determine the gas amplification factor. The number of electrons will be the number of ions plus one that is the original electron.

Simulation results are summarized in Fig. 3.3 for a wire spacing of 0.7 mm and Fig. 3.4 for that of 0.75 mm. The size of the error bar of the vertical axis corresponds to the root mean square divided by the square root the number of entries.

The results of simulated mean gas gains M as a function of applied voltage V are expressed in

$$M = a \cdot \exp(b \cdot V), \tag{3.12}$$

and the constants a and b are summarized in Tables 3.7 and 3.8.

Table 3.7: The values of a and b in simulation of gas gain versus applied voltage of the MWPC with a wire spacing of 0.7 mm.

Gas mixture	a	b [V^{-1}]
Argon (35%) ethane (65%)	3.12×10^{-3}	1.02×10^{-2}
Argon (50%) ethane (50%)	3.84×10^{-3}	1.04×10^{-2}
Argon (50%) isobutane (50%)	2.30×10^{-3}	9.83×10^{-3}
Argon (80%) isobutane (20%)	1.99×10^{-2}	9.84×10^{-3}
Argon (90%) isobutane (10%)	1.10×10^{-2}	1.07×10^{-2}

Table 3.8: The values of a and b in simulation of gas gain versus applied voltage of the MWPC with a wire spacing of 0.75 mm.

Gas mixture	a	b [V^{-1}]
Argon (35%) ethane (65%)	4.76×10^{-3}	9.85×10^{-3}
Argon (80%) isobutane (20%)	7.72×10^{-3}	1.04×10^{-2}
Argon (90%) isobutane (10%)	1.21×10^{-2}	1.06×10^{-2}

3.1.3 Measured Pulse Height

Data of the MWPC waveform is taken as a MIDAS [34] file using FADCs with a sampling rate of 100 MHz. Starting ROOT [35], waveform analysis then is performed by loading scripts of OCUHEP [36] package.

The rough flow of analyzing pulse height of the signals of the MWPC is described in this section:

1. Template waveforms are subtracted.
2. Peaks are found.
3. ADC counts are summed up in the directions of time and strip.
4. Threshold of the ADC count is determined and signals are defined.

Original waveform and subtracting template waveform

The high voltage to potential wires is switched as shown in Fig. 2.13 (below). The output waveform therefore includes a noise pattern generated by the HV switching. It is shown in Fig. 3.5 when a direct voltage of 1630 V is applied to anode wires, and switching voltage of 0–1630 V is applied to potential wires. One count on the vertical axis is 2 mV. In the waveform, a voltage of 1630 V is applied to potential wires until -2.8 μs. They become then electrically floating at the time of -2.8 μs. From -1.9 μs, the voltage begins to fall, and the output waveform is saturated in negative. Due to a pole-zero cancellation circuit of the amplifier, the waveform has a positive spike at the time of -0.7 μs. After that, potential wires are 0 V until 8.1 μs, and the gas gain is on the order of 10^4 to operate the MWPC. During the period of time, oscillation is seen on the waveform. From the time of 8.1 μs, voltage on potential wires started to rise up to the original high voltage. The next operational window will come after approximately 40 ms.

The oscillation occurring in the operating time of the MWPC is the same form every trigger. When we do hit-finding, waveform of the most frequent ADC counts of waveforms (shown in the figure with red) are subtracted from an event waveform (black) to create a subtracted waveform (blue). Then the oscillation is eliminated well, and signal peaks at 1.0 μs, 1.1 μs, and 2.7 μs can be seen for this event.

Finding peaks

Signals with various pulse height that are found in the way above are shown in Fig. 3.6. The time width of the signals does not seem to depend on pulse height. To find signals without bias, when seven times of sample points larger than 1 ADC count (small threshold) continue in succession, the highest sample point is looked for from the first point to the point after twenty points (for 200 ns).

Summing up ADC counts in the directions of time and channels

To raise signal to noise ratio, ADC counts are summed up from the point ten points before the highest sample point to the point five points after that point. If points too behind are used to sum up, the sum is reduced by the waveform sinking from a pole-zero cancellation circuit of the amplifier. In addition, the sums of ADC counts are similarly evaluated for the two adjacent cathode strips next to the cathode strip that a peak is found in.

Figure 3.7 shows a histogram of the sum of ADC counts in the direction of time of one cathode strip (black histogram). In the histogram, the part of signals overlaps with pedestal. But if it is required that the sum of ADC counts of the channel that a peak is found in is larger than those of two adjacent channels, signals are separated from pedestal (as shown in red histogram). And when the sum of the furthermore cathode strips is required to be larger than that of two adjacent channels, the amount of pedestal decreases and the entries of signals do not change (blue histogram). In this section, we adopt the condition that the sum of ADC counts of the cathode strips that a peak is found in is larger than the sums of two adjacent cathode strips.

Histograms of the sums of ADC counts of one (black), three (red), and five (blue) cathode strip(s) are shown in Fig. 3.8. When the data was taken, the MWPC with a wire spacing of 0.75 mm between an anode wire and a potential wire was filled with gas mixture of argon (80%) isobutane (20%), to which 1510 V was applied and electron beam was injected. Comparing the sum of three strips with that of five strips, the pulse height of signals does not seem to change. Therefore, the size of avalanche is found to be smaller than the width of three cathode strips (3 mm $\times$ 3 strips).

Threshold determination and signals definition

When the sum of ADC counts of three cathode strips is larger than 500 counts in Fig. 3.8, we define them as signals. Making a histogram of the highest ADC count of signals yields Fig. 3.9. It has a mean of 147.4 counts, that is, 294.8 mV.

Analysis of the Y-axis direction readout

At present, the channels of the Y-axis direction readout of the MWPCs are bundled up from five strips with a width of 3 mm, that is, 15 mm. The oscillation of the output waveform in the Y-axis readout during the MWPC operation therefore was seen about five times larger than that in the X-axis readout. To prevent the readout amplifiers from being saturated due to oscillation, new amplifiers for the

Y-axis readout (version 2) were produced in the early months of 2017, which have approximately one-third gain of amplifiers for the X-axis readout. The development of readout amplifier for the Y-axis readout will be mentioned in the later section.

A waveform of a cathode strip for the Y-axis direction readout of the MWPC is shown in Fig. 3.10. Amplifiers of version 2 was used, and electron beam was incident into the MWPC with a wire spacing of 0.75 mm, filled gas mixture of argon (80%) isobutane (20%), and 1510 V applied. After subtracting a template waveform as described above, a signal is seen. If the diagram is zoomed in (see Fig. 3.11), the time width of the signal on the Y-readout seems to be comparable with that on the X-readout. In the same way, if seven sample points larger than 1 count (that is a small threshold) continue in succession, we look for a peak, the highest sample point from the first point to the point 20 points after that (during 200 ns). The ADC counts then is summed up from the point 10 points before the highest point to the point 5 points after that. For the two channels next to the channel that a peak is found in, the sum in the direction of time is calculated as well.

Figure 3.12 shows histograms of the sums of ADC counts of one channel (black) and three channels (red) in the direction of time. For the Y direction readout, due to picking up a lot of noises with three channels (3 mm width cathode strip ×5 strips/channel ×3 channels=45 mm width), signals are not separated from pedestal in the histogram. In the case of one channel, they are not completely apart from pedestal, but the sums of ADC counts larger than 100 counts are defined as signals. The highest ADC counts in the signals are shown in a histogram of Fig. 3.13.

Histograms for various voltages and filling gases

Figures 3.14 to 3.19 show histograms of the sum of ADC counts and the highest ADC counts for X- and Y-readout, with filling gas argon (80%) isobutane (20%), and high voltage of 1540 V applied, and for X-readout, with filling gas argon (33.3%) ethane (66.6%), the high voltage of 1650 V applied. Because amplifiers for the Y-axis readout (version 2) was not yet developed when data of argon (33.3%) ethane (66.6%) with high voltage of 1650 V applied in May, 2016, pulse height of the Y-readout could not be analyzed.

Bench test using ^{55}Fe source

Pulse height of the MWPC when electron beam from an accelerator enters it has been described so far. From now on, bench tests using a source ^{55}Fe in the laboratory of the DeeMe group at Tokai Building No. 2, J-PARC are described.

Simulation of X rays incident on the MWPC

First, Fig. 3.20 shows the number of electrons created when X-rays are injected into the active area of the DeeMe MWPC, simulated using Garfield++. In the simulation, X-rays perpendicular to the window of the MWPC are incident on the MWPC with a wire spacing of 0.7 mm and a gap between two cathode planes of 6 mm. As we see a peak at 0 electron, approximately 95% of X-rays go through the chamber without reacting. The histogram mainly has two peaks:

1. A peak of 230 electrons is produced by the photoelectric effect and the emission of Auger electron. The photoelectrons are emitted with an energy of 2.7 keV since 3.2 keV is necessary that X-rays with an energy of 5.9 keV of ^{55}Fe react with the electron of the innermost shell of argon atoms. After deexcitation, electron (called Auger electron) with an extra energy of 3.2 keV is emitted. Because these two kinds of electron produce electron-ion pairs with every of energy 25 eV, (2.7+3.2) keV/(25 eV/1 pair)$\simeq$230 pairs, that is, 230 electrons will be created.
2. A peak of 120 electrons is made by the photoelectric effect, emission of X-ray and Auger electron with remaining energy. After X-ray with an energy of 5.9 keV from ^{55}Fe causes the photoelectric effect, the argon atom is in a state with an energy level of 3.2 keV from the ground state. It emits a characteristic X-ray with an energy of 2.9 keV, and is in a state with an energy level of 0.3 keV. Auger electron is then emitted with an energy of 0.3 keV. Therefore the photoelectron and Auger electron will create (2.7+0.3) keV/(25 eV/1 pair)$\simeq$120 electron-ion pairs.

The fractions of reaction 1 and 2 occur are 85% and 15%, respectively.

About ^{55}Fe source in the Tokai Building No. 2, J-PARC

It is written that the decay rate was 8.43×10^5 Bq on June 18th, 2013. The data analyzed in this section were taken in January, 2018. ^{55}Fe has a half-life of 2.7 years. If we think four and a half years pass, the decay rate will be

$$\begin{aligned} & 8.43 \times 10^5 \text{ Bq} \times \exp(-\lambda t) \qquad (3.13) \\ = \; & 8.43 \times 10^5 \text{ Bq} \times \exp\left(-\frac{\ln 2}{2.7 \text{ years}} \times 4.5 \text{ years}\right) \\ = \; & 2.66 \times 10^5 \text{ Bq} \end{aligned}$$

in January, 2018, where λ is the decay constant.

Analysis of pulse height using ^{55}Fe

Figures 3.21 to 3.24 show histograms of the sum of ADC counts and the highest ADC counts for data of the 724-type MWPC X- and Y-direction readout using ^{55}Fe source. When the data were taken, the MWPC is filled with gas mixture of argon (80%) isobutane (20%) and 1510 V applied. Peaks is seen at the position of 1500 counts in the histogram of the one-cathode strip sum of ADC counts (black) and at 2500 counts in that of the three-cathode strip sum (red). This seems to be the main peak by X-rays. For the black histogram, thinking of the sum larger than 600 counts as signals, histograms of the highest ADC counts for one cathode strip and the sum of the highest ADC counts for three cathode strips are shown in Fig. 3.22. For the Y-direction readout, the main peak is not completely apart from pedestal as shown in Fig. 3.23. But we think the sum of ADC counts larger than 100 counts as signals. Figure 3.24 shows histograms of the sum of the highest ADC counts for one cathode strip (black) and the sum of the highest ADC counts for three cathode strips (red) of signal.

Here we consider the number of entries of signals. To store the histograms, 100,000 triggers were used with an analysis window width of 7 μs per trigger. Because it was 2.66^5 Bq as of January, 2018, the events in the analysis windows will be

$$2.66 \times 10^5 \text{ Bq} \times 7\ \mu\text{s/trigger} \times 100,000 \text{ triggers} = 1.86 \times 10^5 \text{ events}, \qquad (3.14)$$

and if we think half solid angle of them enter the MWPC, the event will be about 93,100 events. From Fig. 3.20, 4% of X-rays generates the main peak signals so that it will be 93,100 events$\times 0.04 \simeq$ 3,800 events. This calculation agrees well with the entries which are found in finding-peak algorithm.

Summary of measured pulse height

Figure 3.25 shows the summary of the analysis result of the sum of the highest ADC counts of three cathode strips for various gas mixture with electron beam and X-rays of ^{55}Fe versus applied voltage.

Comparing pulse height of the Y-direction readout with that of the X-direction readout, the ratio of pulse height should be the ratio of the amplifier gain, 1.9 V/pC and 6.9 V/pC, but it does not seem to be so. It can be thought that the Y-readout has a lower signal to noise ratio and small signals are rejected due to the threshold, which results in a higher average value of the pulse height.

Next, we compare the result of electron beam with that of X-rays ^{55}Fe. While the mean number of initial ions is 60 for electron beam, that is 230 for the main peak of X-rays. The ratio of those pulse height should be the number of initial ions, but that does not seem to be so. The signals in the histogram for electron beam look well apart from pedestal. While photoelectron of X-rays loses the energy of 2.7 keV to travel 5.4 mm on average, and Auger electron loses the energy of 3.2 keV to travel 6.4 mm on average, they hit the cathode planes or wires in the active volume of the MWPC, and it is thought the number of initial ion pairs decreases.

For the result of gas mixture of argon (33.3%) ethane (66.6%), because signals and pedestal are not completely apart, assuming that the highest ADC counts is proportional to the sum of ADC counts of one cathode strip in the direction of time, the highest ADC counts is calculated.

Comparison between gas gain simulation and pulse height analysis

Consider the case that electron beam enters the MWPC with a wire spacing of 0.75 mm, filled with gas mixture of argon (80%) isobutane (20%), and 1540 V applied. When an electron is incident on the MWPC, 61 initial ion pairs on average are generated as shown in Fig. 2.16. The gas amplification is 6.4×10^4 in the simulation as shown in Fig. 3.4. Signals generated from the avalanche amplification are then amplified with a gain of 6.9 V/pC. The pulse height will be

$$
\begin{aligned}
& \text{(the number of initial ion pairs)} \times \text{(gain)} \times \text{(elementary charge)} \times \text{(gain of amplifier)} \\
& \times\text{(fraction of charge moving to one cathode plane)} \\
& \times\text{(fraction of charge moving to one cathode strip)} \qquad (3.15) \\
\simeq\ & 61 \times 6.4 \times 10^{4} \times 1.6 \times 10^{-19}\ \mathrm{C} \times 6.9\ \mathrm{V/pC} \times \frac{1}{3} \times \frac{1}{3} \\
\simeq\ & 480\ \mathrm{mV}.
\end{aligned}
$$

In Figure 3.9, the typical pulse height is 200 ADC counts, that is, 400 mV, and the simulation approximately agree with the analysis result.

Stability of operation

The operation voltage of the MWPC is determined by consideration of the pulse height that we obtain and the electric discharge between an anode wire and a potential wire. The discharge voltage versus wire spacing is shown in Fig. 3.26. It seems to approximately have proportional relation just like the Paschen's law of discharge. Figure 3.27 shows the required voltage to get a gas gain of 4.6×10^{4} in the vertical axis versus the electric discharge voltage calculated for a wire spacing of 0.7 mm in the horizontal axis. The margin between the required voltage and the discharge voltage is the largest for the argon (80%) isobutane (20%), the next argon (50%) ethane (50%), then argon (90%) isobutane (10%). Note that the discharge voltages are measurements, not simulation results.

3.2 HV Switching Module

In MWPC operation, we see oscillation in the output waveform. One of the possible causes is that the HV switching circuit oscillates electrically. We tried to suppress the oscillation by modifying the circuit. The issue could not be resolved after all, but some of the tests are mentioned in this section because it may become tips to resolve the problem in the future.

3.2.1 Influence of Oscillation Problem on Hit Efficiency

Hit efficiency is investigated using the data of the experiment at J-PARC MLF D2 Area in June, 2017. Tracks of positrons produced by positive muons hitting a carbon target are reconstructed by the spectrometer. The hit efficiency is estimated by counting the number of hits found by the hit-finding algorithm in one MWPC and dividing it by the number of tracks reconstructed using the three MWPCs excluding the MWPC in question. Hit efficiency as a function of time for the second and the fourth MWPC from upstream at the D2 Area (see Fig. 2.5) is shown in Figs. 3.28 to 3.31 (The first and second were the 724-type MWPCs with a wire spacing of 0.75 mm, and the third and fourth were the 713-type MWPCs with a wire spacing of 0.7 mm. The reason we choose the second and fourth ones is because the efficiencies are lower than those of the first and third ones, respectively.). Hit efficiency of the second MWPC X-readout is approximately 90%, but it is 80% right after the operation begins. That of the Y-axis readout is about 40%.

Because trip frequently occurred during the experiment due to small wire spacing of 713-type MWPCs, they were operated at a lower voltage of 1600 V than the nominal voltage of 1620 V. It is analyzed that hit efficiency of the X-readout and Y-readout of the fourth MWPC is approximately 50% and 25%, respectively.

Now, when we do tracking with four MWPCs it is required that all of the four MWPCs X-readout have a hit. Product of the individual hit efficiency of four MWPCs X-readout is then shown in Fig. 3.32. It is analyzed to be about 30%. Just after detectors begin to work it seems to be 20%. The efficiency oscillates as the original output waveform oscillates.

3.2.2 Internal Circuit

Figure 3.33 shows a simplified circuit diagram in the HV switching module. It has two N-channel power MOSFET WPH4003 (reference Q1 and Q2) of ON Semiconductor. While Q1 is a switch of the high voltage side, Q2 is that of 0 V. They work as follows:

1. The high-voltage input (having a label of 1650 V) is connected to the output of HV switching module (having a label of OUT_SHV), that is, the drain (a label of D) of Q1 is electrically connected to the high voltage input.
2. The output floats, that is, the drain of Q1 is unconnected to the source.
3. The ground is connected to the output of HV switching module, that is, the drain of Q2 is connected to the ground.

4. The output floats, that is, the drain of Q2 is unconnected to the source.
5. 1. to 4. are repeated.

Voltage differences between the gate and source (a label of S) control whether the drain is connected or not. Single gate drivers model number UCC27531 of TEXAS INSTRUMENTS (reference U1 and U2) make voltage differences. The circuit in front of them is abbreviated.

A resistor (R4) of 100 Ω, and a snubber circuit consisting of a capacitor (C10) of 100 pF and a resistor (R5) of 10 Ω are attached to study suppressing the output-waveform oscillation. An equivalent circuit of coaxial cable is represented by inductance L1, L2, L3, and capacitance C7, C8 and C9.

Figure 3.34 shows a photograph of a circuit in HV switching module. Two MOSFETs, two connectors for output, a connector for TTL input, and other electric parts are reflected in this photograph. As we can see, the snubber circuit and resistor R4 added in series are point-to-point-constructed at this juncture.

3.2.3 Simulation

HV switching circuit, an MWPC, and a readout amplifier are simulated using a circuit simulator LTspice [37]. Figure 3.35 shows a whole simulation model of them. It has a HV-switching circuit model leftmost.

Next, 143 anode wires, 143 potential wires, and cathode strips are drawn in the model. In the simulation, while direct current high voltage is applied to anode wires, switching voltage is applied to potential wires from the HV switching module. The wires are expressed all at once in two steps of sub-circuit. Figure 3.36 show a model of 20 anode wires, 20 potential wires, and cathode strips. This is described in ten sub-circuit sets of two anode wires, two potential wires, and one cathode strip. The other channels of cathode strips, which are not used for this simulation, are in reality readout by other amplifiers, but here they are simplified and connected to ground through a resistance of 100 MΩ.

A simulation model of two anode wires, two potential wires, and one cathode strip is shown in Fig. 3.37. A resistor with a resistance of 2 MΩ (reference R_HV) is attached to each anode wire in the side that applies high voltage, and a resistor with a resistance of 1 kΩ (Rdump) to suppress oscillation and a capacitor with a capacitance of 2 nF to make its voltage stable are added in the dumping side. Divided an anode wire in two, two resistances of 80 Ω (Rano) and two inductances of 0.3 μH (Lano) are put as an anode wire. For a potential wire, two resistances of

7 Ω (Rpo) and two inductances of 0.3 μH (Lpo) are put. There is stray capacitance of 2 pF from Eq. (2.11) between an anode wire and potential wire so that, divided the capacitance in three, three capacitances of 0.7 pF (Cwire) are drawn. As stray capacitance between some wires and one cathode strip, twelve of capacitance of 150 fF are input.

In the rightmost of Fig. 3.35, a model of version 1 amplifier is drawn. The zoom-in diagram of this part will be written in the section later. About the development of version 1 amplifier, please see [28].

3.2.4 Circuit Change and Result

Results of the simulation are shown in Figs. 3.38 and 3.39. The V(n003), V(n004), and V(N047, N048) are voltage at node 3, voltage at node 4, and voltage difference between nodes 47 and 48, that is, output voltage from the readout amplifier, respectively. In the simulation, we do not see oscillation from 10 μs to 20 μs when the detector is working, but from then on after the operation of the detector becomes off, oscillation is seen even though its period and amplitude are different from those in reality. In Fig. 3.38, the amplitude of the oscillation does not change so much, while in Fig. 3.39, we see that the amplitude is decreasing as the capacitance increases.

Six capacitors with a capacitance of 0.1 μF and a voltage proof of 2 kV (2220Y2-K00104KXTWS2 of Knowles Syfer, Digi-Key number 1608-1174-1-ND) are added to the original capacitor C2 of the real circuit in parallel, and they are covered with a heat-shrinkable tubing to protect electrically.

Figures 3.40 and 3.41 show the output waveforms before and after adding a capacitor of 0.6 μF in total, respectively. As we can see, the oscillation after the detector turned off is suppressed, but there is no change for the amplitude of oscillation generated when it is on.

3.3 Amplifier

To prevent reading amplifiers from being saturated by the oscillation of output waveform and from being dead, the gain or dynamic range of the amplifiers is modified. A photograph and circuit diagram of one-channel amplifier version 1 are shown in Figures 3.42 and 3.43, respectively. Amplifiers of sixteen channels are gathered up, and this is put in a shield case. Figure 3.44 shows a circuit diagram of the whole sixteen channels.

3.3.1 Development of Version 2 Amplifiers

A circuit model of reading amplifier version 1 in the circuit simulator LTspice is shown in Fig. 3.45. For a width of a Y-direction-readout cathode strip five times as large as a strip of X-readout, they pick up a lot of noises. Therefore, the gain of amplifiers for Y-direction readout was lowered. Figure 3.46 shows simulation of changing R10 to 2 kΩ, R11 to 1 kΩ, and R12 to 5.6 kΩ, and inputting the circuit model into the whole simulation model (Fig. 3.35). I(I1) is input current of 0.033 pC with a triangle waveform with a height of 3.3 μA and a bottom length of 20 ns. The charge is estimated by Eq. 2.23 for a minimum ionizing particle multiplied by one third which is a ratio of charge to be induced in one side of the cathode plane. As shown in Fig. 3.47, the pulse height is simulated to be approximately 50 mV.

The production of the reading amplifiers of version 2 was carried out at the beginning of 2017. Appendix summarizes parts lists, parts shops, and the cost for the daughter card of the reading amplifier version 2, and their mother board version 1.1.

After the circuit was actually modified, the output waveform was checked. Figures 3.48 and 3.49 show Y-direction-readout output waveform using amplifier version 1 and version 2, respectively. By making the gain of the reading amplifier smaller, the waveform saturation by the oscillation is reduced.

3.3.2 Development of Version 3 Amplifiers

For amplifier version 3, to prevent the amplifier from negative saturation, the dynamic range in the negative direction was increased. Figure 3.50 shows simulations of changing R10 to 5.1 kΩ and R12 to 30 kΩ, and of changing R10 to 2 kΩ and R12 to 32 kΩ. The original amplifier is version 1, and the gray lines mean the upper limit of FADC used for the experiment. The simulations show that the original negative limit of -150 mV increases to -300 mV and -400 mV, respectively.

Figure 3.51 is X-readout output waveform using amplifier version 1. First, two kinds of amplifier with different sets of values of R10 and R12 are produced as a trial. The original amplifier has a negative range of 75 ADC counts (-150 mV), and trial-produced amplifiers have a negative range of 100 ADC counts (-200 mV) (see Fig. 3.52) and 150 counts (-300 mV) (Fig. 3.53). The latter was chosen, and amplifiers version 3 were mass-produced at the beginning of 2018. The part lists and cost of the daughter cards of version 3 amplifier are summarized in the appendix. As of December, 2018, the daughter cards of the reading amplifier version 3 are replaced with those of version 1 in the mother boards, and are used for the preparation experiment.

3.4 Beam Test

In this section, we describe tests of the MWPCs using electron linear accelerator of the Institute for Integrated Radiation and Nuclear Science, Kyoto University in February, 2018 (Research Reactor Institute, Kyoto University at that time). The mean energy of electrons is 20 MeV, and it can be regarded as minimum ionizing particles. The repetition is 25 Hz in the same way as the DeeMe experiment. Figure 3.54 shows a photograph and schematic diagram of the 724-type MWPC and counters for calibration put in the target room of electron linear accelerator, and Fig. 3.55 illustrates a layout drawing of placement.

3.4.1 Hit Efficiency

Hit efficiency of the MWPC is measured by checking if the MWPC has a hit at the time when two counters put in front of and behind the MWPC have a coincidence hit by electron beam. Figure 3.56 shows the waveform of two photomultiplier tubes of counters (red and blue), template-waveform-subtracted waveform of the MWPC (black), and monitor-out of the HV switching module (light green). While the waveforms of two photomultipliers and monitor-out are taken by copper FADC with a sampling rate of 2 ns, the waveform of the MWPC is done by FADC with a sampling rate of 10 ns. The following is some details of analyzing the hit efficiency of the MWPC:

1. When the HV switching module supplies a high voltage, its monitor-out is about 200 mV. Looking at the timing when the monitor-out of the HV switching module falls from 200 mV to 0 V and the time when the MWPC waveform is saturated to the negative direction, we can match the time of the MWPC FADC and the copper FADC. The monitor-out (light green) of 10 counts means that the HV switching module supplies 0 V to the potential wires of the MWPC and the MWPC is working.
2. When the photomultiplier (drawn in red) has a signal less than a threshold of -25 counts and the other photomultiplier (drawn in blue) has the one less than -6 counts, we think there is a coincident hit in two counters.
3. We identify a MWPC channel and the time with the highest ADC count among the sampling points of plus and minus ten points (100 ns) from the time when

the two counters have a coincident hit. We consider that there is a hit of the MWPC if the hit meets the following two conditions: (1) Seven points (± three points from the peak are all larger than 1 count, (2) the sum of ADC counts in the direction of time (ten points before the peak and five points after the peak) is larger than the same ADC sum of the two adjacent strip channels. Figure 3.57 shows the number of hits versus time of two-counter coincidence and the MWPC. This represents the time structure as a function of time of electron beam of this electron linear accelerator.

4. Hit efficiency of the MWPC is calculated by the number of hits on the MWPC divided by the number of hits of two-counter coincidence.

Analyzed hit efficiency versus time of X-direction readout of the MWPC in the way above is shown in Fig. 3.58, and that of Y-direction readout is shown in Fig. 3.59, using the 724-type MWPC filled with gas mixture of argon (80%) isobutane (20%), 1540 V applied. The X-readout has a hit efficiency of approximately 98%, while the Y-readout has 60%. The efficiencies are improved from those when we use the MWPCs filled with agron (33.3%) ethane (66.6%) and amplifiers version 1 in June, 2017 (Figures 3.28 to 3.31). A simple method to improve the Y-readout hit efficiency is to change the width of the Y-direction cathode strips to the same width as the X-readout. Figures 3.60 and 3.61 show the hit efficiency of X-readout versus the number of hits on the MWPC and its enlarged graph. The less hits on the MWPC, the more entries there are. This is because the hit efficiency falls down due to pile up in the time that two counters have a lot of coincidence.

3.4.2 Position Resolution

We tried to analyze the position resolution of the tracking detectors from the experimental data using four MWPCs at J-PARC MLF D2 Area in June, 2017. The analysis result will be mentioned in Chapter 4.

3.4.3 Waveform Fluctuation after Many Particles Hitting

In the DeeMe experiment, 10^8 charged particles per pulse of prompt burst will hit the MWPCs before the analysis window. Figure 3.62 shows the output waveform when beam of 10^7 electrons per pulse from the electron linear accelerator enters the MWPC. We see spikes in the output waveforms during the time window when the MWPC is operational. They are randomly generated and it is difficult to distinguish them from incident electron signals. The cause is under investigation, but one possibility could be the electrons emerging from the cathode plane when ions reach and hit it.

3.5 Simulation of Mixing Freon Gas

To suppress the fluctuation of waveform in the section before, it was suggested to mix the gas of the compound including fluorine. Due to the electronegativity of the compound including fluorine, after having absorbed extra electrons generated from a large amount of prompt burst, that may make the MWPCs possible immediately to restore the operation for searching for μ-e conversion. This time, for $C_2H_2F_4$ and SF_6 usable in Japan, it was simulated how much fraction the gases absorb electrons which produced near the cathode plane, using Garfield++.

Figure 3.63 illustrates simulations of absorbing electrons during drifting. For the geometry, a voltage of 1500 V is applied to both anode and potential wires of the MWPC with a wire spacing of 0.7 mm, that is, the operation as a detector is on. Electrons are put in place that is near to one of the cathode planes, y=0.28 cm at random. In the case of argon (80%) isobutane (20%), electrons drift to the anode plane without being absorbed at all. Here if we mix $C_2H_2F_4$ (3%) or SF_6 (0.02%) to the gas mixture, some electrons are absorbed on the way of drifting to the anode plane (shown in blue markers).

Figure 3.64 shows the simulation result of where electrons put near the cathode plane are absorbed while drifting to the anode wires for mixing $C_2H_2F_4$ (3%) with argon (80%) isobutane (20%). While electrons of 3% are absorbed from y =0.28 cm to several hundred micrometers, 97% arrive at the anode wires. The number of electrons left without being absorbed N is expressed by

$$N = N_0 \exp(-ax) \tag{3.16}$$

where N_0 is the original number of electrons, a the attachment coefficient, and x the drift distance. For the attachment coefficient mixing $C_2H_2F_4$ (3%),

$$9700 = 10000 \times \exp(-a \times 0.28 \text{ cm}) \tag{3.17}$$

$$a = 1.1 \times 10^{-1} \text{ cm}^{-1}. \tag{3.18}$$

Similarly, the attachment coefficient $a = 5.0\ \mathrm{cm}^{-1}$ for mixing SF_6 (0.02%) into argon (80%) isobutane (20%). From this result, it is found that if we mix SF_6 about 0.06% into argon (80%) isobutane (20%) electrons of 99% generated by a large number of ions from prompt charged particles hitting the cathode walls are absorbed. In the simulation of mixing SF_6 of 0.05% (see Fig. 3.66), electrons of 98% are absorbed during drifting a length of approximately 3 mm.

Some ions of the prompt charged particles may hit the cathode walls after the operation of the MWPC starts. The attachment coefficient for mixing SF_6 (0.02%) is simulated to be $a = 1.4 \times 10^1\ \mathrm{cm}^{-1}$ when high voltage is applied to the anode wires and 0 V applied to the potential wires. In this case electrons of 98% will be absorbed while they drift.

Tables 3.9, 3.10, 3.11 and 3.12 summarize main parameters and gas gain (the number of electrons after being amplified from one electron accelerated near an anode wire), respectively. Actual experiment to mix compound including fluorine with mixture gas will be conducted to optimize the filling gas, balancing condition of the absorption of prompt charged particles and the gas gain or detect efficiency in the future.

Table 3.9: Argon (80%) isobutane (20%).

	Value
`Drift velocity along` E	2.08×10^{-2} cm/ns $\pm 0.089\%$
`Longitudinal diffusion`	1.00×10^{-2} cm$^{\frac{1}{2}}$ $\pm 7.7\%$
`Transverse diffusion`	1.14×10^{-2} cm$^{\frac{1}{2}}$ $\pm 10\%$
`Townsend coefficient (SST)`	1.97×10^{3} cm^{-1} $\pm 0.22\%$
`Attachment coefficient (SST)`	0 cm^{-1} $\pm 0\%$
`Eff. Townsend coefficient (TOF)`	1.98×10^{3} cm^{-1}

Table 3.10: Argon (80%) isobutane (20%) sulfur hexafluoride (0.02%).

	Value
`Drift velocity along` E	2.08×10^{-2} cm/ns $\pm 0.089\%$
`Longitudinal diffusion`	0.97×10^{-2} cm$^{\frac{1}{2}}$ $\pm 9.3\%$
`Transverse diffusion`	1.14×10^{-2} cm$^{\frac{1}{2}}$ $\pm 9.6\%$
`Townsend coefficient (SST)`	1.98×10^{3} cm^{-1} $\pm 0.23\%$
`Attachment coefficient (SST)`	1.44×10^{-1} cm^{-1} $\pm 7.8\%$
`Eff. Townsend coefficient (TOF)`	1.98×10^{3} cm^{-1}

Table 3.11: Argon (77.6%) isobutane (19.4%) 1, 1, 1, 2-tetrafluoroethane (3%)

	Value
`Drift velocity along` E	2.08×10^{-2} cm/ns $\pm 0.054\%$
`Longitudinal diffusion`	0.98×10^{-2} cm$^{\frac{1}{2}}$ $\pm 3.8\%$
`Transverse diffusion`	1.12×10^{-2} cm$^{\frac{1}{2}}$ $\pm 9.9\%$
`Townsend coefficient (SST)`	1.94×10^{3} cm^{-1} $\pm 0.33\%$
`Attachment coefficient (SST)`	1.03×10^{-1} cm^{-1} $\pm 29\%$
`Eff. Townsend coefficient (TOF)`	1.95×10^{3} cm^{-1}

Table 3.12: Comparison of the gas gain for mixing some kinds of compound including fluorine.

Gas mixture	Gas gain
Argon (80%) isobutane (20%)	$(3.273\pm0.087)\times10^4$
+ $C_2H_2F_4$ (3%)	$(2.656\pm0.072)\times10^4$
+ SF_6 (0.02%)	$(3.235\pm0.088)\times10^4$

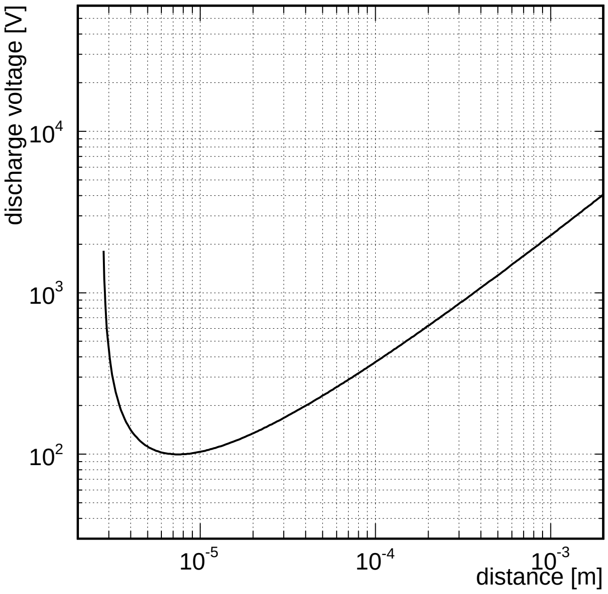

Figure 3.1: Paschen's law. Discharge voltage [V] as a function of distance for argon at 1 atmosphere.

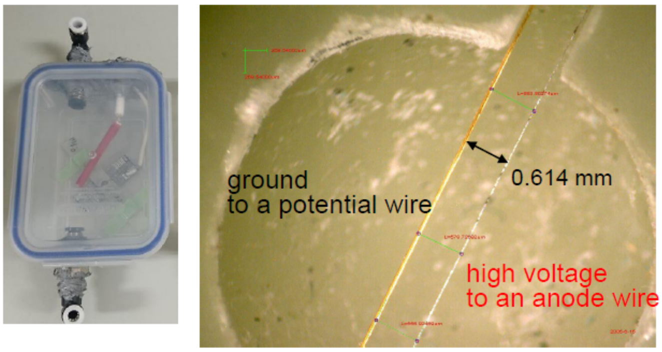

Figure 3.2: Photographs of a small chamber for discharge experiment (left) and tighten-up wires (right).

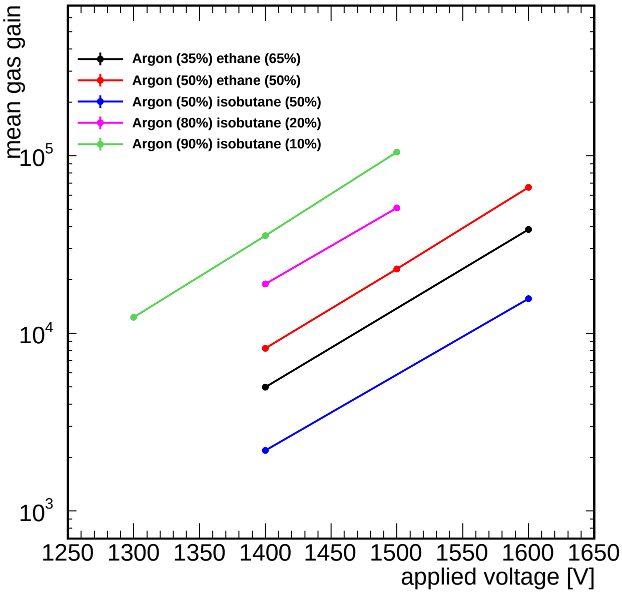

Figure 3.3: Simulated mean gas gain as a function of applied voltage for a wire spacing of 0.7 mm.

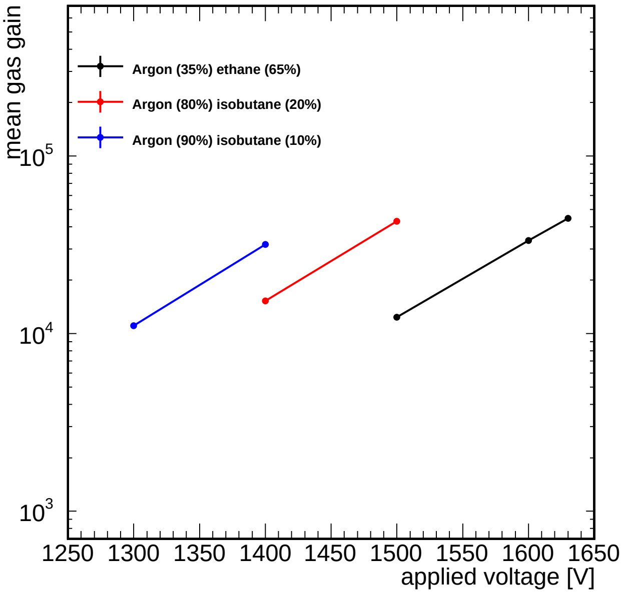

Figure 3.4: Simulated mean gas gain as a function of applied voltage for a wire spacing of 0.75 mm.

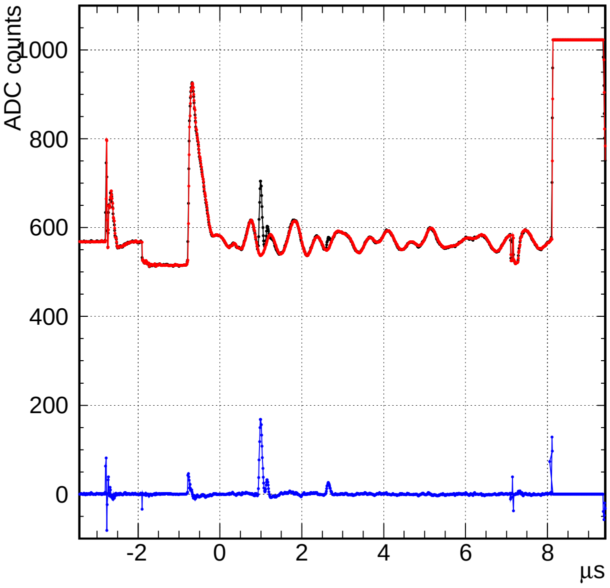

Figure 3.5: An output waveform of one trigger (black), waveform created from the most frequent ADC count values at each sampling point of waveforms (red), and subtracted waveform (blue).

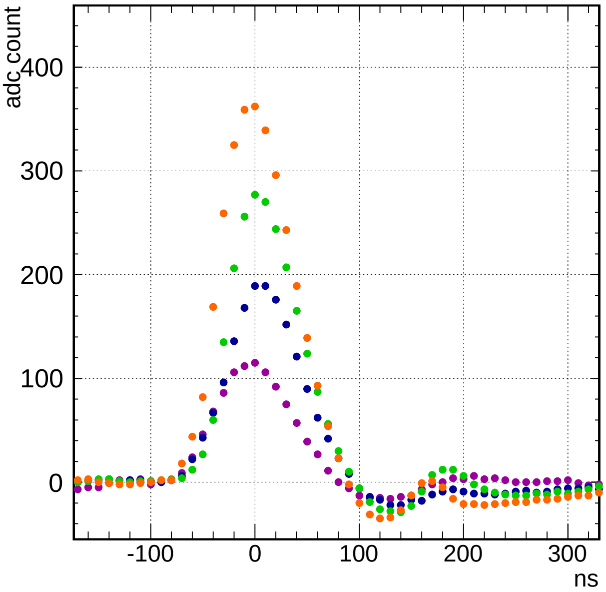

Figure 3.6: Signals of various pulse height sampled in 10 ns.

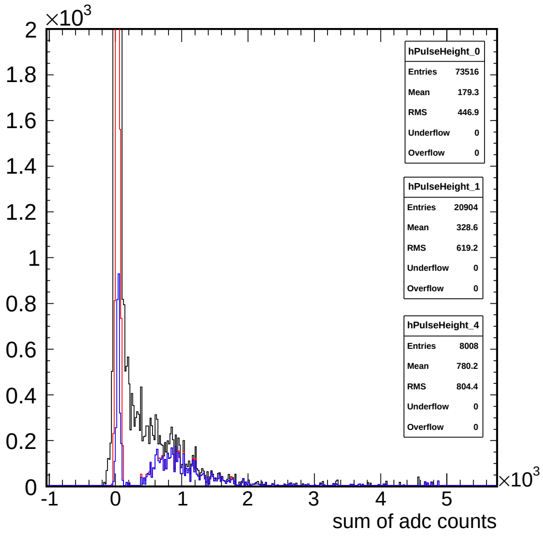

Figure 3.7: Histogram of the sum of ADC counts in time on one cathode strip after finding peak (black) and histograms with condition that the sum is larger than those of the two adjacent cathode strips (red), or in addition, with condition that the sums are larger than those of the furthermore next two cathode strips (blue).

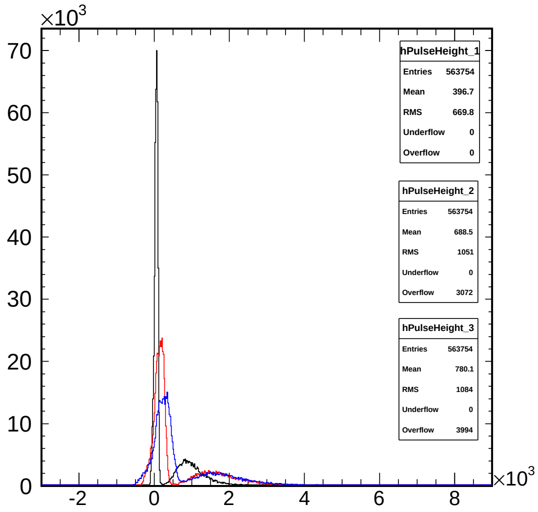

Figure 3.8: Histograms of the sum of ADC counts in the direction of time for one cathode strip (black), added over three cathode strips (red), and five cathode strips (blue) when electron beam enters the MWPC filled with argon (80%) isobutane (20%), and 1510 V applied with a wire spacing of 0.75 mm between an anode wire and a potential wire.

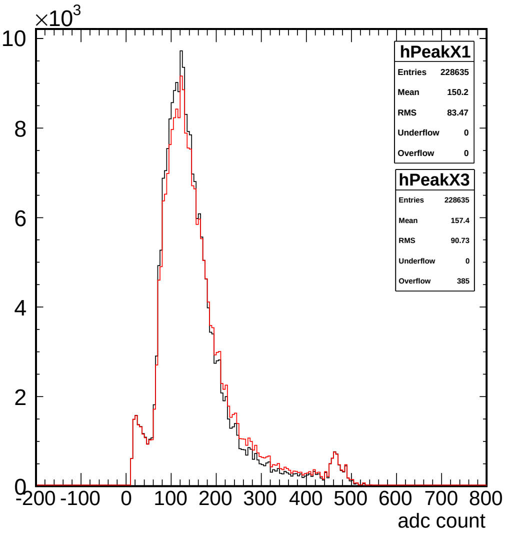

Figure 3.9: Histograms of the highest ADC count of one cathode strip (black) and three strips (red) of signals defined by the sum of ADC counts of three cathode strips in Fig. 3.8 being larger than 500 counts.

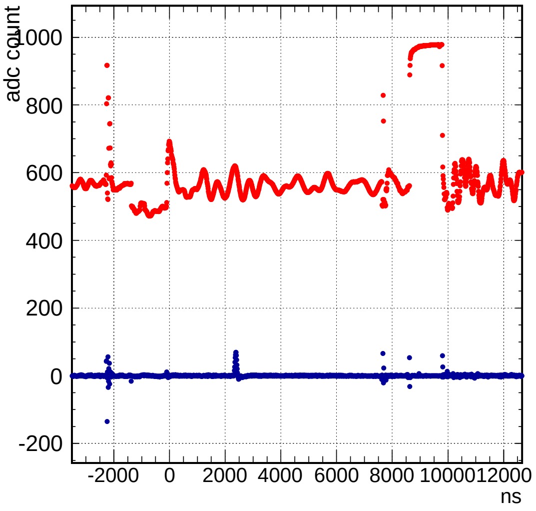

Figure 3.10: Waveform of one cathode strip for the Y-axis direction readout.

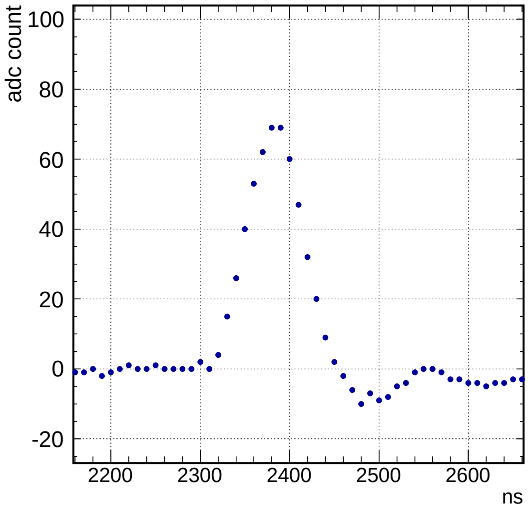

Figure 3.11: Signal on the Y-axis direction readout.

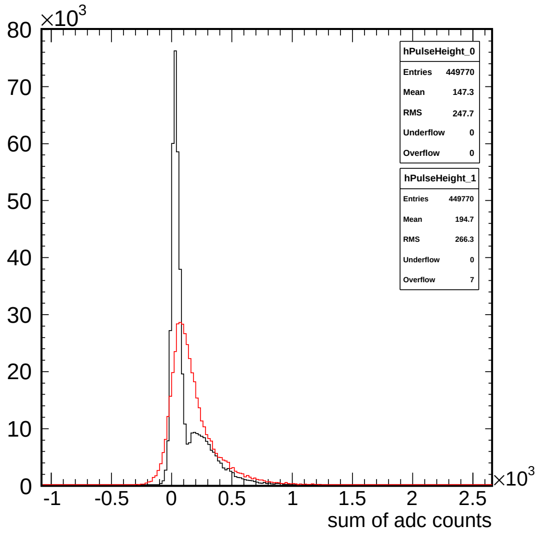

Figure 3.12: Histograms of the sums in the direction of time of ADC counts of Y-readout one channel (black) and three channels (red).

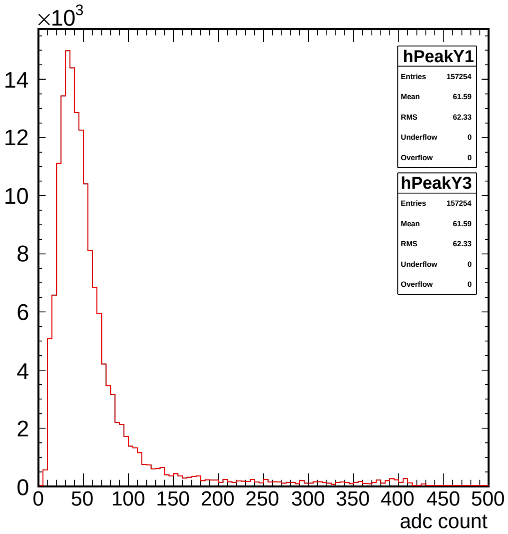

Figure 3.13: Histogramd of the highest ADC counts of one cathode strip (black) and three strips (red) of signals defined by the sum of ADC counts being larger than 100 counts in Fig. 3.12.

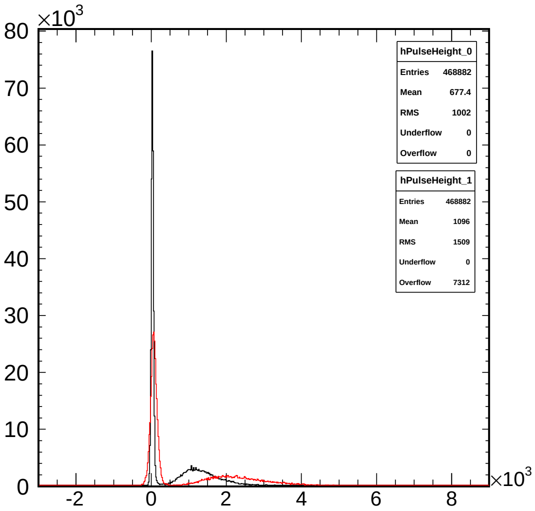

Figure 3.14: Histograms of the sum of ADC counts of X-readout for one cathode strip (black) and three cathode strips (red) of the MWPC with a wire spacing 0.75 mm filled with gas mixture of argon (80%) isobutane (20%) 1540 V applied.

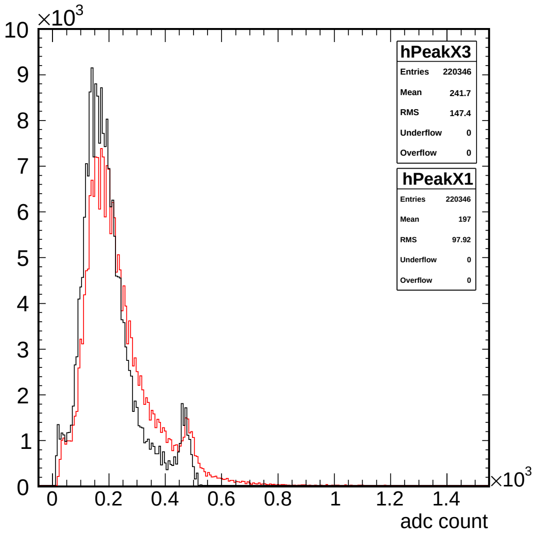

Figure 3.15: Histogram of the highest ADC counts of signals defined by the sum of ADC counts of three cathode strips in Fig. 3.14 being larger than 500 counts.

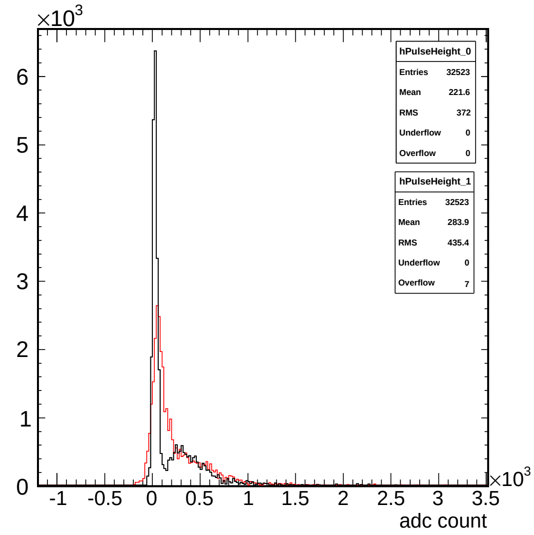

Figure 3.16: Histograms of the sum of ADC counts of Y-readout for one cathode strip (black) and three cathode strips (red) of the MWPC with a wire spacing 0.75 mm filled with gas mixture of argon (80%) isobutane (20%) 1540 V applied.

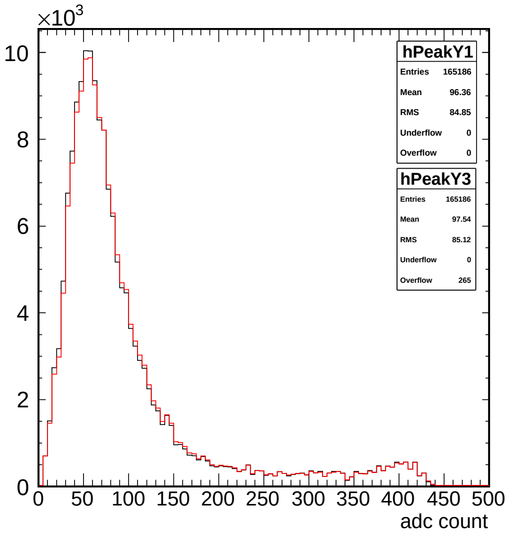

Figure 3.17: Histogram of the highest ADC counts of signals defined by the sum of ADC counts of three cathode strips in Fig. 3.16 being larger than 100 counts.

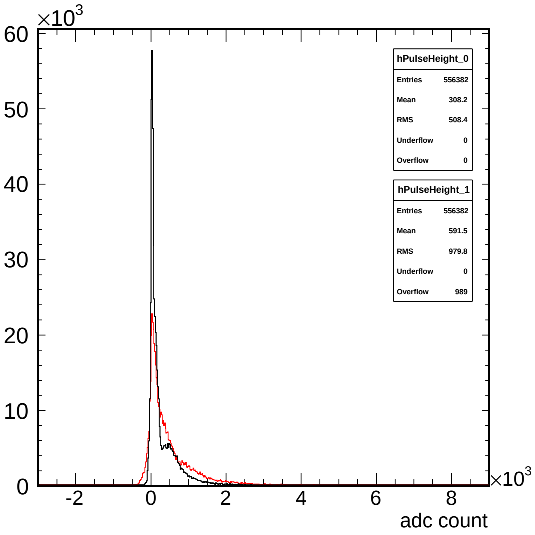

Figure 3.18: Histograms of the sum of ADC counts of X-readout for one cathode strip (black) and three cathode strips (red) of the MWPC with a wire spacing 0.7 mm filled with gas mixture of argon (33.3%) ethane (66.6%) 1650 V applied.

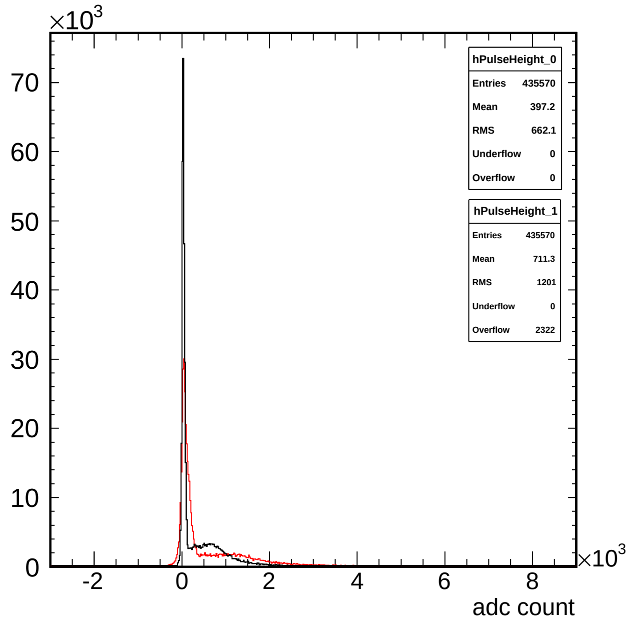

Figure 3.19: Histograms of the sum of ADC counts of X-readout one cathode strip (black) and three cathode strips (red) of the MWPC with a wire spacing 0.7 mm filled with gas mixture of argon (33.3%) ethane (66.6%) 1700 V applied.

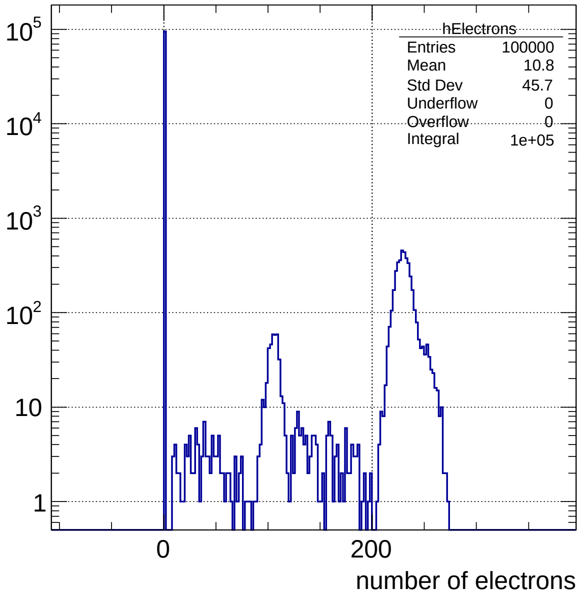

Figure 3.20: The number of electrons created when X-rays are incident on the active area of the DeeMe MWPC, simulated using Garfield++.

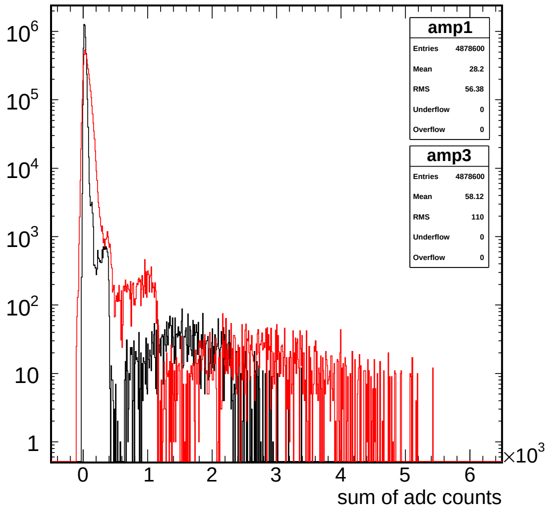

Figure 3.21: Histograms of the sum of ADC counts in the direction of time of one strip (black) and three strips (red) for data of the 724-type MWPC X-direction readout filled with gas mixture of argon (80%) isobutane (20%) and 1510 V applied using ^{55}Fe source.

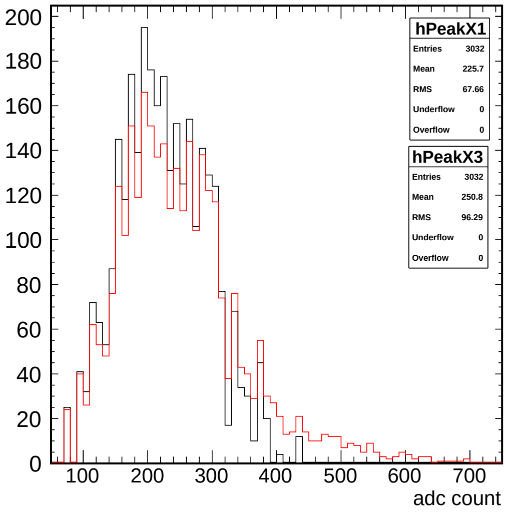

Figure 3.22: Histograms of the highest ADC count(s) of one cathode strip (black) and three cathode strips (red) for the sum of ADC counts larger than 600 in Fig. 3.21.

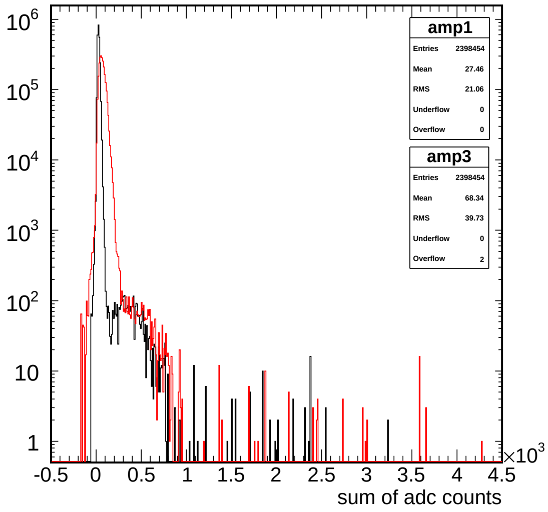

Figure 3.23: Histograms of the sum of ADC counts in the direction of time of one strip (black) and three strips (red) for data of the 724-type MWPC Y-direction readout filled with gas mixture of argon (80%) isobutane (20%) and 1510 V applied using ^{55}Fe source.

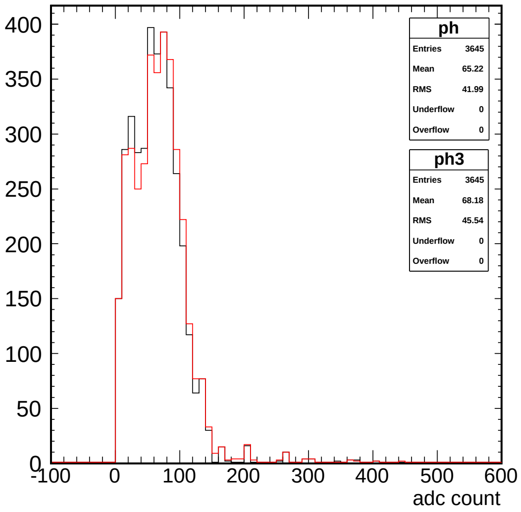

Figure 3.24: Histograms of the highest ADC count(s) of one cathode strip (black) and three cathode strips (red) of the sum of ADC counts larger than 100 counts in Fig. 3.21.

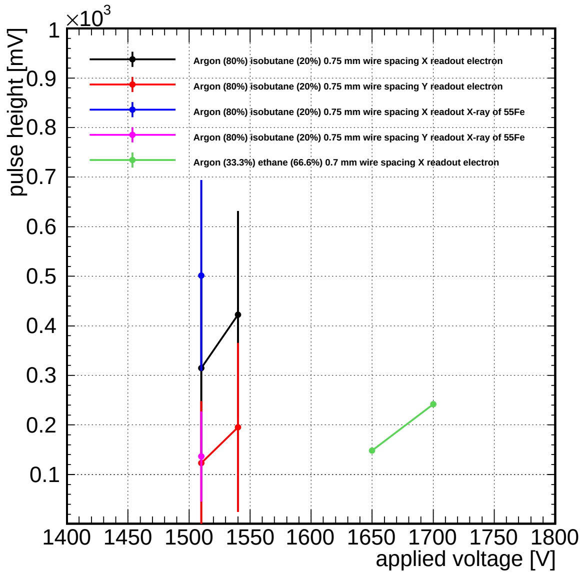

Figure 3.25: Summary of the analysis result of the sum of the highest ADC counts of three cathode strips for various gas mixture with electron beam and X-rays of ^{55}Fe versus applied voltage.

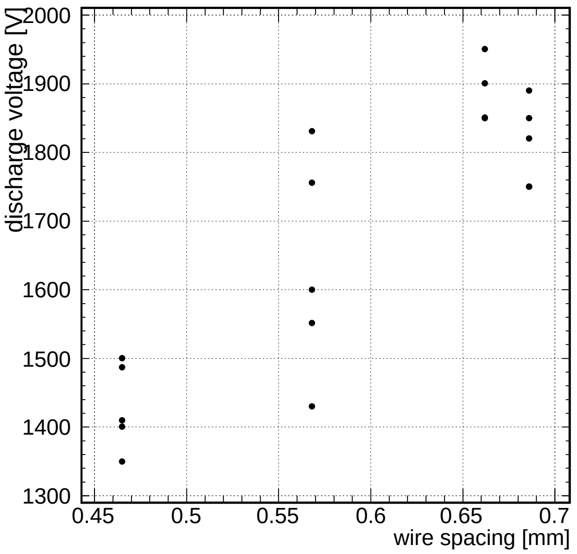

Figure 3.26: Results of discharge voltage as a function of distance between wires for argon (50%) ethane (50%) at 1 atmosphere [32].

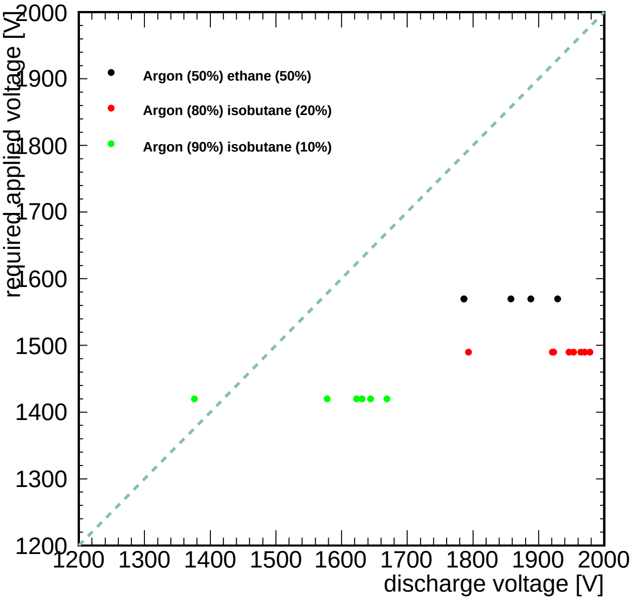

Figure 3.27: Required voltage to get a gas gain of 4.6×10^4 in the vertical axis versus the electric discharge voltage calculated for a wire spacing of 0.7 mm in the horizontal axis.

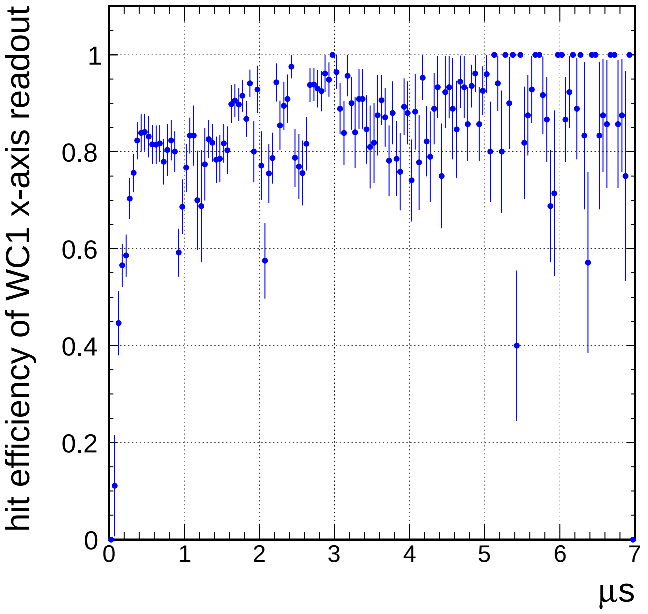

Figure 3.28: Hit efficiency as a function of time of the second MWPC X-readout from upstream at J-PARC MLF D2 Area in June, 2017.

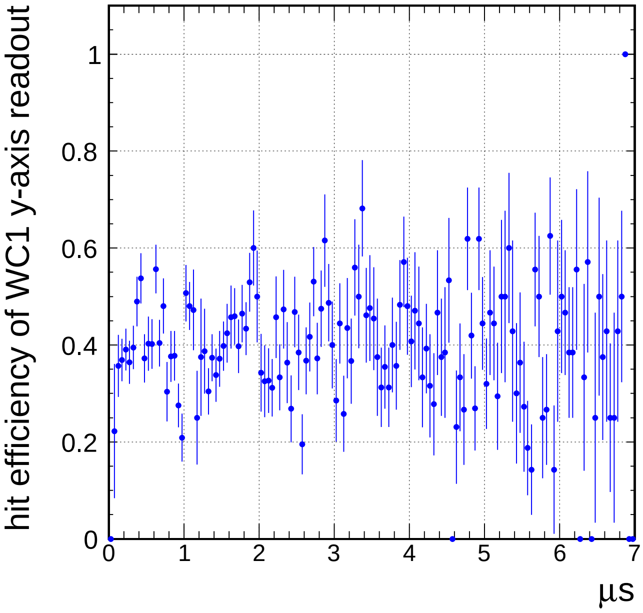

Figure 3.29: Hit efficiency as a function of time of the second MWPC Y-readout from upstream at J-PARC MLF D2 Area in June, 2017.

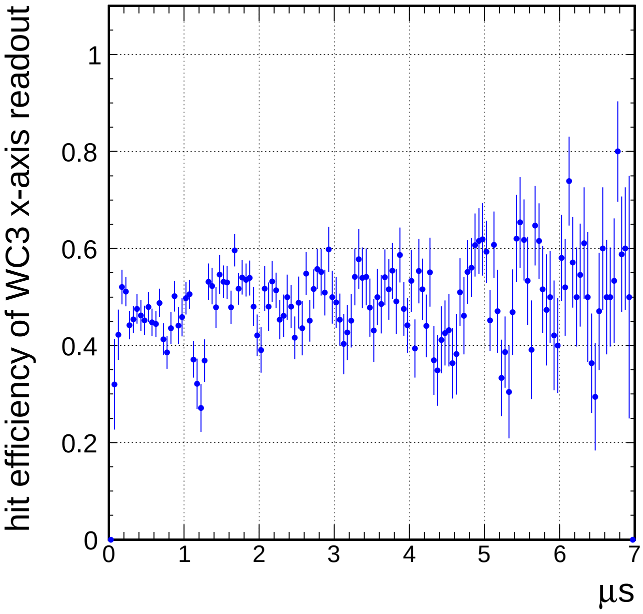

Figure 3.30: Hit efficiency as a function of time of the fourth MWPC X-readout from upstream at J-PARC MLF D2 Area in June, 2017.

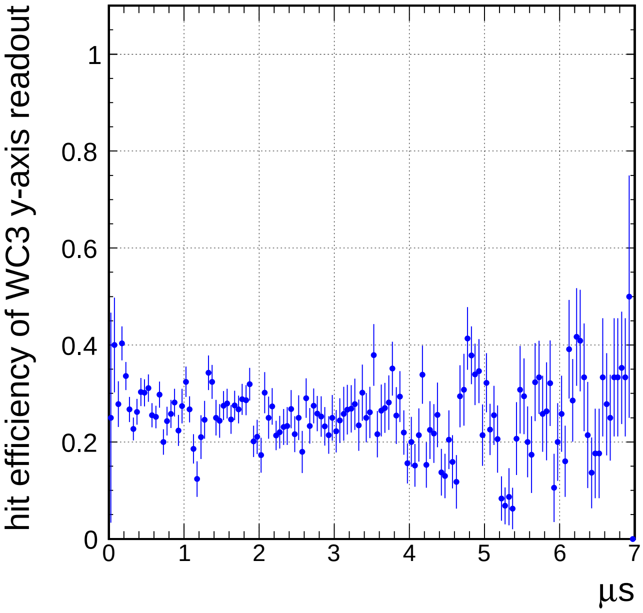

Figure 3.31: Hit efficiency as a function of time of the fourth MWPC Y-readout from upstream at J-PARC MLF D2 Area in June, 2017.

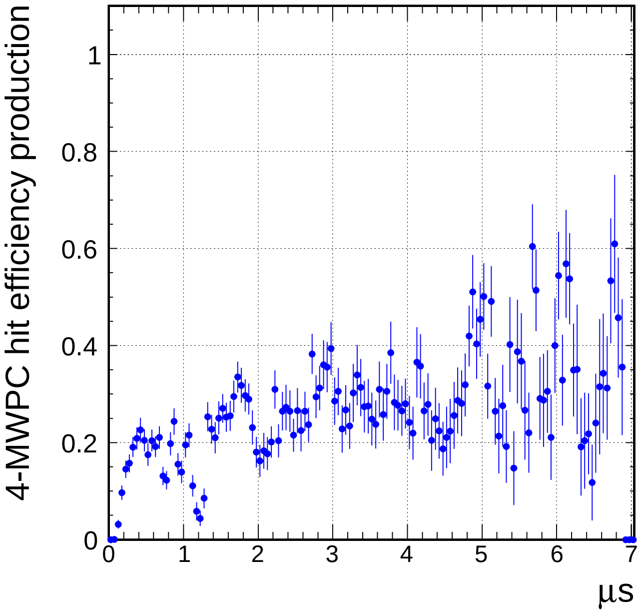

Figure 3.32: Production of hit efficiency of four MWPCs X-readout.

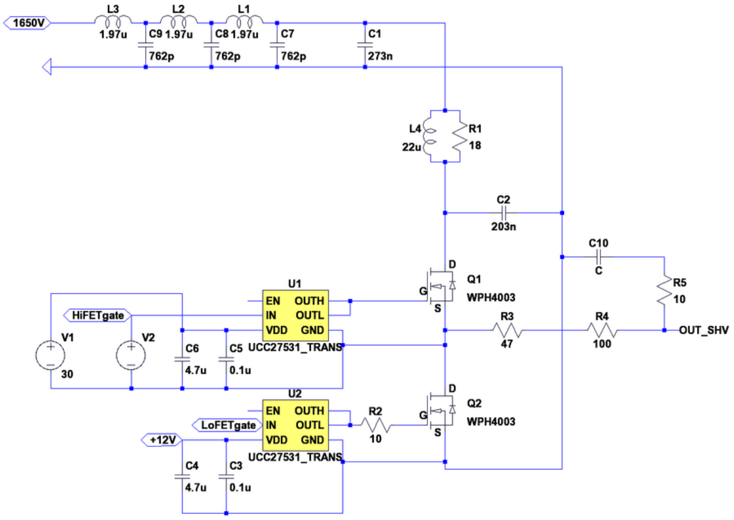

Figure 3.33: Simplified circuit diagram in the HV switching module.

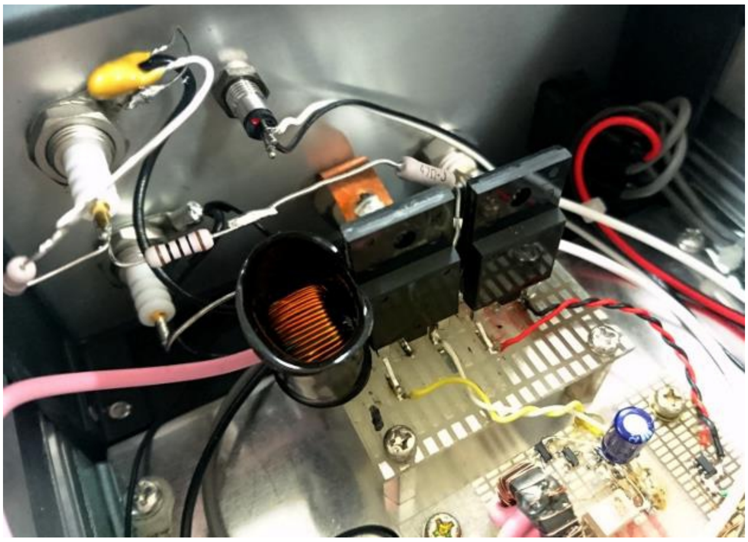

Figure 3.34: Photograph of a circuit made in HV switching module.

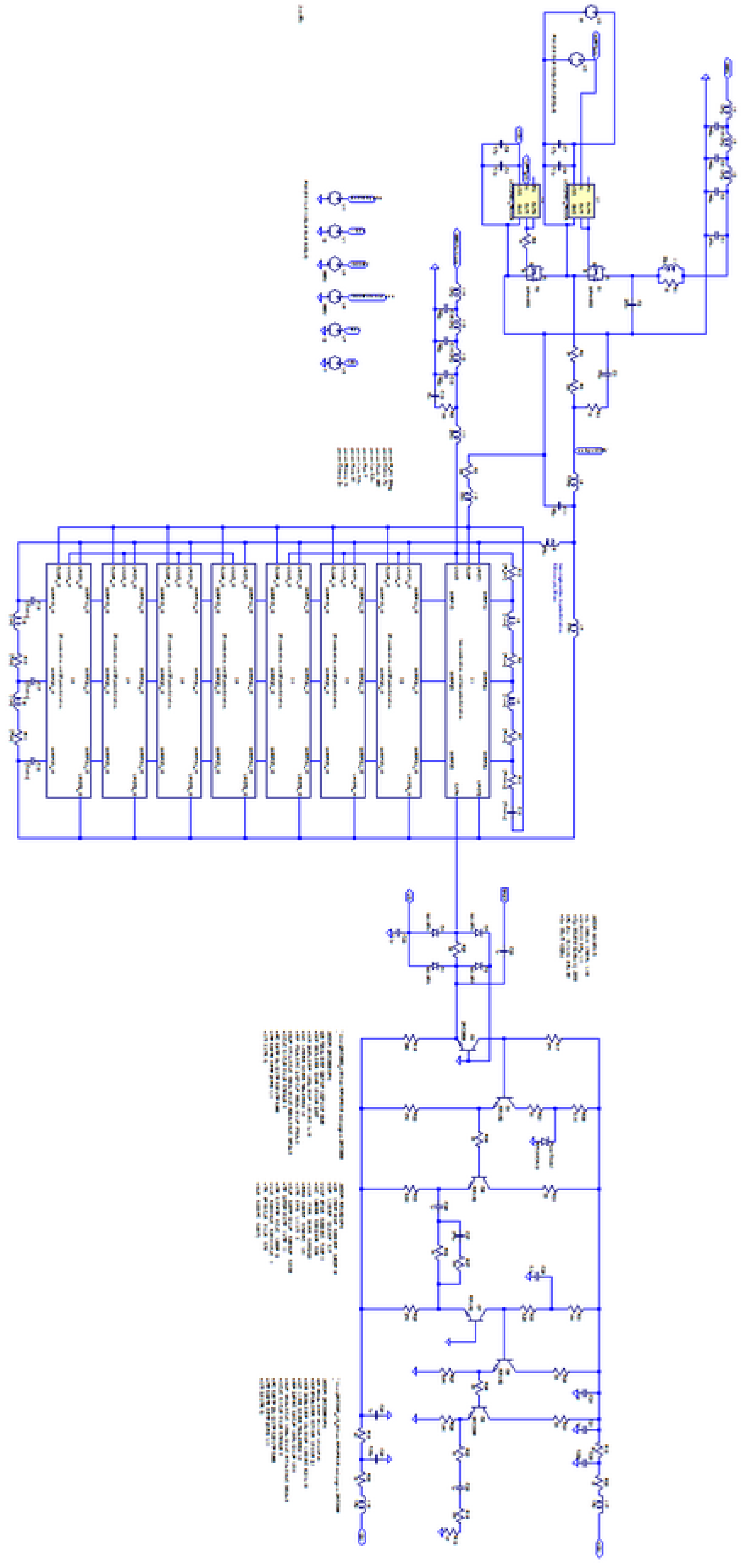

Figure 3.35: Whole simulation model of a HV-switching circuit, an MWPC, and a readout amplifier using a circuit simulator LTspice [37].

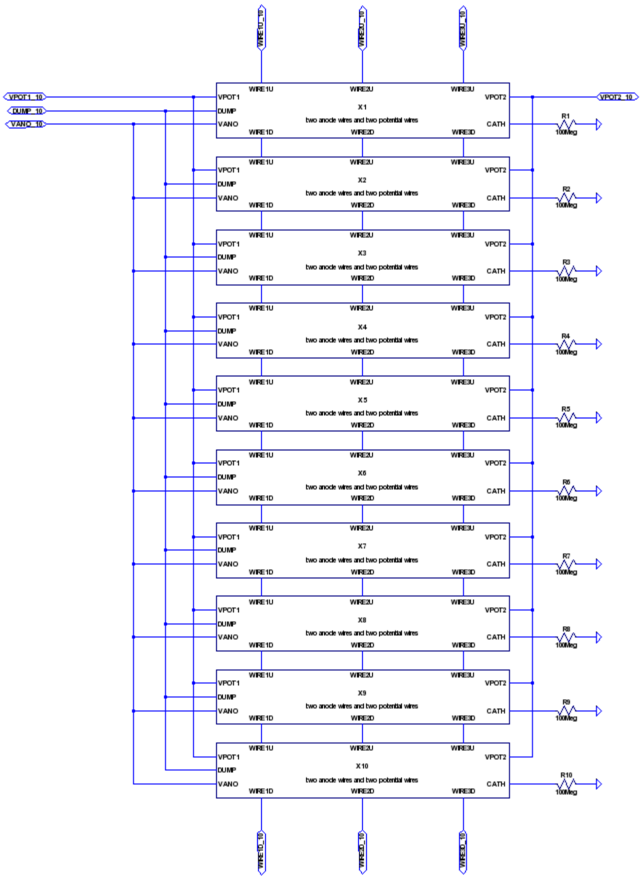

Figure 3.36: Sub-circuit model of 20 anode wires, 20 potential wires, and cathode strips.

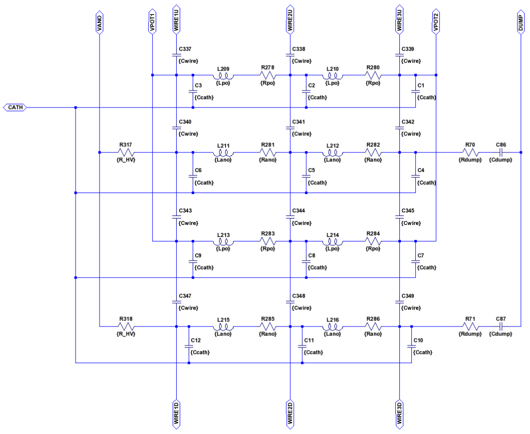

Figure 3.37: Simulation model of two anode wires, two potential wires, and one cathode strip.

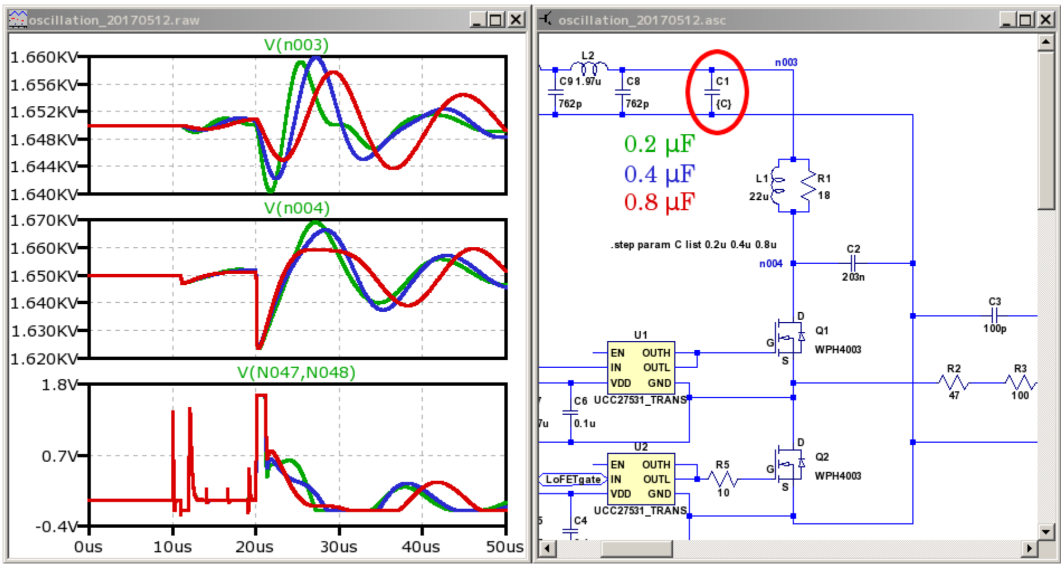

Figure 3.38: Simulation that the original value of 273 nF of capacitor C1 is changed to 0.2 μF, 0.4 μF, and 0.8 μF.

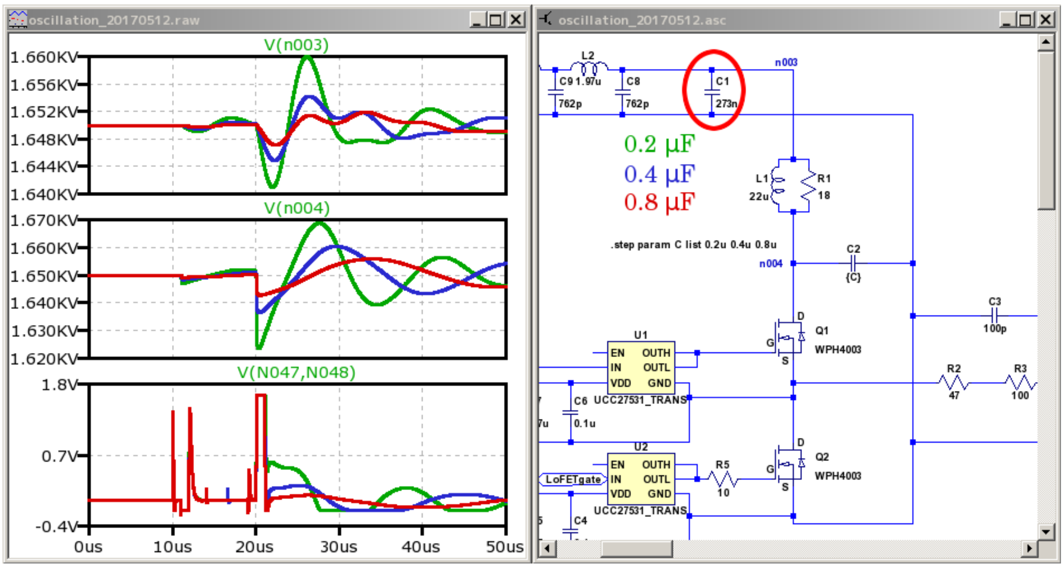

Figure 3.39: Simulation that the original value of 203 nF of capacitor C2 is changed to 0.2 μF, 0.4 μF, and 0.8 μF.

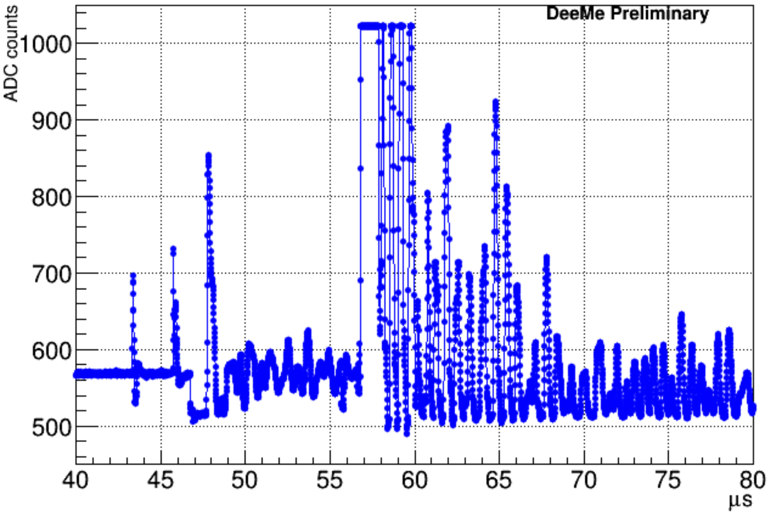

Figure 3.40: Output waveform before adding a capacitor of 0.6 μF in total to the original capacitor C2.

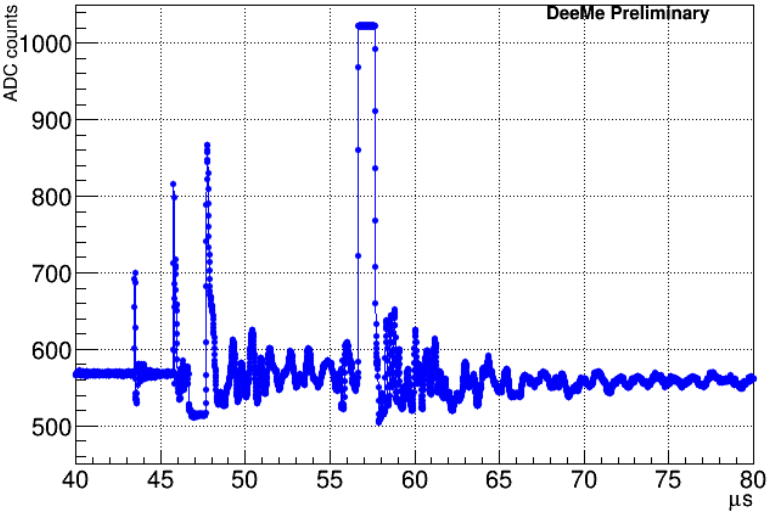

Figure 3.41: Output waveform after adding a capacitor of 0.6 μF in total to the original capacitor C2.

Figure 3.42: Photograph of one-channel amplifier version 1.

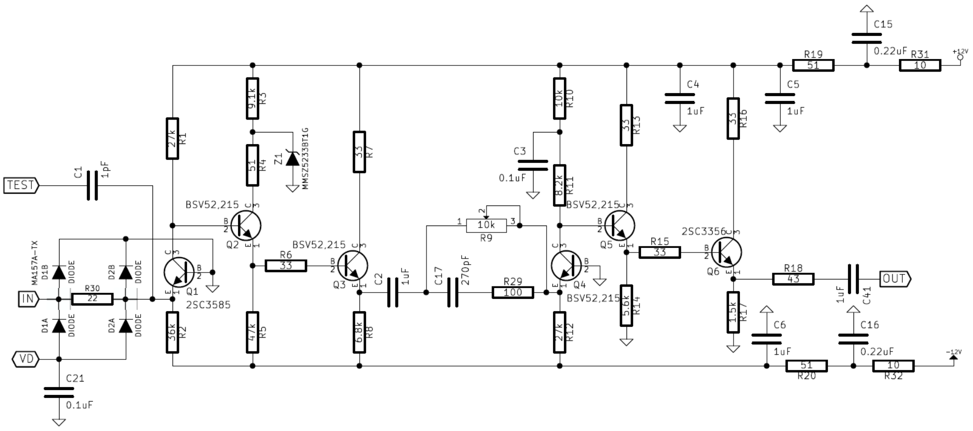

Figure 3.43: Circuit diagram of one-channel amplifier version 1.

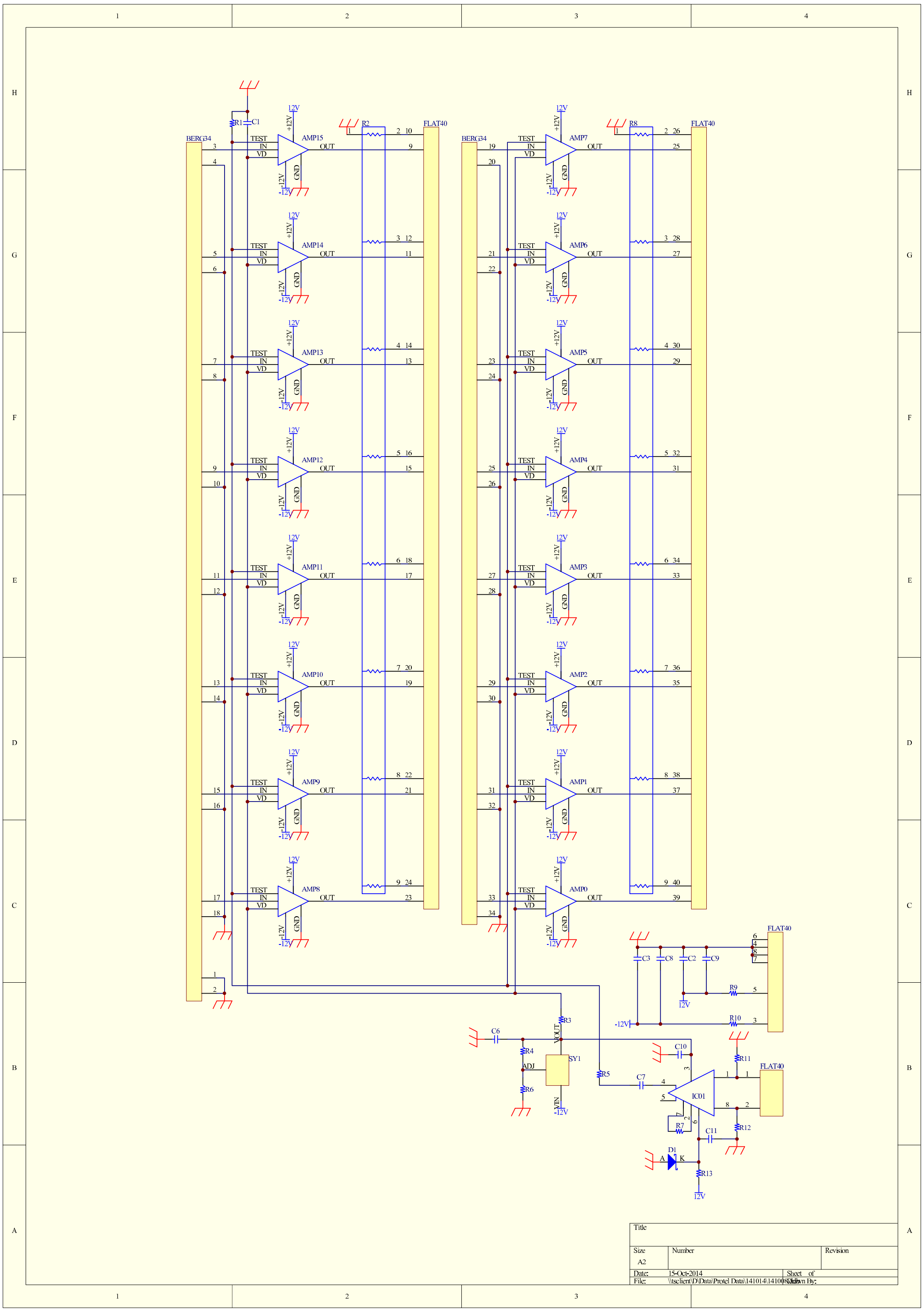

Figure 3.44: Circuit diagram of the whole sixteen-channel amplifiers.

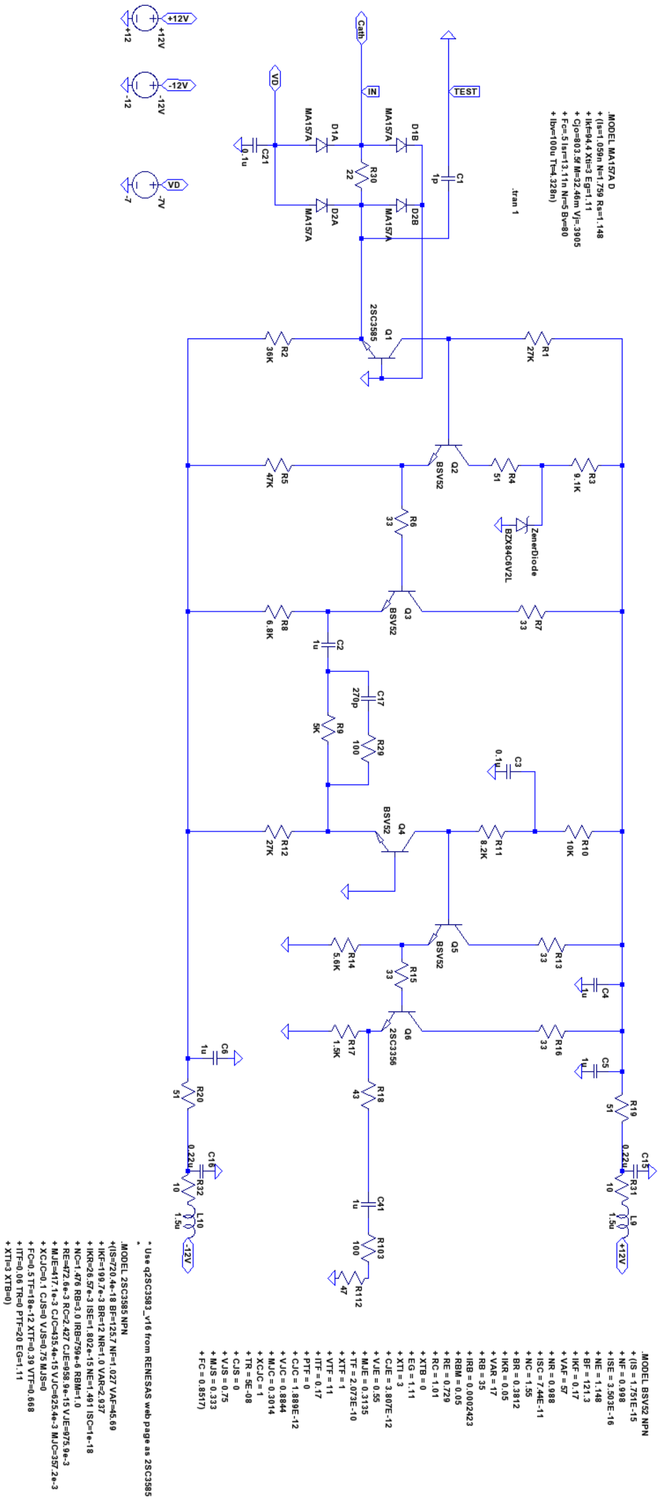

```
.MODEL MA157A D
+ (Is=1.059n N=1.759 Rs=1.148
+ Ikf=94.4 Xti=3 Eg=1.11
+ Cjo=803.5f M=32.46m Vj=.3905
+ Fc=.5 Isr=13.11n Nr=5 Bv=80
+ Ibv=100u Tt=4.328n)
```

```
.tran 1
```

```
.MODEL BSV52 NPN
+ (IS = 1.751E-15
+ NF = 0.998
+ ISE = 3.503E-16
+ NE = 1.148
+ BF = 121.3
+ IKF = 0.17
+ VAF = 57
+ NR = 0.988
+ ISC = 7.44E-11
+ NC = 1.55
+ BR = 0.3812
+ IKR = 0.05
+ VAR = 17
+ RB = 35
+ IRB = 0.0002423
+ RBM = 0.05
+ RE = 0.729
+ RC = 1.01
+ XTB = 0
+ EG = 1.11
+ XTI = 3
+ CJE = 3.807E-12
+ VJE = 0.55
+ MJE = 0.3135
+ TF = 2.073E-10
+ XTF = 1
+ VTF = 11
+ ITF = 0.17
+ PTF = 0
+ CJC = 1.889E-12
+ VJC = 0.8844
+ MJC = 0.3014
+ XCJC = 1
+ TR = 5E-08
+ CJS = 0
+ VJS = 0.75
+ MJS = 0.333
+ FC = 0.8517)
```

```
* Use q2SC3583_v16 from RENESAS web page as 2SC3585
*
.MODEL 2SC3585 NPN
+(IS=720.4e-18 BF=125.7 NF=1.027 VAF=45.69
+ IKF=199.7e-3 BR=12 NR=1.0 VAR=2.937
+ IKR=26.57e-3 ISE=1.802e-15 NE=1.491 ISC=1e-18
+ NC=1.476 RB=3.0 IRB=759e-6 RBM=1.0
+ RE=472.6e-3 RC=2.427 CJE=958.9e-15 VJE=975.9e-3
+ MJE=417.1e-3 CJC=435.4e-15 VJC=625.4e-3 MJC=357.2e-3
+ XCJC=0.1 CJS=0 VJS=0.75 MJS=0
+ FC=0.5 TF=18e-12 XTF=0.39 VTF=0.668
+ ITF=0.06 TR=0 PTF=20 EG=1.11
+ XTI=3 XTB=0)
```

Figure 3.45: Circuit model of reading amplifier version 1 in the circuit simulator LTspice.

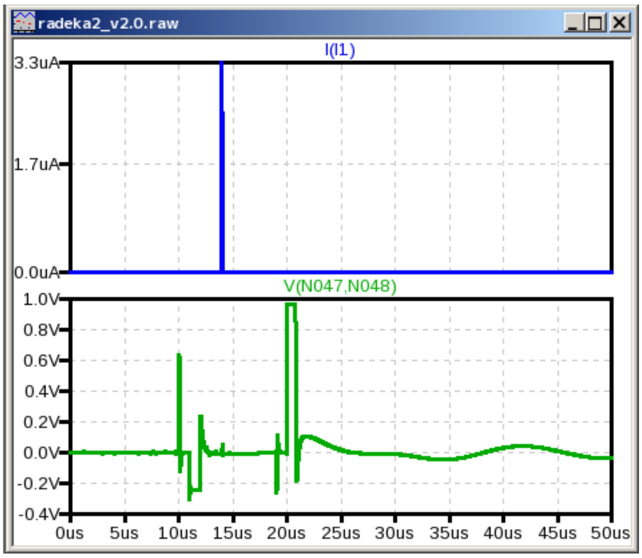

Figure 3.46: Simulation result of changing R10 to 2 kΩ, R11 to 1 kΩ, and R12 to 5.6 kΩ in the model of Fig. 3.45, and inputting the circuit model into the whole simulation model (Fig. 3.35).

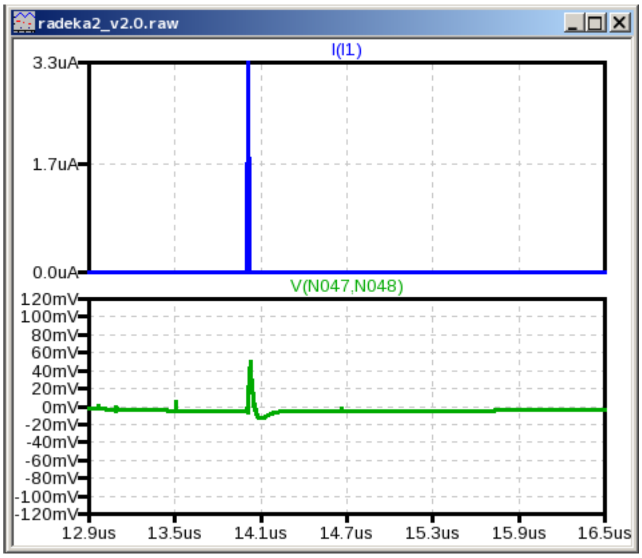

Figure 3.47: Simulation result (zoomed in) of changing R10 to 2 kΩ, R11 to 1 kΩ, and R12 to 5.6 kΩ in the model of Fig. 3.45, and inputting the circuit model into the whole simulation model (Fig. 3.35).

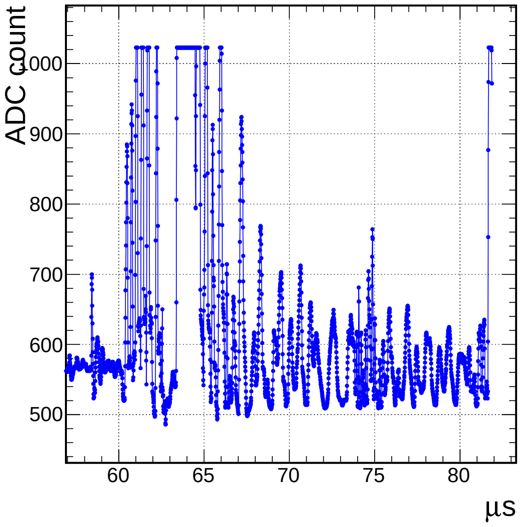

Figure 3.48: Y-direction-readout output waveform using amplifier version 1.

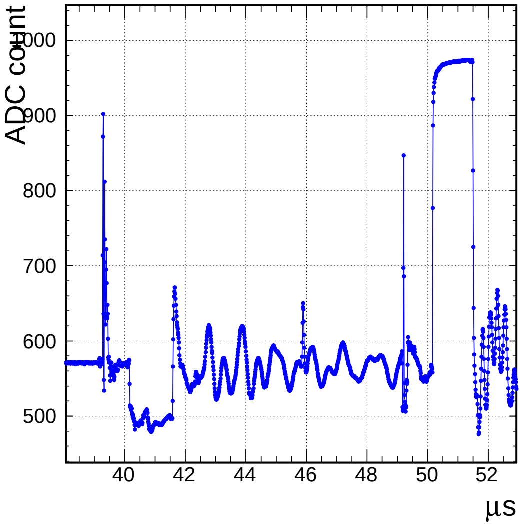

Figure 3.49: Y-direction-readout output waveform using amplifier version 2.

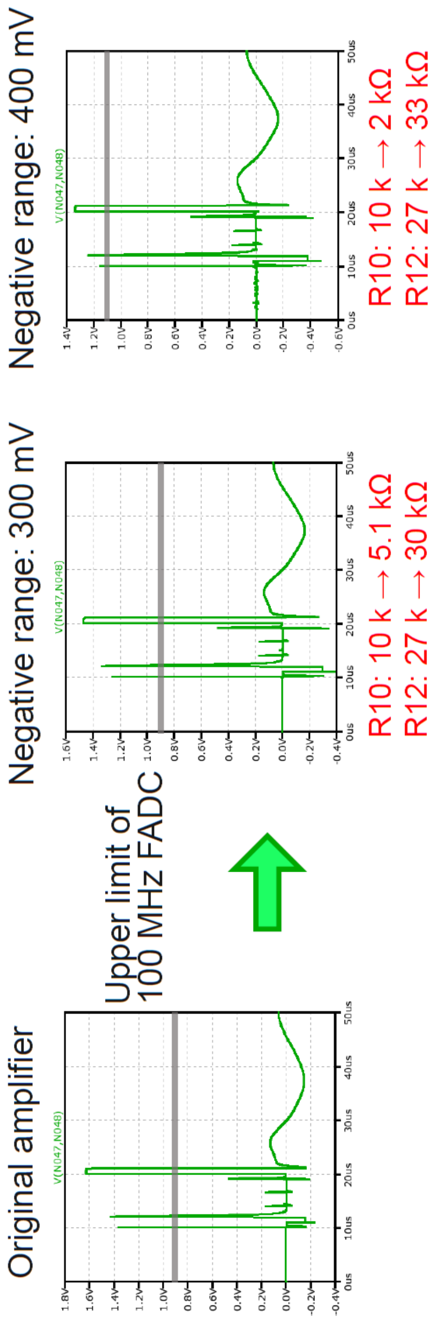
Original amplifier

Negative range: 300 mV

Negative range: 400 mV

Figure 3.50: Simulations of changing R10 to 5.1 kΩ and R12 to 30 kΩ, and of changing R10 to 2 kΩ and R12 to 32 kΩ. The original amplifier is version 1, and the gray lines mean the upper limit of FADC used for the experiment.

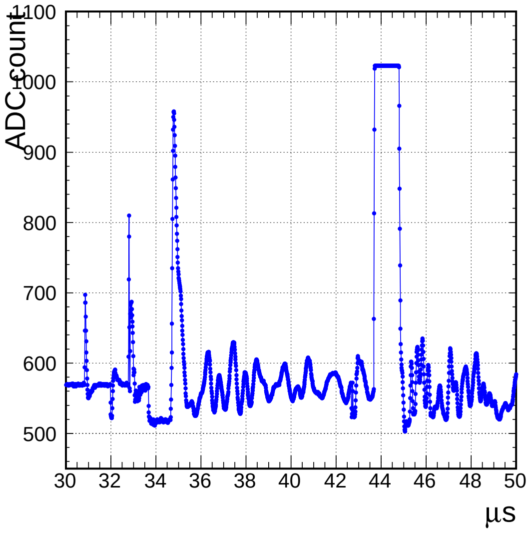

Figure 3.51: X-direction-readout output waveform using amplifier version 1.

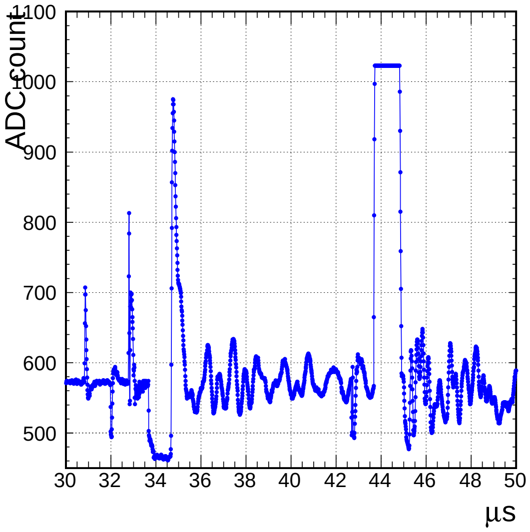

Figure 3.52: X-readout waveform of trial-produced amplifiers having a negative range of 100 ADC counts (-200 mV).

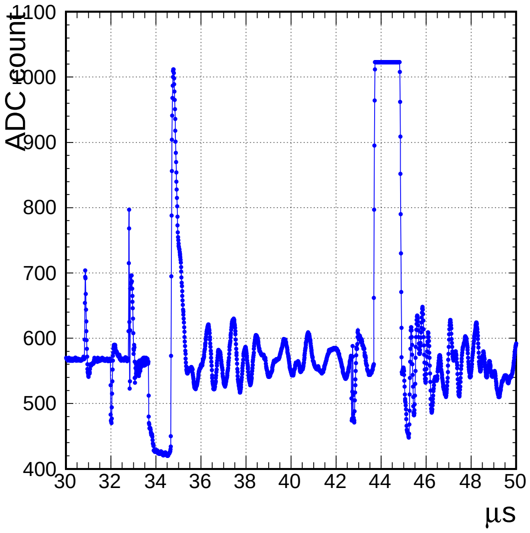

Figure 3.53: X-readout waveform of trial-produced amplifiers having a negative range of 150 ADC counts (-300 mV).

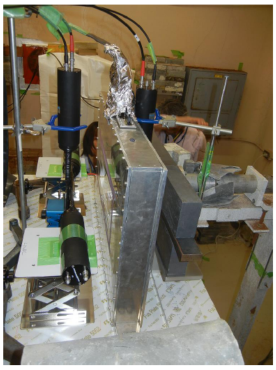

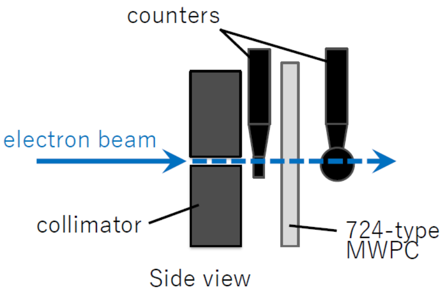

Figure 3.54: Photograph and schematic diagram of the 724-type MWPC and counters for calibration put in the target room of electron linear accelerator.

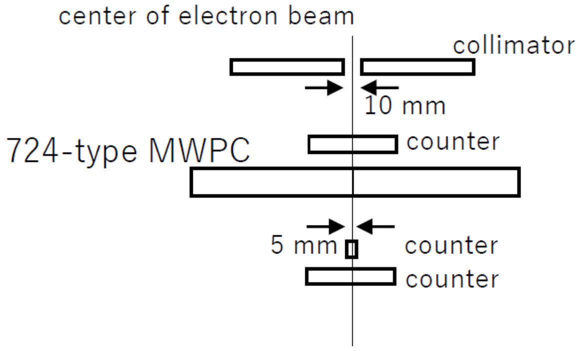

Figure 3.55: Layout drawing of placement in the target room in the experiment in February, 2018. The height of the beam is 230 mm from the edge under the MWPC.

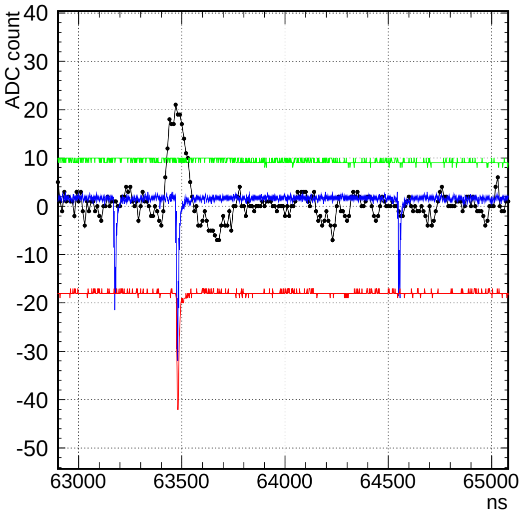

Figure 3.56: Waveform of two photomultiplier tubes of counters (red and blue), template-waveform-subtracted waveform of the MWPC (black), and monitor-out of the HV switching module (light green).

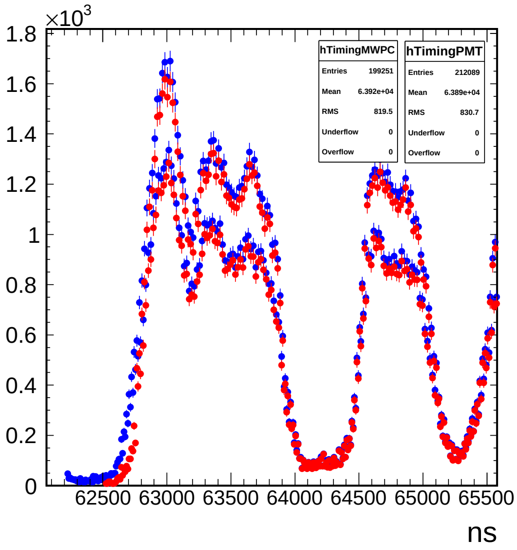

Figure 3.57: Number of hits versus time of two-counter coincidence and the MWPC.

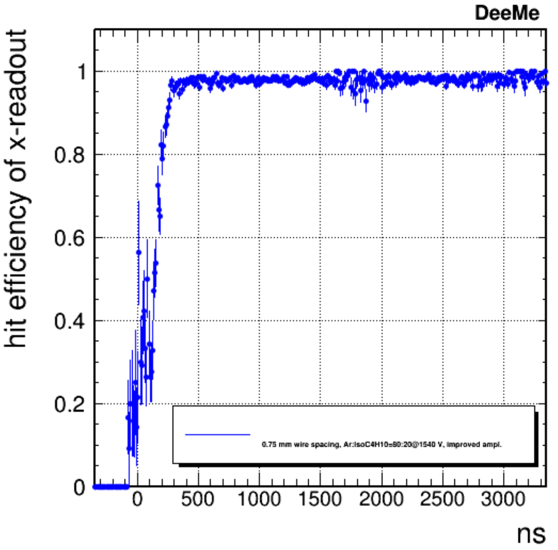

Figure 3.58: Hit efficiency versus time of X-direction readout of the 724-type MWPC filled with gas mixture of argon (80%) isobutane (20%), 1540 V applied.

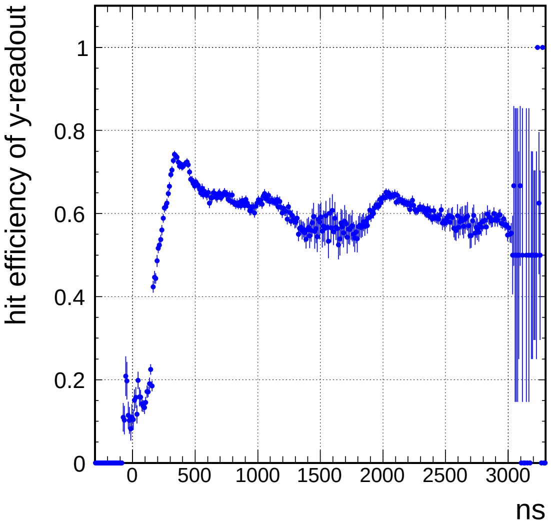

Figure 3.59: Hit efficiency versus time of Y-direction readout of the 724-type MWPC filled with gas mixture of argon (80%) isobutane (20%), 1540 V applied.

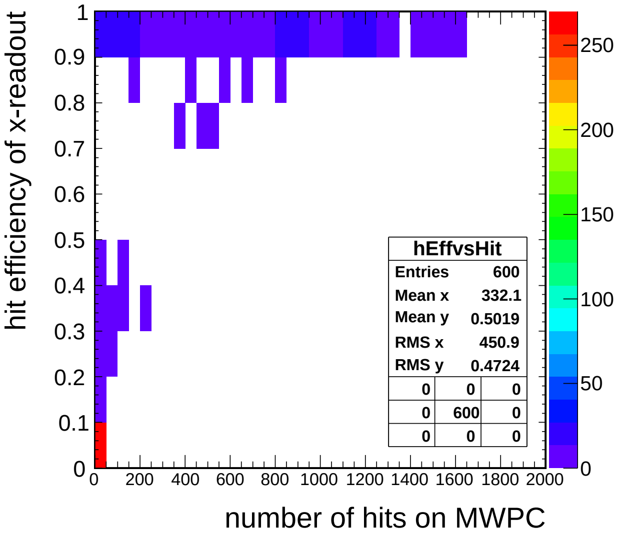

Figure 3.60: Hit efficiency of X-readout versus the number of hits on the MWPC.

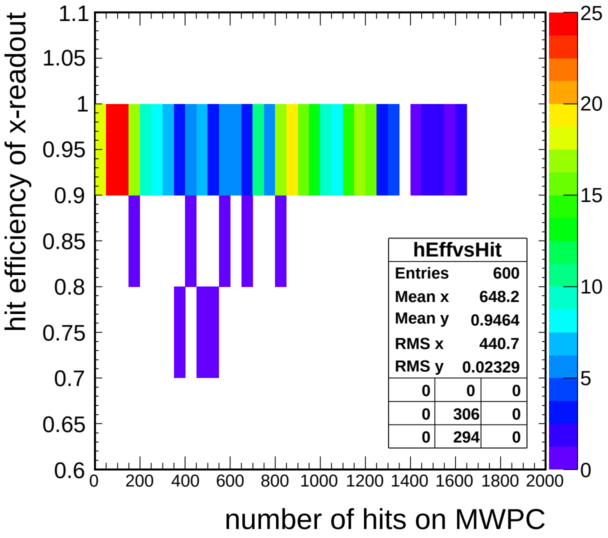

Figure 3.61: Hit efficiency of X-readout versus the number of hits on the MWPC (enlarged).

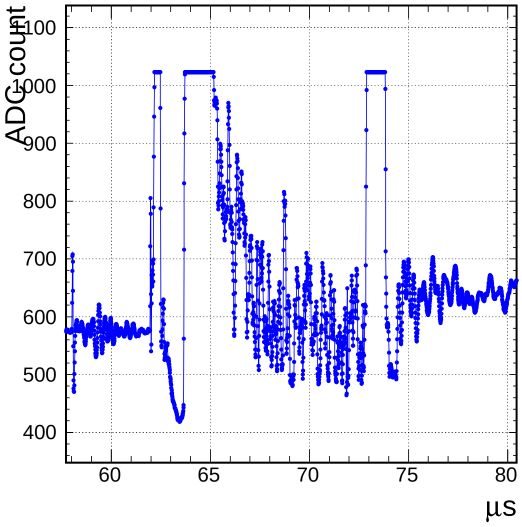

Figure 3.62: Output waveform when beam of 10^7 electrons per pulse from the electron linear accelerator enters the MWPC.

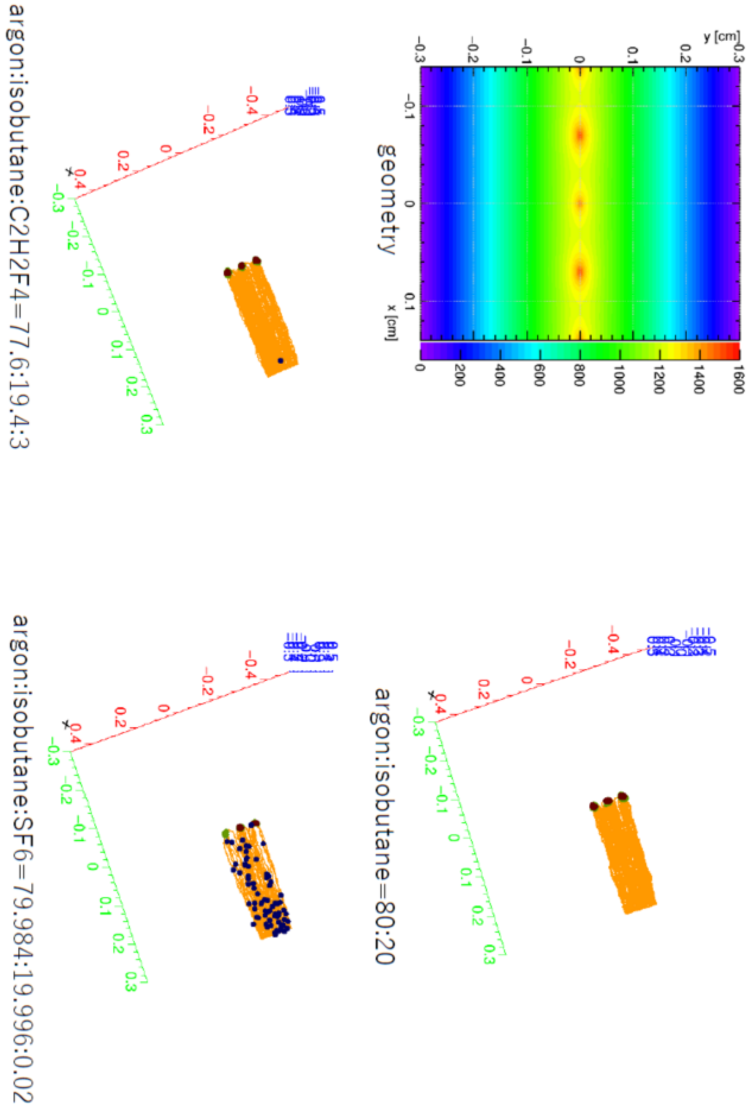

Figure 3.63: Simulations of absorbing electrons during drifting from the cathode plane to the anode wires in various gas mixtures.

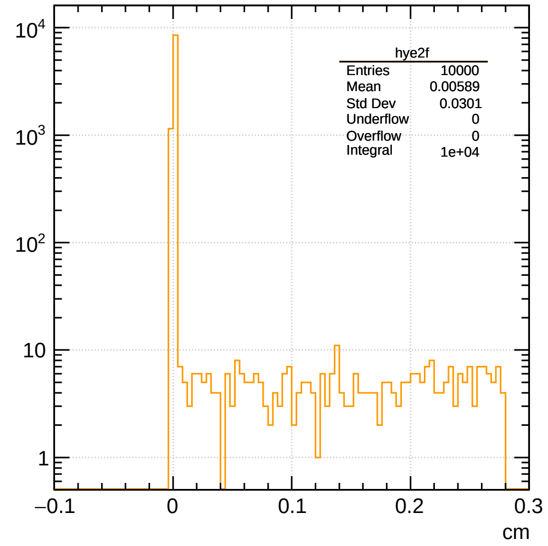

Figure 3.64: Simulation result of where electrons put near the cathode plane are absorbed while drifting to the anode wires for mixing $C_2H_2F_4$ (3%) with argon (80%) isobutane (20%), high voltage applied to the anode and potential wires.

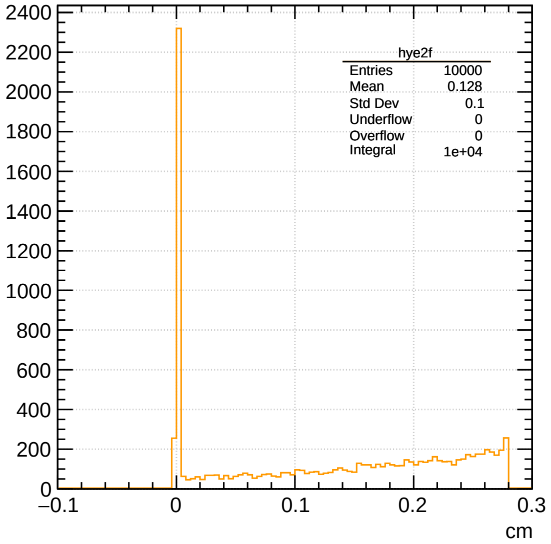

Figure 3.65: Simulation result of where electrons put near the cathode plane are absorbed while drifting to the anode wires for mixing SF_6 (0.02%) with argon (80%) isobutane (20%), high voltage applied to the anode and potential wires.

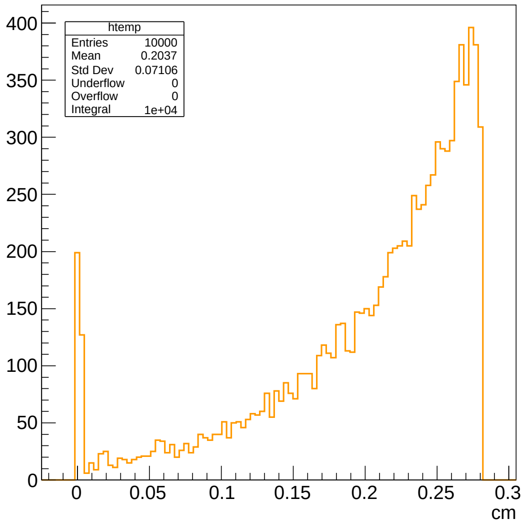

Figure 3.66: Simulation result of where electrons put near the cathode plane are absorbed while drifting to the anode wires for mixing SF_6 (0.05%) with argon (80%) isobutane (20%), high voltage applied to the anode and potential wires.

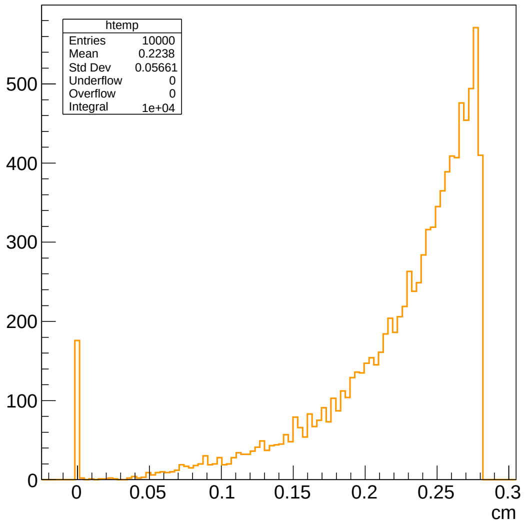

Figure 3.67: Simulation result of where electrons put near the cathode plane are absorbed while drifting to the anode wires for mixing SF_6 (0.02%) with argon (80%) isobutane (20%), high voltage applied to the anode wires and 0 V applied to the potential wires.

Chapter 4

Experiment at J-PARC MLF D2 Area

Muon Decay in Orbit (DIO, $\mu^- \to e^- + \nu_\mu + \overline{\nu_e}$ in the nuclear field) becomes the main background in the experiments searching for μ-e conversion process. In June, 2017, we measured the momentum spectra of muon beam hitting a target made of carbon, silicon or silicon carbide using a spectrometer at J-PARC MLF D2 Area. In this chapter, I want to discuss the setup of the experiment, systematic error, and analysis of the momentum spectra.

4.1 Experimental Setup

4.1.1 Muon Beam

In the experiment, the momenta of muon beam supplied to the D2 Area was 30 MeV/c±5%. The size of beam is 70 mm×70 mm. Tables 4.1 to 4.3 gives the setting of each electromagnet of the D Line when it supplies when it supplied negative muons. The component of the D Line is shown in Fig. 4.1. When it supplied positive muon beam for calibration of spectrometer, the setting value was the value the sign of which are changed.

Table 4.1: Setting of each electromagnet of the D Line when it supplies when it supplied negative muons in the experiment at the D2 Area in June, 2017.

	Polarity	Current Set	Voltage	MODE
DQ01	Negative	-285.0	-17.1	
DQ02	Negative	-192.0	-21.7	
DQ03	Negative	-126.0	-12.4	
DQ04	Positive	94.0	12.7	
DQ05	Positive	118.0	9.6	
DQ06	Positive	73.0	5.9	
DQ07	Positive	38.0	5.0	
DQ08	Positive	40.5	3.0	
DQ09	Positive	31.0	2.5	
DQ10	Negative	0.0	0.0	
DQ11	Negative	0.0	0.0	
DQ12	Negative	0.0	0.0	
DQ13	Positive	38.0	3.0	
DQ14	Positive	52.0	3.8	
DQ15	Positive	74.0	5.9	
DB01	Negative	-260.50	-8.7	1000 A
DB02	Negative	-63.51	-6.8	400 A
DSY12	Positive	35.00	1.9	400 A
DSEPCC		43.00	16.21	

Table 4.2: Gate valve.

	OPEN	CLOSE
DGV1	🟩	
DGV2	🟩	
DGV3-1		🟥
DGV3-2	🟩	

Table 4.3: Beam blocker.

	OPEN	CLOSE
PI	🟩	
D1		🟥
D2	🟩	

The load file of setting was /home/epics/dline/Application/savefile/D2-NDecay-30MeV-161108-4 of the epics PC in the control room.

4.1.2 Target

Four kinds of target made of holmium (Ho), carbon (C), silicon (Si), and silicon carbide (SiC). Figures 4.3 and 4.3 show the photographs of those targets. The shape of the targets is summarized in Table 4.4.

The muons in the beam have polarization, and the form of the momentum spectrum of DIO may change. Because using a holmium target cancels polarization of muon beam, first the data for calibration of momentum was taken by hitting the holmium target with positive muons. In addition, we can measure acceptance of the spectrometer due to positive muons not interacting with atomic nuclei.

In the DeeMe experiment, first a target made of carbon, and we have a plan that the target may be changed in the future so that targets made of carbon and silicon carbide were used. The silicon target was used to inspect the ratio which of silicon and carbon negative muons stopped at the target are captured by, that is, to inspect Fermi-Teller Z law.

4.1.3 Spectrometer

Figure 4.4 shows a photograph of the D2 Area at the time of the experiment in June, 2017. In the upper part of the photograph, there is the exit of the muon beam, and a target is hanged near the exit. Using a spectrometer facing the target, we took data of the momenta of electrons produced through muon decay in orbit.

The tracking detectors, four MWPCs, were put on the footstool. From the upstream of beam, we give them numbers, wire chamber 0 (MWPC 1), wire chamber 1 (MWPC 2), wire chamber 2 (MWPC 3), and wire chamber 3 (MWPC 4). While

Table 4.4: Shape of four kinds of target.

	Width	Height	Thickness
Holmium (Ho)	11 mm	52 mm	1 mm
Carbon (C)	200 mm	200 mm	1 mm

	Diameter	Thickness
Silicon (Si)	4 inches	525 μm
Silicon carbide (SiC)	4 inches	525 μm

two 724-type MWPCs with a wire spacing of 0.75 mm were used as wire chamber 0 and 1, two 713-type MWPCs with a wire spacing of 0.7 mm were used as wire chamber 2 and 3. For reading amplifiers, version 1 and 2 were used in the X-axis and Y-axis readout, respectively, and the resistance of the pole-zero cancelation circuit was set to 1 kΩ. The output signal from the reading amplifiers was carried by long flat cables to the outside of the D2 Area, and the data were taken using FADCs with a sampling rate of 100 MHz. The correspondence between the cathode strips of MWPCs and channel of the FADCs are summarized in Table 4.5.

The electromagnet was leased from KEK Institute of Materials Structure Science Muon Science Laboratory. The power supply of the magnet is was taken from a white power supply on the photograph right side. This is the power supply device to supply electric current to PACMAN magnet in the DeeMe experiment. The amount of coolant was measured by flow meter in the upper left corner of the photograph.

Figure 4.5 illustrates the position relations of the magnet and four MWPCs. A central line is written in each MWPC. This line is the central line of 80-channel cathode strips for the X-axis direction readout (see Figures 4.3 and 4.3). The gap of the X-axis direction of a place each MWPC are put is written in the figure. In addition, for the Y-axis direction (vertical direction), the origin of the coordinate axis is where the center of muon beam is, and it is +208.0 mm to +209.0 mm from the bottom edge of each MWPC. The Z-axis is the direction that the beam goes ahead.

Table 4.5: Correspondence between the cathode strips of MWPCs and channel of the FADCs. It is written in order of negative to positive of the coordinates.

	FADC channel (ch)
Wire chamber 0	
X-axis readout	FI02 ch31–16, FI03 ch0–15, FI03 ch31–16, FI04 ch0–15, FI04 ch31–16
Y-axis readout	FI02 ch15–0
Wire chamber 1	
X-axis readout	FI05 ch31–16, FI06 ch0–15, FI06 ch31–16, FI07 ch0–15, FI07 ch31–16
Y-axis readout	FI05 ch15–0
Wire chamber 2	
X-axis readout	FI10 ch31–16, FI11 ch0–15, FI11 ch31–16, FI15 ch0–15, FI15 ch31–16
Y-axis readout	FI10 ch15–0
Wire chamber 3	
X-axis readout	FI16 ch31–16, FI17 ch0–15, FI17 ch31–16, FI20 ch0–15, FI20 ch31–16
Y-axis readout	FI16 ch15–0

4.1.4 Logic Circuit and Triggers

Figure 4.8 briefly describes the logic circuit at the time of the experiment. The trigger of the whole logic circuit is taken from the trigger of “RCS extraction”. This includes the cases that proton beam comes to MLF and that proton beam goes to the main ring. The former one is used to take data for our analysis, while the latter is taken to calibrate the data.

The RCS extraction trigger is then divided into the following signals using fan-in/out:

- Start signal of the FADCs for the MWPCs and copper FADC. While the FADCs for the MWPCs can take waveform for approximately 80 μs, the copper FADC can do it for 8 μs. After appropriate timing adjustment by putting delay, the start signal is input into two kinds of FADC. The busy signal from two kinds of FADC is input into another fan-in/out, and the output is input in veto of the module giving the start signal.
- The random pulse signal of the reading amplifiers. After the level translator it is input in one of the inputs of coincidence. The other input is NIM signal from function generator with a slightly different frequency from the frequency of RCS extraction trigger (25 Hz), and the output of the coincidence module becomes random signal in NIM level. The signal is input into two test pulse boards, and then the test pulse is carried to the reading amplifiers. In the output waveform, the signal of test pulse is seen to test the FADCs for the MWPCs.
- Gate of HV switching on the potential wires of the MWPCs. After going through level translator, its width is changed into 10 μs by using function generator. Two signals reproduced by fan-in/out are changed into TTL signals by level translator and are input to the TTL input of two HV switching modules. The timing adjustment of HV switching gate is performed by seeing the timing between the monitor-out signal of HV switching module and signal of decay particles in two counters put in the top right corner of Fig. 4.4 (see Fig. 4.9).

4.2 Data

Data taken in the beam time of 120 hours from June 23rd 9:00 AM to 28th 9:00 AM, 2017 is briefly summarized in Table 4.6.

Table 4.6: Data taken in the beam time of 120 hours from June 23rd 9:00 AM to 28th 9:00 AM, 2017. (Prompt cut) means the data in which decay particles of prompt timing are taken off the gate of HV switching, that is the analysis window. After the data was taken, timing was returned to the original timing. For more detailed information, please refer to No. 9 of DeeMe experiment notebook.

Target	Muon charge	Momentum [MeV/c]	Number of triggers	Run number
Holmium	Positive	52.5	4.6×10^5	6049–6116
		45	3.5×10^5	6122–6158
		40	1.4×10^5	6159–6174
		60	1.5×10^5	6195–6210
Carbon		52.5	2.3×10^5	6233–6257
		45	4.6×10^5	6258–6306
	Negative	52.5	1.6×10^5	6320–6335
		45	1.8×10^5	6337–6354
		55	6.3×10^5	6355–6419
	(prompt cut)		1.6×10^5	6420–6435
Silicon		52.5	1.4×10^5	6437–6450
		45	1.4×10^5	6452–6465
		55.5	4.8×10^5	6469–6524
Silicon carbide		52.5	1.5×10^5	6525–6540
		45	1.6×10^5	6541–6556
		55	1.7×10^6	6557–6745

4.3 Analysis

Transporting positron beam with a monochromatic momentum of 52.5 MeV/c in the g4beamline simulation, it was calibrated by seeing the number of hits on wire chamber 3 as a function of magnet scale. It was then calibrated to be a mean momentum of 52.5 MeV/c changing magnet scales of track fit. Calibration using the edge of usual decay (Michel decay) is made as shown in Fig. 4.12, and then the momentum spectra of low momentum positrons and decay in orbit around 52.5 MeV/c and 55 MeV/c are compared with the theoretical calculations.

Figure 4.13 shows momentum spectra of data (black) and simulation (red) of negative muon beam with a magnet setting 52.5 MeV/c. The data results agree with the Monte Carlo simulations within a few root mean squares.

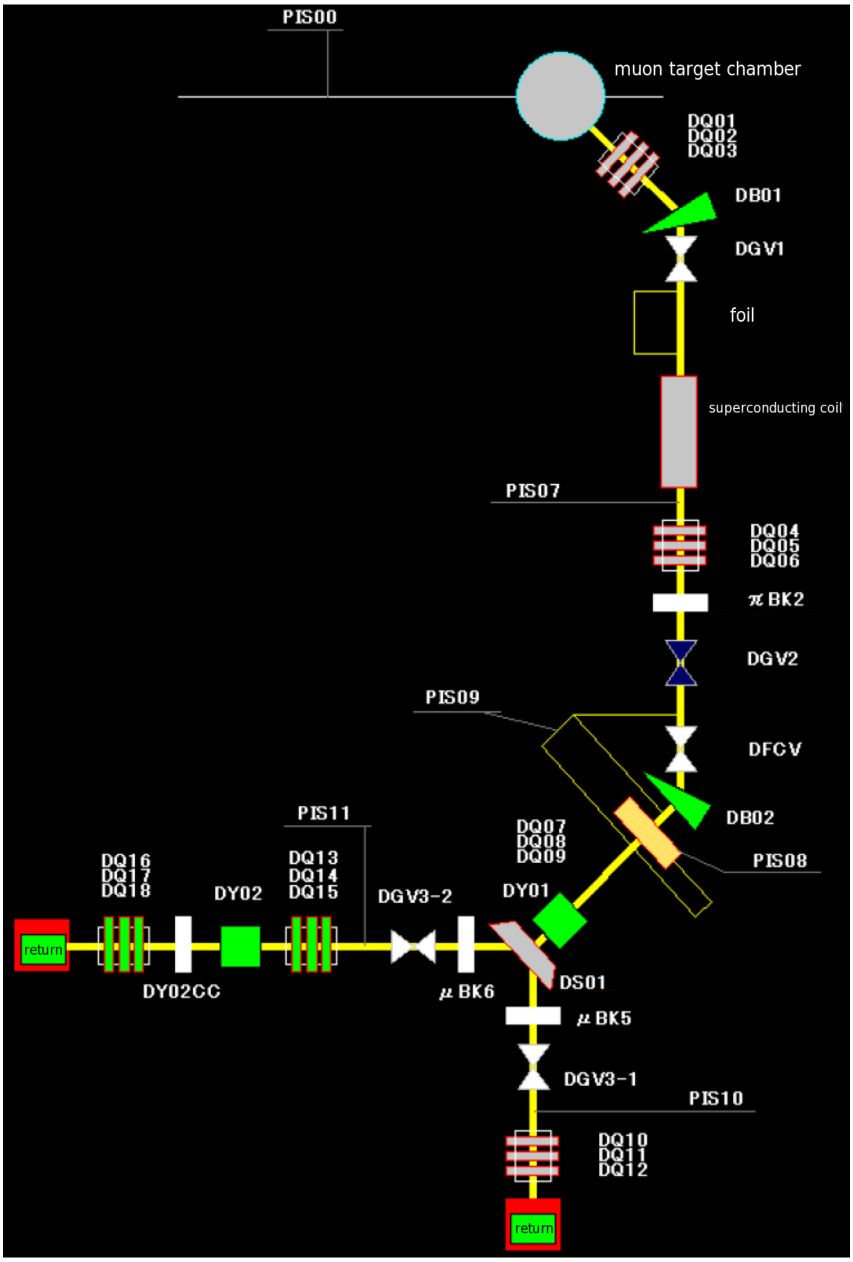

Figure 4.1: Component of the D Line [38].

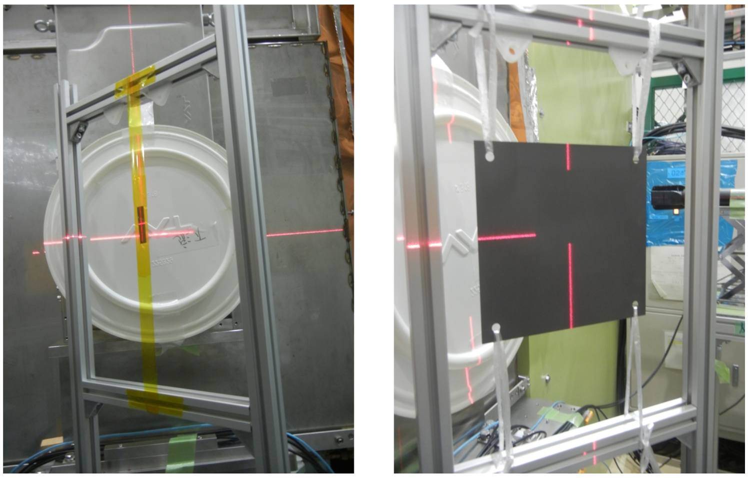

Figure 4.2: Photographs of targets made of holmium (left) and carbon (right).

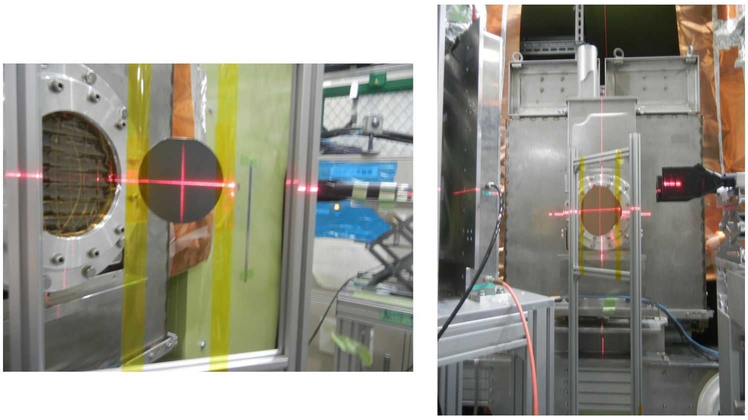

Figure 4.3: Photographs of targets made of silicon (left) and silicon carbide (right).

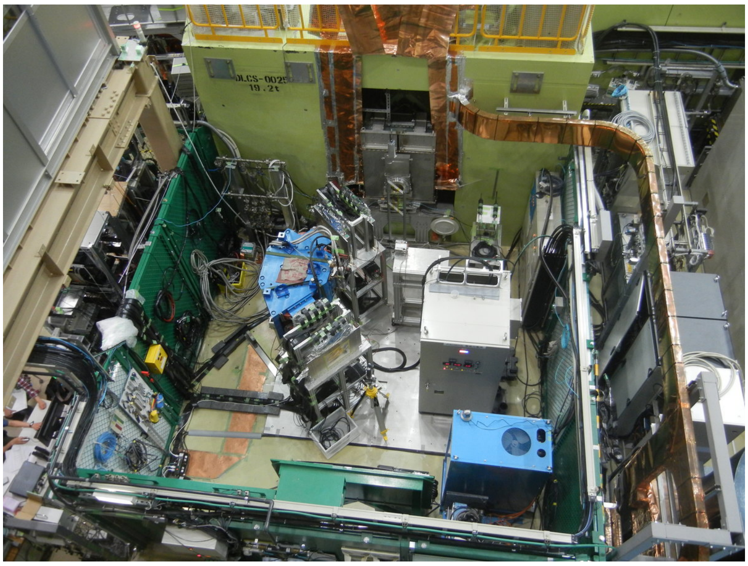

Figure 4.4: Photograph of the D2 Area at the time of the experiment in June, 2017.

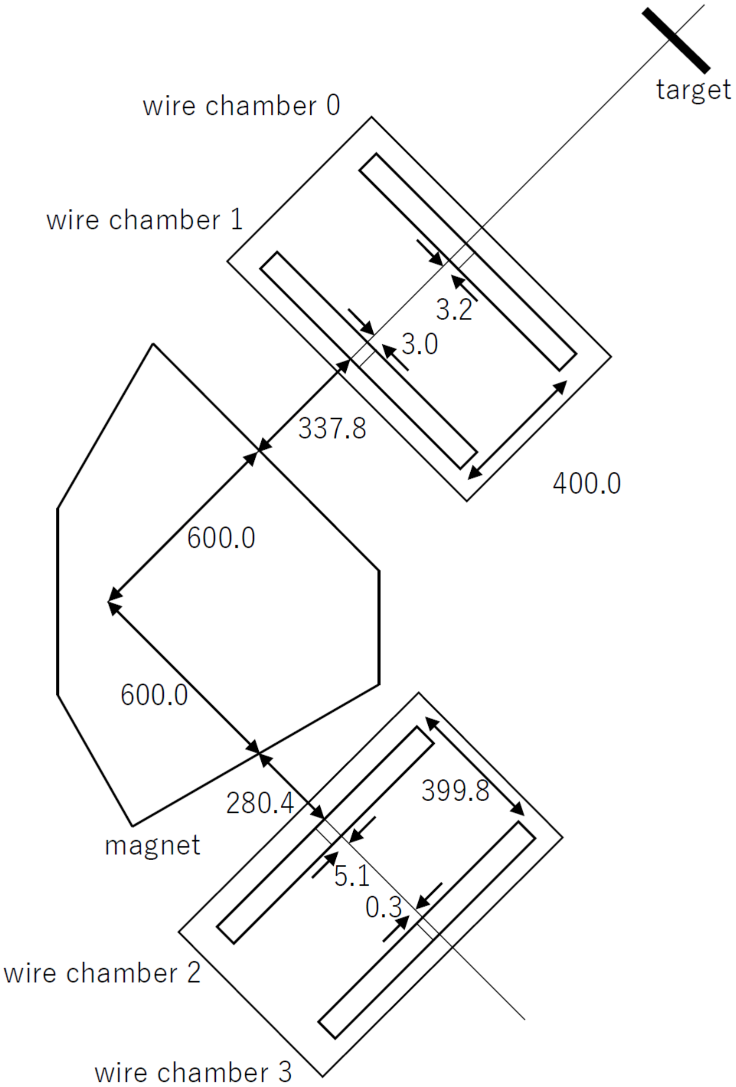

Figure 4.5: Position relations of the magnet and four MWPCs.

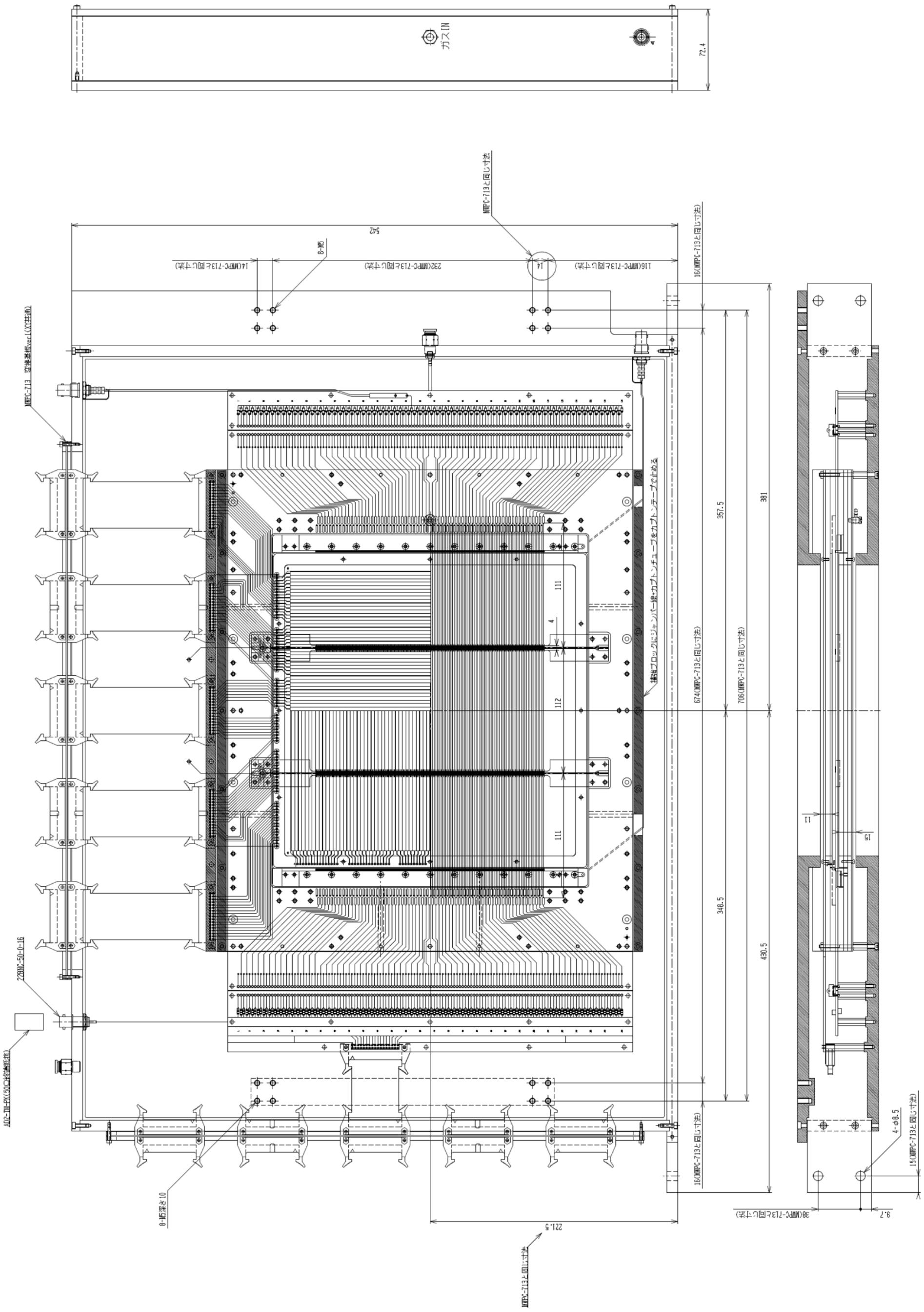

Figure 4.6: Drawing of the 724-type MWPC used for wire chamber 0 and 1.

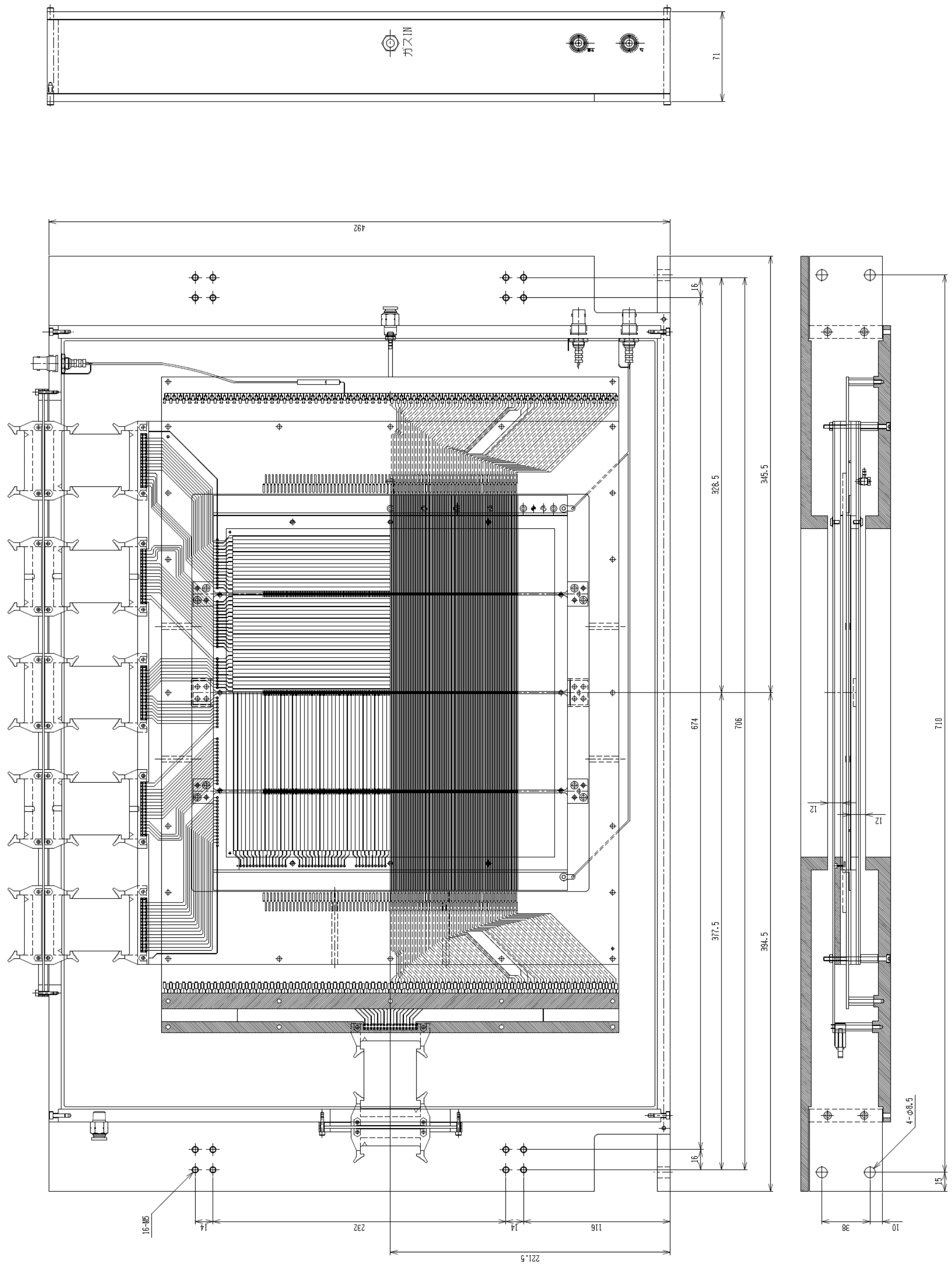

Figure 4.7: Drawing of the 713-type MWPC used for wire chamber 2 and 3.

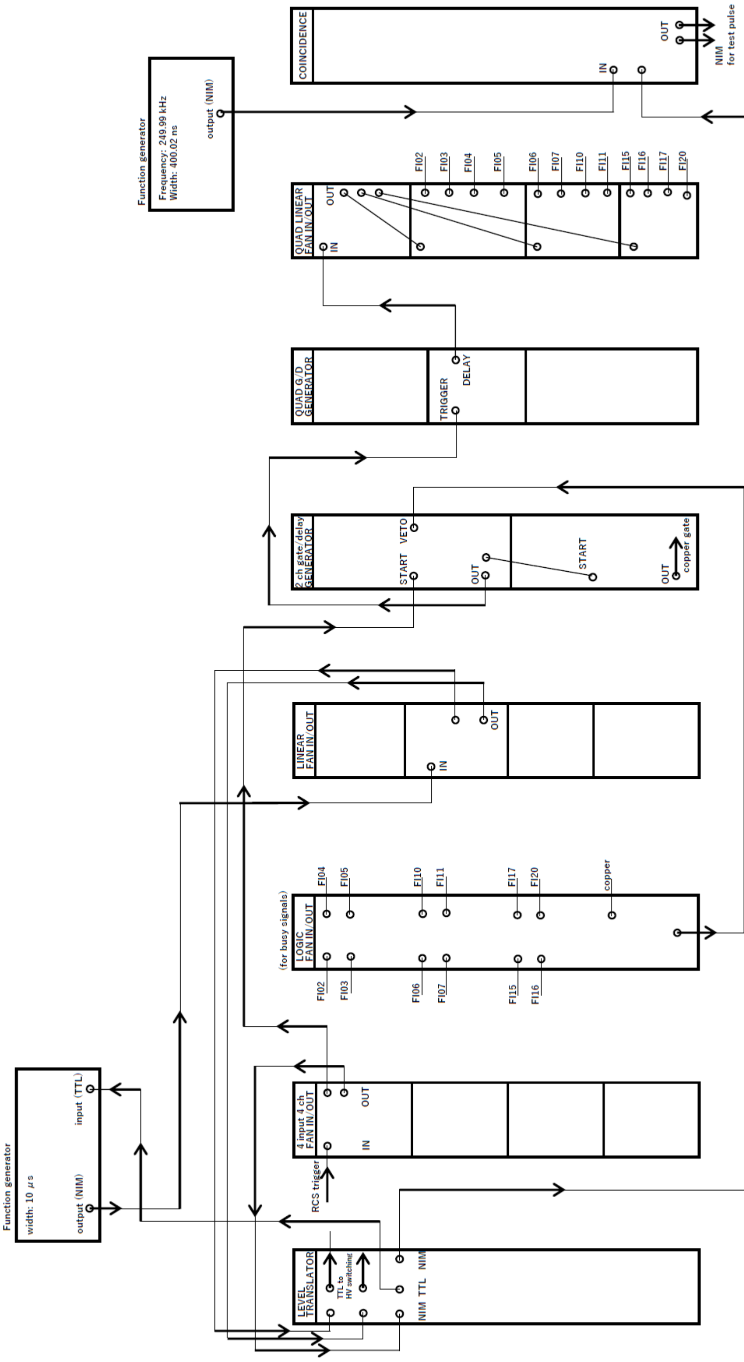

Figure 4.8: Logic circuit at the time of the experiment (briefly summarized).

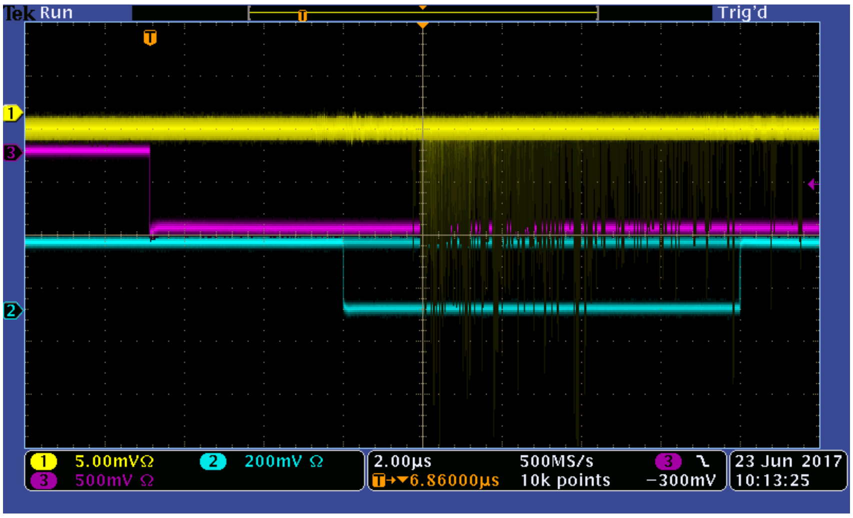

Figure 4.9: Oscilloscope screen shot for timing adjustment between the monitor-out signal of HV switching module (blue) and signal of decay particles in the counter put in the top right corner of Fig. 4.4 (yellow).

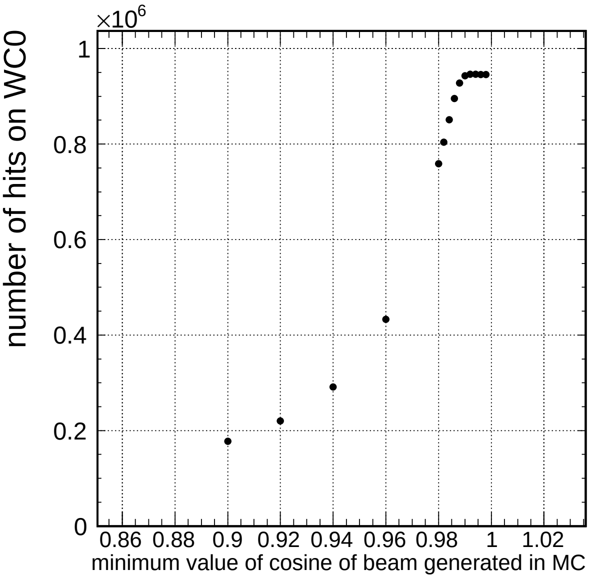

Figure 4.10: Number of hits on wire chamber 0 versus minimum value of cosine of beam generated in Monte Carlo.

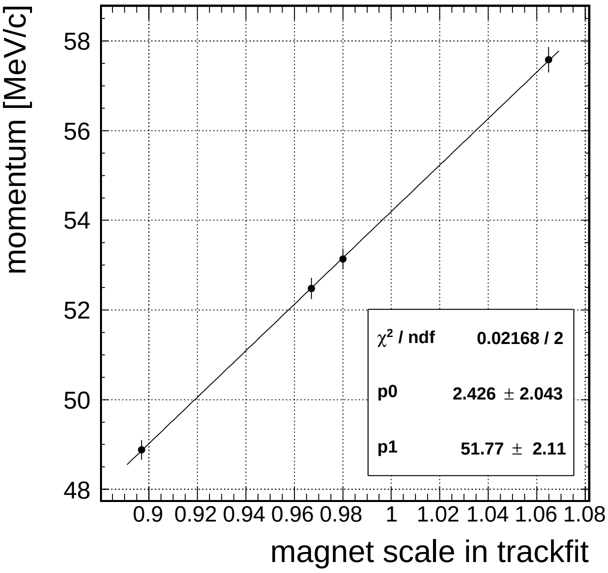

Figure 4.11: Momentum [MeV/c] versus magnet scale in trackfit.

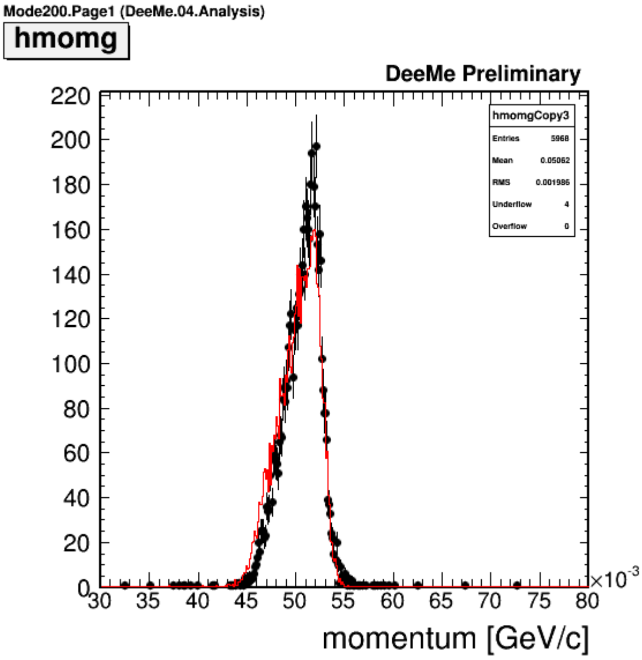

Figure 4.12: Momentum spectra of data (black) and simulation (red) of positive muon beam with a magnet setting 52.5 MeV/c.

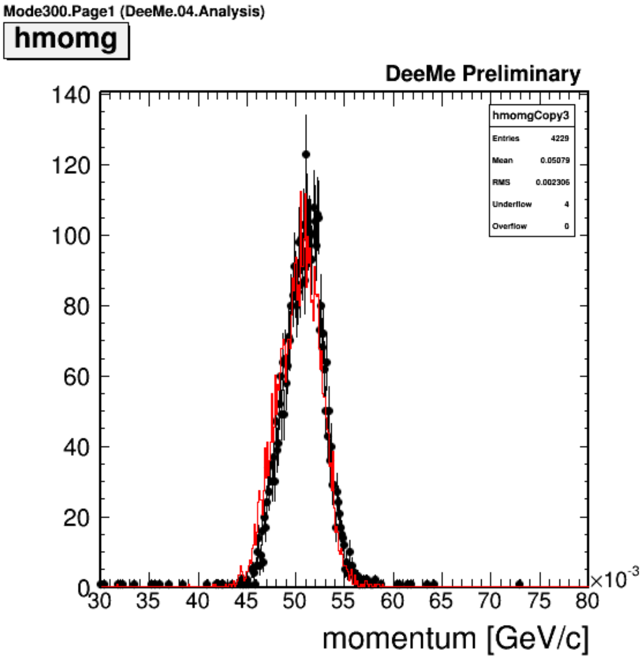

Figure 4.13: Momentum spectra of data (black) and simulation (red) of negative muon beam with a magnet setting 52.5 MeV/c.

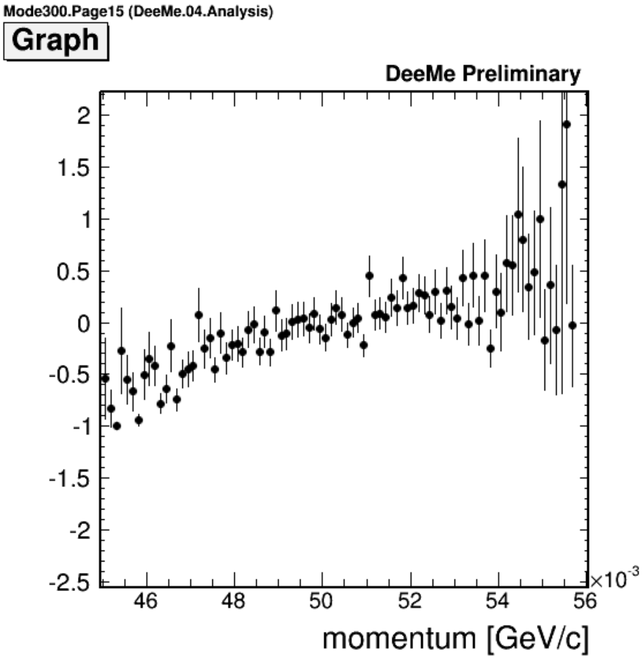

Figure 4.14: The ratio of momentum spectra of data (black) to simulation (red) of negative muon beam with a magnet setting 52.5 MeV/c in Fig. 4.13.

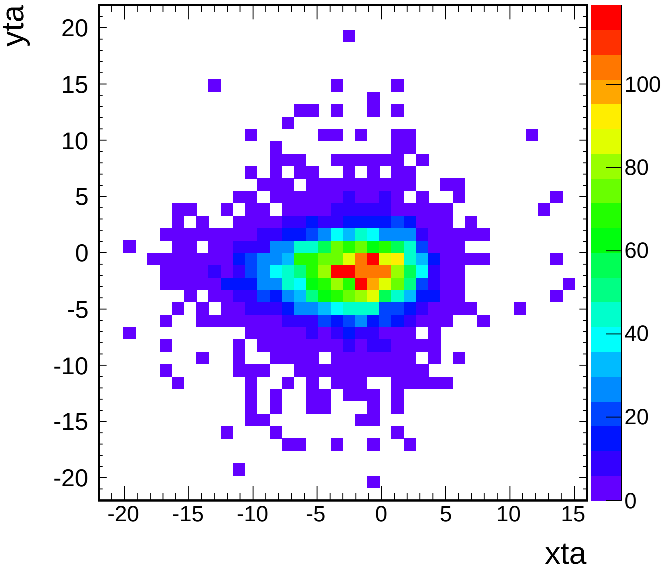

Figure 4.15: Track back distribution of data analysis.

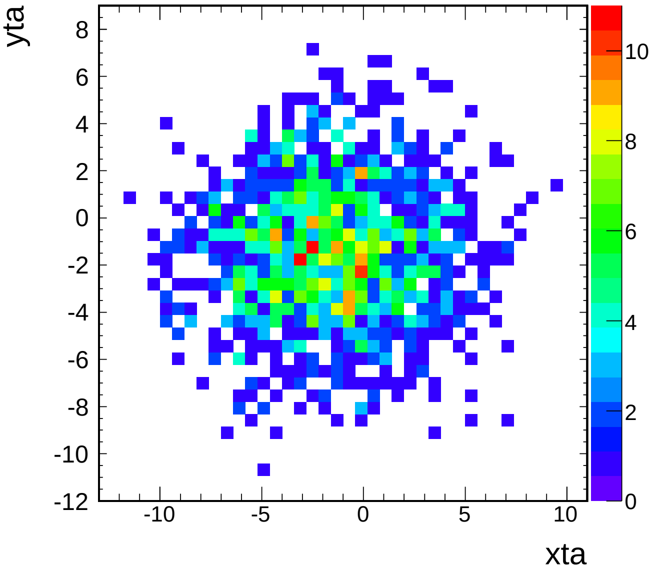

Figure 4.16: Track back distribution of Monte Carlo simulation.

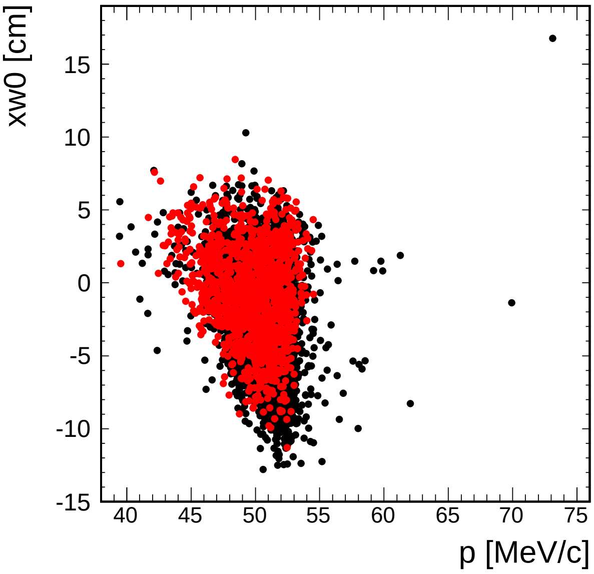

Figure 4.17: Track position in X-direction on wire chamber 0 versus momentum of data (black) and Monte Carlo simulation (red).

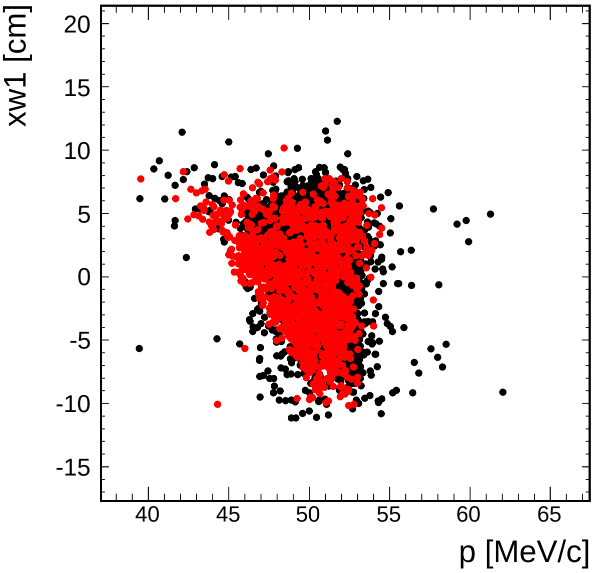

Figure 4.18: Track position in X-direction on wire chamber 1 versus momentum of data (black) and Monte Carlo simulation (red).

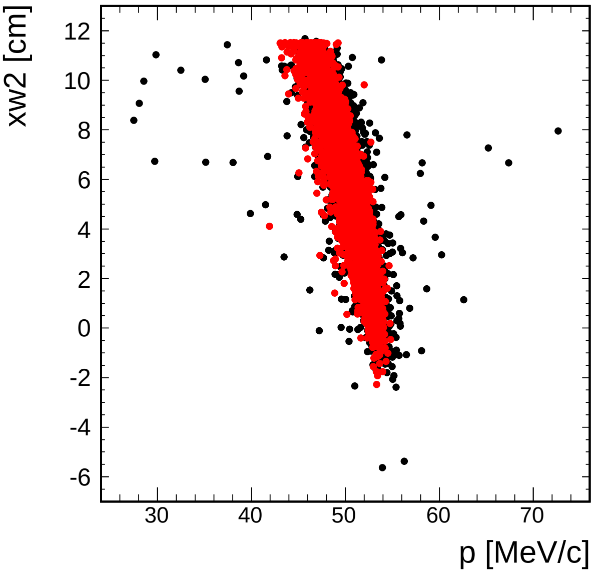

Figure 4.19: Track position in X-direction on wire chamber 2 versus momentum of data (black) and Monte Carlo simulation (red).

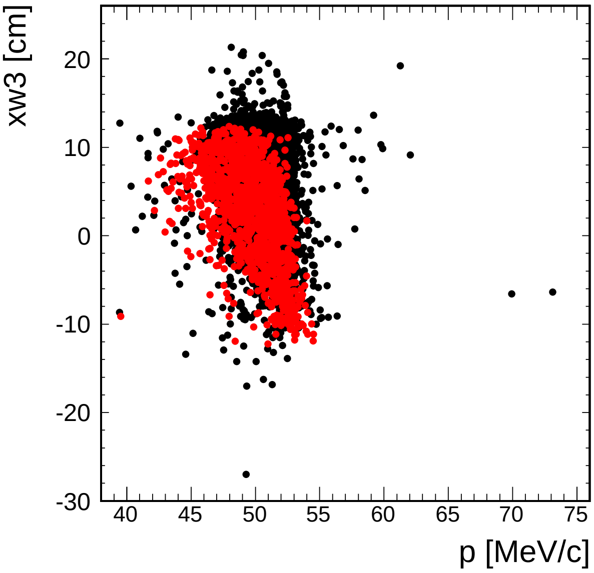

Figure 4.20: Track position in X-direction on wire chamber 3 versus momentum of data (black) and Monte Carlo simulation (red).

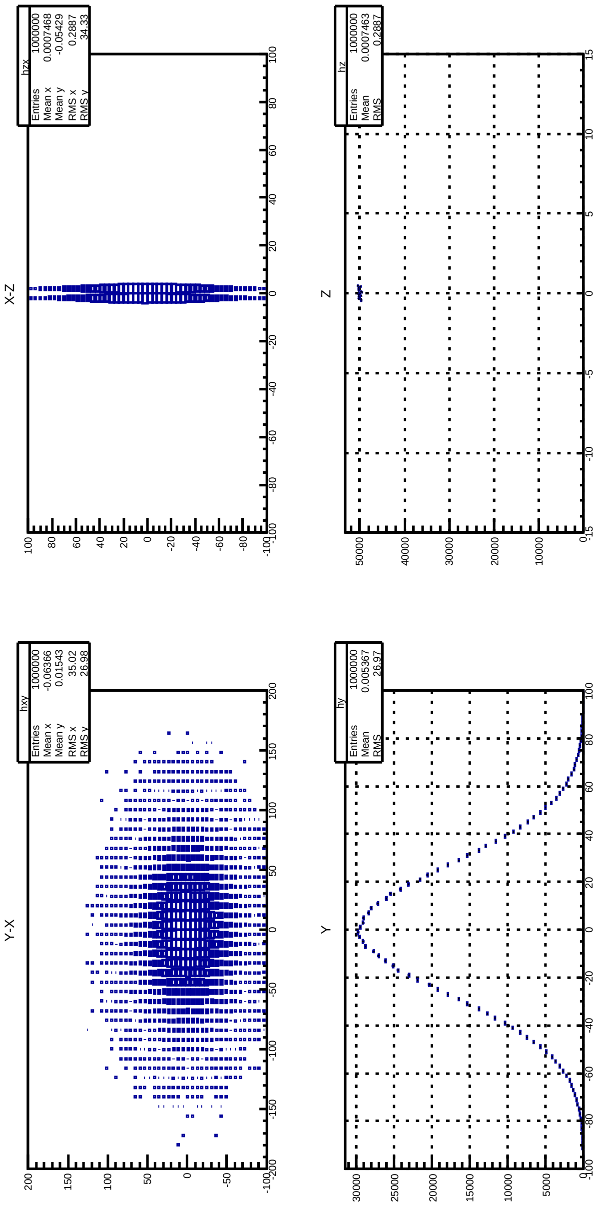

Figure 4.21: Beam shape for positive muon beam in Monte Carlo simulation.

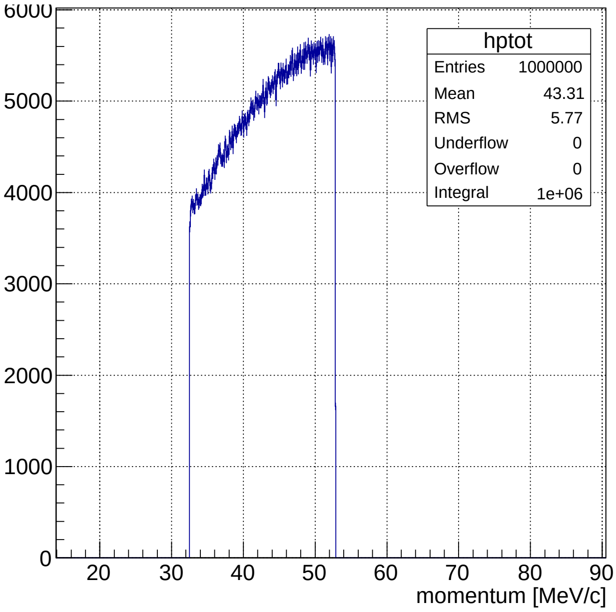

Figure 4.22: Momentum distribution for positive muon beam in Monte Carlo simulation.

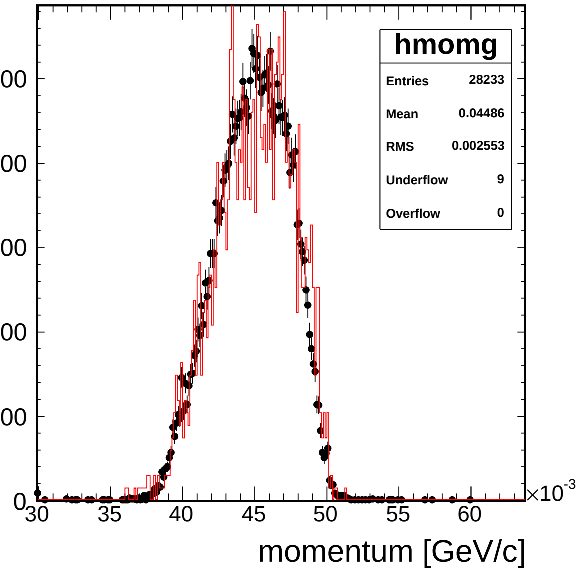

Figure 4.23: Momentum spectra of data (black) and simulation (red) of positive muon beam with a magnet setting 45 MeV/c.

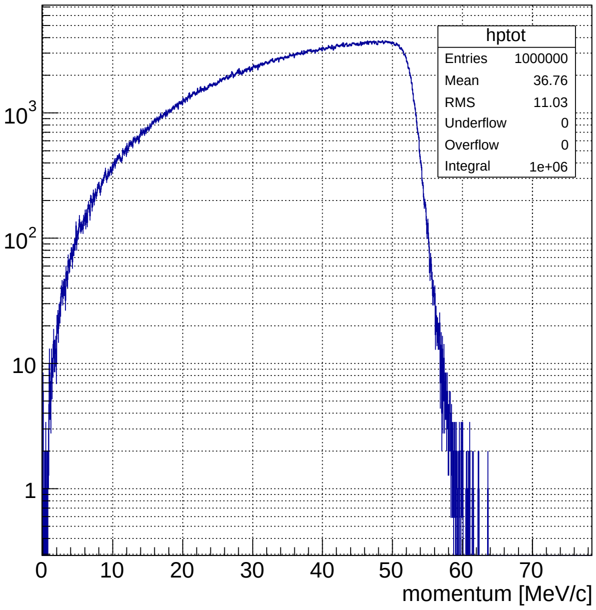

Figure 4.24: Momentum distribution of muon decay in orbit of Czarnecki model for negative muon beam in Monte Carlo simulation.

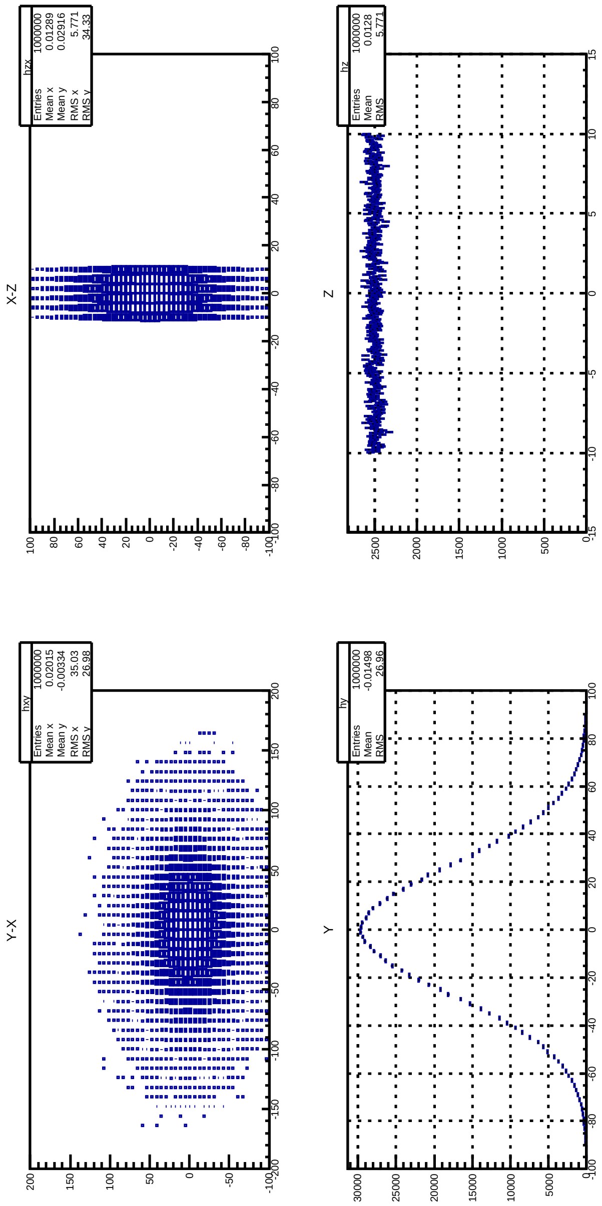

Figure 4.25: Beam shape for negative muon beam in Monte Carlo simulation.

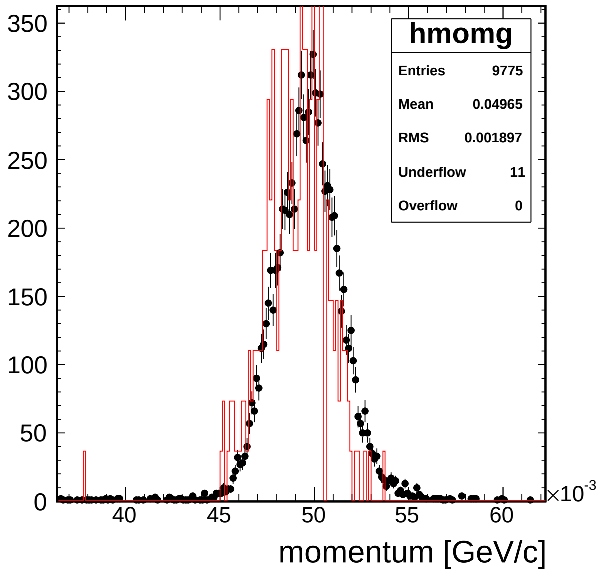

Figure 4.26: Momentum spectra of data (black) and simulation (red) of muon decay in orbit for a magnet setting 55 MeV/c.

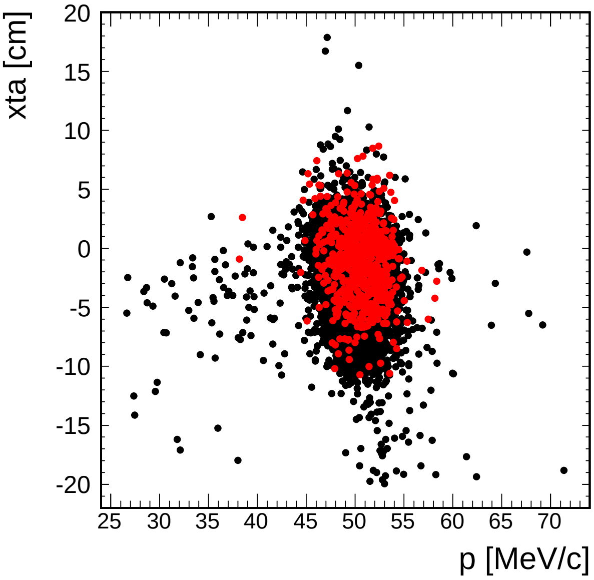

Figure 4.27: Track back position in X-direction versus momentum of data (black) and Monte Carlo simulation (red).

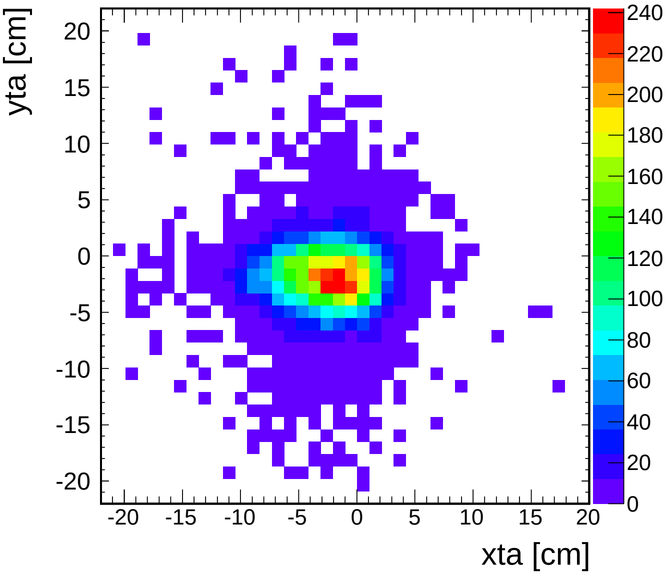

Figure 4.28: Track back distribution of data analysis.

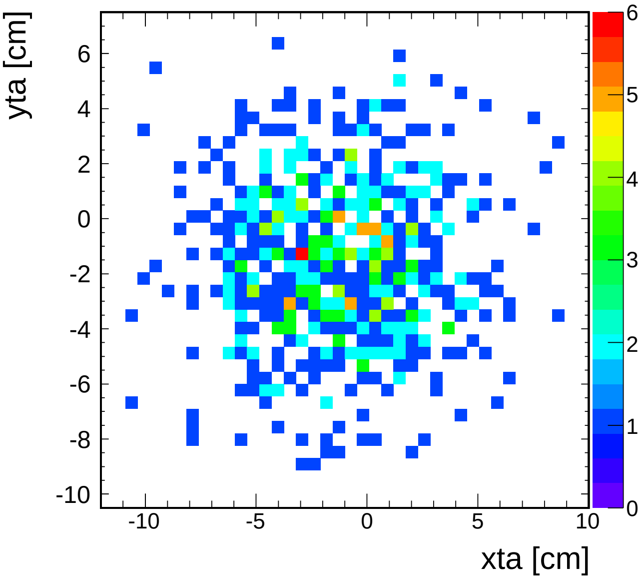

Figure 4.29: Track back distribution of Monte Carlo simulation.

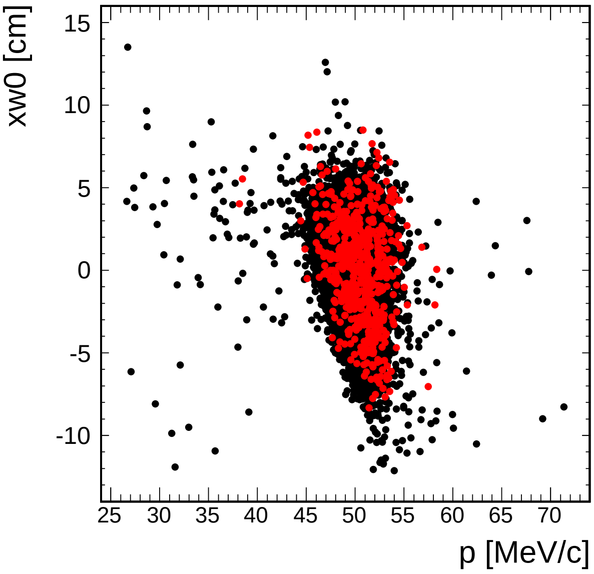

Figure 4.30: Track position in X-direction on wire chamber 0 versus momentum of data (black) and Monte Carlo simulation (red).

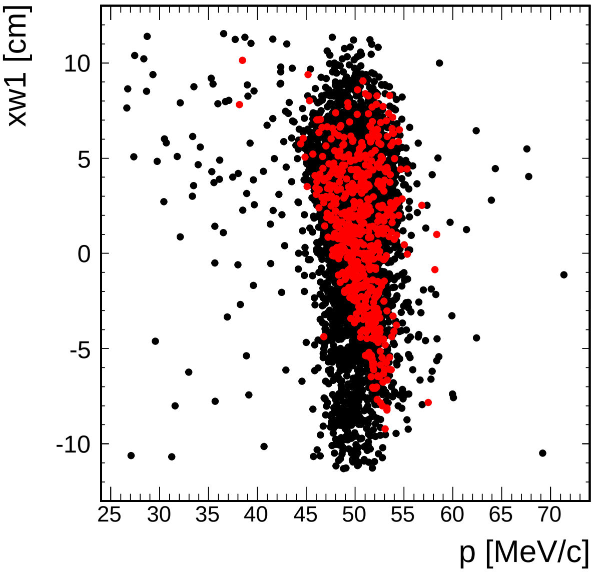

Figure 4.31: Track position in X-direction on wire chamber 1 versus momentum of data (black) and Monte Carlo simulation (red).

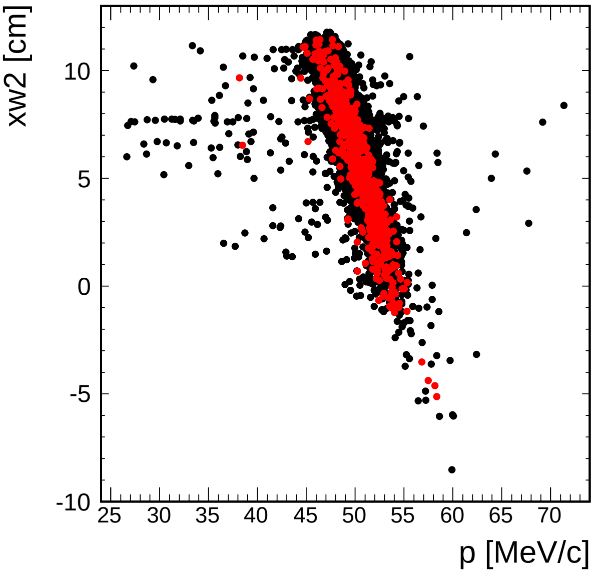

Figure 4.32: Track position in X-direction on wire chamber 2 versus momentum of data (black) and Monte Carlo simulation (red).

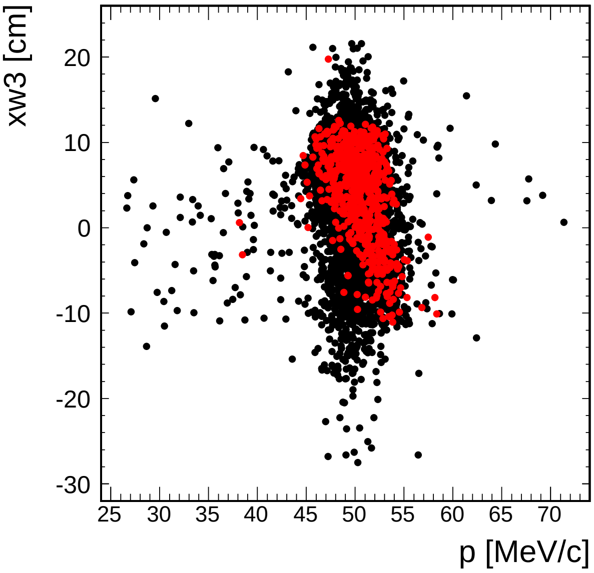

Figure 4.33: Track position in X-direction on wire chamber 3 versus momentum of data (black) and Monte Carlo simulation (red).

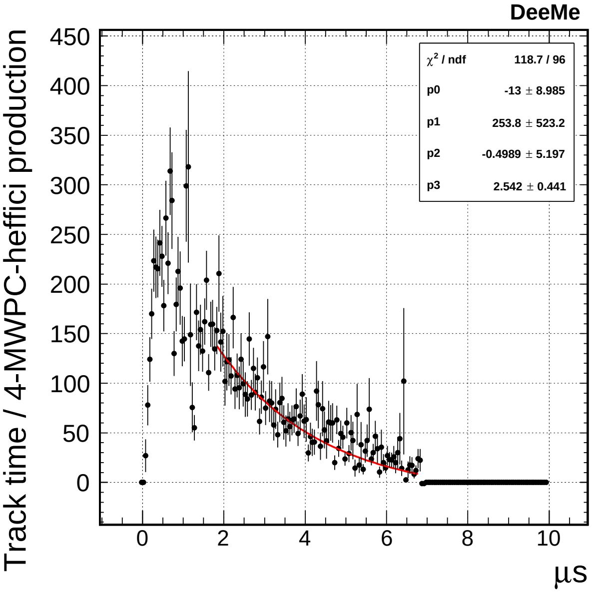

Figure 4.34: Track as a function of time for positive muon beam hitting the carbon target with a magnet setting 45 MeV/c.

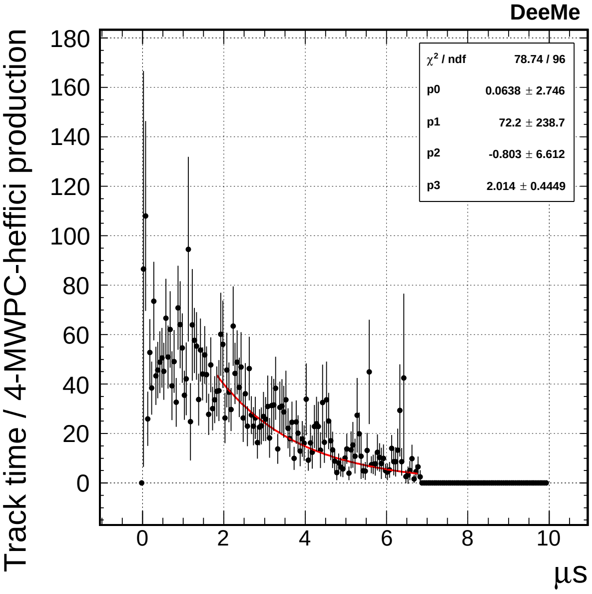

Figure 4.35: Track as a function of time for negative muon beam hitting the carbon target with a magnet setting 45 MeV/c.

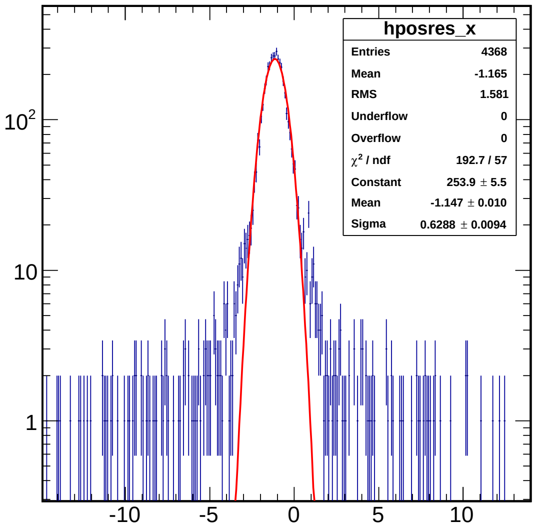

Figure 4.36: Fitted position minus hit position of hits on wire chamber 0 in X-readout.

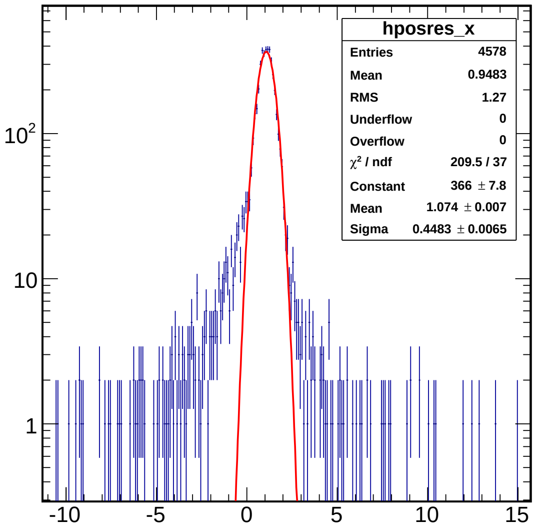

Figure 4.37: Fitted position minus hit position of hits on wire chamber 1 in X-readout.

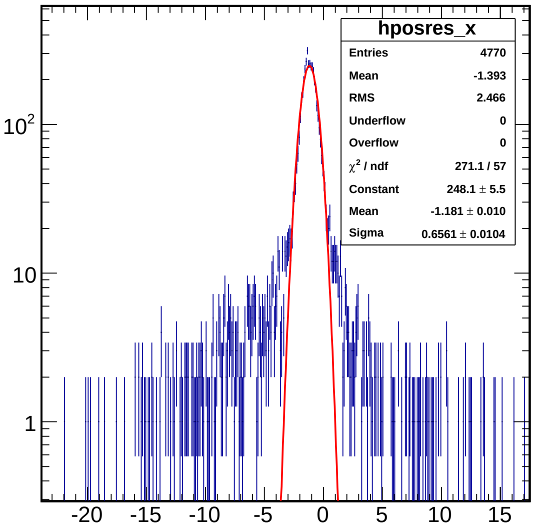

Figure 4.38: Fitted position minus hit position of hits on wire chamber 2 in X-readout.

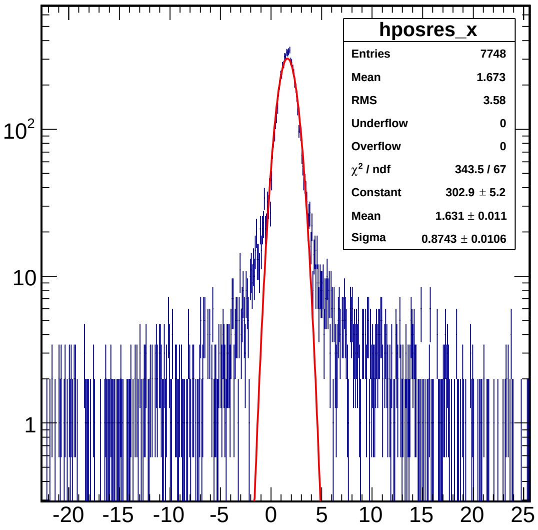

Figure 4.39: Fitted position minus hit position of hits on wire chamber 3 in X-readout.

Chapter 5

Conclusion

The Standard Model of particle physics successfully describes all phenomena observed in experiments so far. However, the hint of new physics beyond the Standard Model is not provided yet. At present, much focus is being placed on searching for rare reaction processes of particle interactions as a search for new physics. The preparation status of DeeMe experiment, an experimental plan to search for muon-to-electron conversion that is not yet discovered, is presented.

In the experiment, a signal of muon-to-electron conversion is an electron with a monochromatic energy of 105 MeV, and we search for it using a magnetic spectrometer. The spectrometer consists of four tracking detectors, multi-wire proportional chambers (MWPCs), and a magnet called PACMAN. The MWPCs have reading cathode strips, and anode and potential wires stretched alternately, to which high voltage applied momentarily at the timing of searching for a signal. We discuss development of these innovative MWPCs including optimization of filling gases, improvement of the reading circuits, and the test of suppressing oscillation on the output waveform induced by the high voltage switching. The detection efficiency for an electron improved by two times of that for the old setting as the whole magnetic spectrometer.

In June, 2017, we measured momentum spectra of muon decay in orbit, which is a main background in DeeMe experiment, at J-PARC Material and Life Science Experimental Facility (MLF) D2 Area. In this experiment, the MWPCs and a magnet of KEK Muon Science Laboratory was used. After calibration of the magnetic spectrometer, the momentum was analyzed. The data results agree with the Monte Carlo simulations within a few root mean squares.

Appendix A

Electronic Parts List

Here are some electronic parts lists of electronics mass-produced in financial year 2017. The drawings and parts lists of v1.0 amplifier, power supply board, test pulse board and shield case are found in master's thesis [27] (Japanese). Parts highlighted in yellow are different from previous version.

A.1 Mother Board of Amplifier for Y-axis Readout (v2.0)

Here is the electric parts list for the mother board (v1.1) of Y-axis direction readout amplifier of the DeeMe multi-wire proportional chamber.

Table A.1: Electronic parts list of the mother board (v1.1) for Radeka-type two-stage amplifier Y-axis direction readout (v2.0).

	Brand	Types of products	Mfr. part no.	Reference	Quantity per board
1	HONDA	Input connector	MFC-34LFD+	BERG34	1
2	Hirose Electric	Output connector	HIF3BA-40PA-2.54DS	FLAT40	1

Table A.2: Electronic parts list of the mother board (v1.1) for Radeka-type two-stage amplifier Y-axis direction readout (v2.0).

	Brand	Types of products	Mfr. part no.	Reference	Quantity per board
3	KOA	Through hole fixed resistor	MFS1/4 51Ω	R1, R11, R12	3
4	BI Technologies / TT Electronics	Array resistor	M9-1-470	R2, R8	2
5	MURATA	Ceramic multilayer capacitor	RPER71H104 K2S1A03A	C1, C7, C10, C11	4
6	TEXAS INSTRUMENTS	Differential amplifier	TL592BP	IC01	1
7	KOA	Through hole fixed resistor	MOS1/2CT52 A10R0F	R9, R10	2
8	Nippon Chemi-Con	Ceramic multilayer capacitor	KTD101B155 M43A0T00	C2, C3, C8, C9	4
9	TEXAS INSTRUMENTS	Linear voltage regulator	LM337LZ/NO PB	SY1	1
10	KOA	Through hole fixed resistor	1/4W metal film R 1.5 kΩ (MF1/4CC15 01F)	R7	1
11	KOA	Through hole fixed resistor	MFS1/4 1 kΩ (MFS1/4CC1 001F)	R5	1

Table A.3: Electronic parts list of the mother board (v1.1) for Radeka-type two-stage amplifier Y-axis direction readout (v2.0).

	Brand	Types of products	Mfr. part no.	Reference	Quantity per board
12	KOA	Through hole fixed resistor	1/2W metal film R 300 kΩ (MF1/2CC3000F)	R13	1
13	KOA	Through hole fixed resistor	1/2W metal film R 100 kΩ (MF1/2CC1000F)	R3	1
14	KOA	Through hole fixed resistor	MFS1/4R 240 Ω (MFS1/4CC2400F)	R4	1
15	KOA	Through hole fixed resistor	MFS1/4R 1.1 kΩ (MFS1/4CC1101F)	R6	1
16	Matsuo Electric	Tantalum capacitor	204N2502155K4	C6	1
17	Vishay	Zener diode	1N5233B-TR	D1	1
18	OMRON	IC socket	XR2C2011N	No reference	16

A.2 Daughter Card of Amplifier for Y-axis Readout (v2.0)

Here is the electric parts list for the daughter card (v2.0) of Y-axis direction readout amplifier of the DeeMe multi-wire proportional chamber.

Table A.4: Electronic parts list of the daughter card for Radeka-type two-stage amplifier Y-axis direction readout (v2.0).

	Brand	Types of products	Mfr. part no.	Reference	Quantity per board
1	Panasonic	Switching diode	MA3X157A	D1A, D1B, D2A, D2B	2
2	KEMET	Ceramic multilayer capacitor	C0603C109C5GACTU	C1	1
3	MURATA	Ceramic multilayer capacitor	GRM188B11E104KA01D	C3, C21	2
4	KOA	Surface mount fixed resistor	RK73B2BTTD220J	R30	1
5	NEC	NPN bipolar transistor	2SC3585-T1B	Q1	1
6	KOA	Surface mount fixed resistor	RK73B2ATTD273J	R1	2
7	KOA	Surface mount fixed resistor	RK73B2ATTD562J	R12	2
8	KOA	Surface mount fixed resistor	RK73B2ATTD363J	R2	1

Table A.5: Electronic parts list of the daughter card for Radeka-type two-stage amplifier Y-axis direction readout (v2.0).

	Brand	Types of products	Mfr. part no.	Reference	Quantity per board
9	KOA	Surface mount fixed resistor	RK73B2ATTD 912J	R3	1
10	KOA	Surface mount fixed resistor	RK73H2ATTD 51R0F	R4, R19, R20	3
11	KOA	Surface mount fixed resistor	RK73B2ATTD 473J	R5	1
12	NXP	NPN bipolar transistor	BSV52(,215)	Q2, Q3, Q4, Q5	4
13	KOA	Surface mount fixed resistor	RK73B2ATTD 330J	R6, R7, R13, R15, R16	5
14	ON Semiconductor	Zener diode	MMSZ5233BT 1G	Z1	1
15	KOA	Surface mount fixed resistor	RK73B2ATTD 682J	R8	1
16	MURATA	Ceramic multilayer capacitor	GRM31MB11E 105KA01L	C2, C4, C5, C6, C41	5
17	MURATA	Ceramic multilayer capacitor	GRM155B11H 271KA01D	C17	1
18	KOA	Surface mount fixed resistor	RK73H1JTTD 1000F	R29	1

Table A.6: Electronic parts list of the daughter card for Radeka-type two-stage amplifier Y-axis direction readout (v2.0).

	Brand	Types of products	Mfr. part no.	Reference	Quantity per board
19	KOA	Surface mount fixed resistor	RK73H1JTTD 2001F	R10	1
20	KOA	Surface mount fixed resistor	RK73H1JTTD 1001F	R11	1
21	Bourns	Potentiometer	3382G-1-103G	R9	1
22	KOA	Surface mount fixed resistor	RK73B1JTTD 562J	R14	1
23	NEC	NPN bipolar transistor	2SC3356-T1B	Q6	1
24	KOA	Surface mount fixed resistor	RK73B1JTTD 152J	R17	1
25	KOA	Surface mount fixed resistor	RK73H1JTTD 43R0F	R18	1
26	KOA	Surface mount fixed resistor	RK73H1JTTD 10R0F	R31, R32	2
27	MURATA	Ceramic multi-layer capacitor	GRM31MB11 H224KA01L	C15, C16	2
28	MAC8	For hybrid manufacturing	CB-1-5	No reference	11

A.3 Amplifier for X-axis Direction Readout (v3.0)

Here is the electric parts list for the daughter card (v3.0) of improved X-axis direction readout amplifier of the DeeMe multi-wire proportional chamber.

Table A.7: Electronic parts list of the daughter card for Radeka-type two-stage amplifier X-axis direction readout (v3.0).

	Brand	Types of products	Mfr. part no.	Reference	Quantity per board
1	Panasonic	Switching diode	MA3X157A	D1A, D1B, D2A, D2B	2
2	KEMET	Ceramic multi-layer capacitor	C0603C109C 5GACTU	C1	1
3	MURATA	Ceramic multi-layer capacitor	GRM188B11E 104KA01D	C3, C21	2
4	KOA	Surface mount fixed resistor	RK73B2BTTD 220J	R30	1
5	NEC	NPN bipolar transistor	2SC3585-T1B-A	Q1	1
6	KOA	Surface mount fixed resistor	RK73B2ATTD 273J	R1	2
7	KOA	Surface mount fixed resistor	RK73B2ATTD 333J	R12	2
8	KOA	Surface mount fixed resistor	RK73B2ATTD 363J	R2	1

Table A.8: Electronic parts list of the daughter card for Radeka-type two-stage amplifier X-axis direction readout (v3.0).

	Brand	Types of products	Mfr. part no.	Reference	Quantity per board
9	KOA	Surface mount fixed resistor	RK73B2ATTD 912J	R3	1
10	KOA	Surface mount fixed resistor	RK73H2ATTD 51R0F	R4, R19, R20	3
11	KOA	Surface mount fixed resistor	RK73B2ATTD 473J	R5	1
12	NXP	NPN bipolar transistor	BSV52(,215)	Q2, Q3, Q4, Q5	4
13	KOA	Surface mount fixed resistor	RK73B2ATTD 330J	R6, R7, R13, R15, R16	5
14	ON Semiconductor	Zener diode	MMSZ5233BT 1G	Z1	1
15	KOA	Surface mount fixed resistor	RK73B2ATTD 682J	R8	1
16	MURATA	Ceramic multilayer capacitor	GRM31MB11E 105KA01L	C2, C4, C5, C6, C41	5
17	MURATA	Ceramic multilayer capacitor	GRM155B11H 271KA01D	C17	1
18	KOA	Surface mount fixed resistor	RK73H1JTTD 1000F	R29	1

Table A.9: Electronic parts list of the daughter card for Radeka-type two-stage amplifier X-axis direction readout (v3.0).

	Brand	Types of products	Mfr. part no.	Reference	Quantity per board
19	KOA	Surface mount fixed resistor	RK73H1JTTD 2001F	R10	1
20	KOA	Surface mount fixed resistor	RK73H1JTTD 8201F	R11	1
21	Bourns	Potentiometer	3382G-1-103G	R9	1
22	KOA	Surface mount fixed resistor	RK73B1JTTD 562J	R14	1
23	NEC	NPN bipolar transistor	2SC3356-T1 B-A-(R)	Q6	1
24	KOA	Surface mount fixed resistor	RK73B1JTTD 152J	R17	1
25	KOA	Surface mount fixed resistor	RK73H1JTTD 43R0F	R18	1
26	KOA	Surface mount fixed resistor	RK73H1JTTD 10R0F	R31, R32	2
27	MURATA	Ceramic multi-layer capacitor	GRM31MB11 H224KA01L	C15, C16	2
28	MAC8	For hybrid manufacturing	CB-1-5	No reference	11

A.4 Printed Circuit Board Maker

- Printed circuit board
  Printed Circuit Board PB by Towa-Tec Corporation [65]

- Front panel manufacturing
  Kyohritsu Electronic Industry Co., Ltd. / Takachi Electronics Enclosure Co., Ltd. [66]

- One of shield cases for amplifiers
  NPS inc. [67]

A.5 Parts Shop

- RS Online [68]

- Marutsu Online [69]

- Zaikostore [70]

- Monotaro [71]

- Akizukidenshi [72]

- Misumi [73]

A.6 Cost

Cost for v1.1 Mother Boards, v2.0 Daughter Cards and v3.0 Daughter Cards of Amplifier (JPY).

A.6.1 v1.1 Mother Board for $Y-$axis Readout

Table A.10: Cost for v1.1 Mother Boards

Revision designing	\10,000
5 Mother Boards printing	\23,300
Parts mounting	\29,500
Parts for 5 boards	\30,012
Sum (excluding tax)	\92,812
Sum (including 8% tax)	\100,237

A.6.2 v2.0 Daughter Card for $Y-$axis Readout

Table A.11: Cost for v2.0 Daughter Cards

80 Daughter Cards printing	\26,770
Parts mounting	\93,600
Parts for 80 boards	\60,773
Sum (excluding tax)	\181,143
Sum (including 8% tax)	\195,634

A.6.3 v3.0 Daughter Card for $X-$axis Readout

Table A.12: Cost for v3.0 Daughter Cards

Revision designing	\10,000
336 Daughter Cards printing	\38,810
Parts mounting	\104,160
Parts for 336 boards	\187,297
Sum (excluding tax)	\341,267
Sum (including 8% tax)	\368,568

Bibliography

[1] M. Kobayashi, T. Maskawa: "CP-Violation in the Renormalizable Theory of Weak Interaction", *Progressive of Theoretical Physics,* Vol. **49**, No. 2, pp. 652-657 (1973).

[2] Y. Ashie *et al.*: "Evidence for an oscillatory signature in atmospheric neutrino oscillations", *Phys. Rev. Lett.* **93** (10), 101801 (2004).

[3] K. Abe *et al.* (T2K Collaboration): "First Muon-Neutrino Disappearance Study with an Off-Axis Beam", *Phys. Rev.* D**85**, 031103 (2012).

[4] Y. Fukuda *et al.* (Super-Kamiokande Collaboration): "Evidence for Oscillation of Atmospheric Neutrinos", *Phys. Rev. Lett.* **81**, 1562 (1998).

[5] W. Marciano and A. Sanda: *Physics Letters* B 67 (3) 303 (1977).

[6] B. W. Lee and R. E. Shrock: *Phys. Rev.* D 16, 1444 (1977).

[7] B. Pontecorvo: *Phys. Rev.* Vol. 72, 246 (1947).

[8] E. P. Hincks and B. Pontecorvo: *Phys. Rev.* Vol. 73, 257 (1948).

[9] Y. Kuno and Y. Okada: "Muon Decay and Physics Beyond the Standard Model", *KEK Preprint*, 99-69, KEK-TH-639 (1999).

[10] A. de. Gouvea, N. Saoulidou: *Rev. Nucl. Part. Sci.* 60, 513 (2010).

[11] L. J. Hall, V. A. Kostelecky and S. Raby: *Nuclear Physics,* B**267** (1986).

[12] R. Barbieri, L. Hall and A. Strumia: *Nuclear Physics,* B**445** 219 (1995).

[13] Y. Kuno and Y. Okada: *Rev. of Mod. Phys.* **73** 151 (2001).

[14] J. Hisano and D. Nomura: *Phys. Rev.* D**59** 116005 (1999).

[15] The DeeMe Collaboration: "Proposal to the Experimental Search for μ-e Conversion in Nuclear Field at Sensitivity of 10^{-14} with Pulsed Proton Beam from RCS", (2011).

[16] A. Czarnecki, X. G. Tormo and W. J. Marciano: *Hyperfine Interact.* **210**, 19 (2012).

[17] W. Bertl *et al.* (SINDRUM Collaboration): "A Search for muon to electron conversion in muonic gold", *Euro. Phys,* Vol. 31, No. C 47, pp. 337-346 (2006).

[18] T. Mori *et al.* (MEG Collaboration): "Final Results of the MEG Experiment", *Nuovo. Cim.* C39, 325 (2017).

[19] Y. G. Cui *et al.* (COMET Collaboration): "COMET Conceptual Design Report", KEK-2009-10 (2009).

[20] R. J. Abrams *et al.* (Mu2e Collaboration): "Mu2e conceptual design report", *arXiv:* 1211. 7019 [phys.ins-det].

[21] J-PARC – Japan Proton Accelerator Research Conplex (n. d.), retrieved November, 2017, from `https://j-parc.jp/index-e.html`

[22] S. Makimura *et al., Meeting abstracts of the Physical Society of Japan* **68** (1), 152 (2013), Japanese.

[23] Y. Miyake *et al.*: "Current status of the J-PARC muon facility, MUSE", *Journal of Physics: Conference Series* **511** (2014) 012061.

[24] G4beamline (n. d.), retrieved January, 2019, from `http://www.muonsinternal.com/muons3/G4beamline/`

[25] Muon g-2/EDM at J-PARC (n. d.), retrieved June, 2018, from `http://g-2.kek.jp/portal/index.html`

[26] PiENu – TRIUMF (n. d.), retrieved December, 2017, from `https://pienu.triumf.ca/`

[27] M. Morii, T. Taniguchi and M.Ikeno: "Development of a readout electronics system for the VENUS vertex chamber", *KEK Internal*, 87-14 (1988).

[28] N. Teshima, *Master's Thesis, Osaka City University* (2016), unpublished.

[29] Ö. Şahin *et al.*: "Penning transfer in argon-based gas mixtures", *Journal of Instrumantation*, 5 (2010) P05002 1-30.

[30] M. E. Rose, S. A. Korff: *Phys. Rev.*, **59**, 850 (1941).

[31] M. A. Lieberman and A. J. Lichtenberg: *Principles of Plasma Discharges and Materials Proceeding*, John Wiley & Sons, Inc., 2nd edition (1994).

[32] Y. Takezaki, *Master's Thesis, Osaka City University* (2016), unpublished.

[33] Garfield++ - simulation of tracking detectors (n. d.), retrieved November, 2018,
from `https://garfieldpp.web.cern.ch/garfieldpp/`

[34] MIDAS Main Page (n. d.), retrieved December, 2018, from `https://midas.triumf.ca/MidasWiki/index.php/Main_Page`

[35] ROOT a Data analysis Framework (n. d.), retrieved December, 2018, from `https://root.cern.ch/`

[36] Osaka City University High Energy Physics at Work (n. d.), retrieved December, 2018, from `http://ocupc1.hep.osaka-cu.ac.jp/`

[37] LTspice (n. d.), retrieved December, 2018, from `https://www.analog.com/jp/design-center/design-tools-and-calculators/ltspice-simulator.html`

[38] Y. Kobayashi *et al.*: "PPS and MPS of experimental equipment at J-PARC MLF", Japanese.

[65] Printed board center PB – Printed circuit board manufacturing and design (n. d.), retrieved June, 2018,
from `http://pcb-center.com/`

[66] Takachi (n. d.), retrieved June, 2018,
from `http://www.takachi-el.co.jp/`

[67] NPS (n. d.), retrieved June, 2018,
from `http://nps1.jp/`

[68] RS Online (n. d.), retrieved June, 2018,
from `http://jp.rs-online.com/web/`

[69] Marutsu Online (n. d.), retrieved July, 2018, from `http://www.marutsu.co.jp/`

[70] Zaikostore.com (n. d.), retrieved July, 2018, from `https://www.zaikostore.com/zaikostore/`

[71] Monotaro.com (n. d.), retrieved July, 2018, from `http://www.monotaro.com/`

[72] Akizukidenshi (n. d.), retrieved July, 2018, from `http://akizukidenshi.com/catalog/default.aspx`

[73] Misumi (n. d.), retrieved July, 2018, from `http://jp.misumi-ec.com/`